Helmholtz-Zentrum Berlin für Materialien und Energie
und Institut für Physik und Astronomie, Universität Potsdam

Rashba effect on Dirac fermions in graphene

Dissertation

zur Erlangung des akademischen Grades "Doctor rerum naturalium"

(Dr. rer. nat.) in der Wissenschaftsdisziplin Experimentalphysik

von

Dmitry Marchenko

eingereicht an der
Mathematisch-Naturwissenschaftlichen Fakultät
der Universität Potsdam

Januar 2013

Marchenko, Dmitry
`marchenko.dmitry@gmail.com`
Rashba effect on Dirac fermions in graphene
Dissertation zur Erlangung des akademischen Grades "Doctor rerum naturalium" (Dr. rer. nat.) in der Wissenschaftsdisziplin Experimentalphysik
eingereicht an der Mathematisch-Naturwissenschaftlichen Fakultät
der Universität Potsdam
Supervisor: apl. Prof. Dr. Oliver Rader

SELBSTÄNDIGKEITSERKLÄRUNG

Hiermit erkläre ich, daß ich die vorliegende Arbeit selbständig angefertigt, nicht anderweitig zu Prüfungszwecken vorgelegt und keine anderen als die angegebenen Hilfsmittel verwendet habe. Sämtliche wissentlich verwendeten Textausschnitte, Zitate oder Inhalte anderer Verfasser wurden ausdrücklich als solche gekennzeichnet.

Potsdam, 28.11.2012

Dmitry Marchenko

CONTENTS

Introduction **7**

1 Experimental techniques **10**
- 1.1 Introduction . . . 10
- 1.2 X-Ray Photoelectron Spectroscopy . . . 10
- 1.3 Angle-Resolved Photoelectron Spectroscopy . . . 13
- 1.4 Spin- and Angle-Resolved Photoelectron Spectroscopy . . . 16
- 1.5 Low Energy Electron Diffraction . . . 19
- 1.6 Experimental stations . . . 21

2 Graphene and Rashba effect **23**
- 2.1 Graphene . . . 23
- 2.2 Rashba Effect . . . 27
  - 2.2.1 Rashba effect in case of 2D electron gas . . . 27
  - 2.2.2 Rashba effect in case of graphene . . . 30

3 Graphene on Ferromagnets **33**
- 3.1 Introduction . . . 33
- 3.2 Preparation . . . 33
- 3.3 Electronic structure and intact Dirac cones . . . 37
- 3.4 Absence of Rashba effect . . . 40
- 3.5 Dirac cone spin polarization . . . 42

4 Graphene on low-Z materials **50**
- 4.1 Introduction . . . 50
- 4.2 Graphene on SiC(0001) . . . 50
  - 4.2.1 Preparation . . . 50
  - 4.2.2 Electronic structure . . . 51
  - 4.2.3 Absence of Rashba effect . . . 53
- 4.3 Graphene on Silver . . . 58

5 Graphene on high-Z materials **60**
- 5.1 Graphene on gold . . . 60
  - 5.1.1 Preparation and electronic structure . . . 61
  - 5.1.2 Giant Rashba effect in graphene . . . 62
  - 5.1.3 Hybridization as the source of the giant splitting . . . 64
  - 5.1.4 Atmospheric stability . . . 81

5.2 Graphene on Iridium 86
    5.2.1 Iridium Surface State 88
    5.2.2 Giant Rashba effect in graphene 92
    5.2.3 Control of Rashba effect by rotational displacement 93

Summary and conclusions **102**

Bibliography **104**

Abbreviations **112**

Curriculum Vitae **113**

List of Publications **114**

Zusammenfassung **118**

Acknowledgements **120**

INTRODUCTION

In this thesis the externally induced Rashba effect and spin polarization in graphene is studied with the aim of controlling its size in a very wide range. This problem is of major scientific interest due to possible applications of graphene in spintronics. Graphene is a single layer of carbon atoms arranged in honeycomb lattice. Graphene is, in principle, known for a long time: the graphene electronic structure was, for example, calculated in 1947 [1], on a Ni(111) substrate it was prepared already in the 1970s [2], subsequently different methods of preparation were developed, and the graphene electronic structure was studied on different substrates [3–10]. For most of the time, it was called a *graphite monolayer* and the term *graphene* became popular only recently. Graphene became famous in 2004 after a micromechanical cleavage method for bulk graphite was proposed [11]. "*For groundbreaking experiments regarding the two-dimensional material graphene*" Andre Geim and Konstantin Novoselov were awarded the Nobel Prize in Physics in 2010 [12]. Due to a high quality and a lattice structure with two atoms per unit cell graphene has peculiar electronic, optical and mechanical properties. Graphene has a very high electron mobility [13] and is promising for ballistic transistors and transport [14], for field-effect transistors [11, 15], transparent conducting electrodes [16, 17], ultracapacitors [18] and many other applications.

The Rashba effect is related to spin-orbit coupling and is important for spintronics applications because it creates spin polarization of electronic states in nonmagnetic systems. The effect was discovered by Emmanuel I. Rashba and published in 1960 [19]. The Rashba splitting manifests itself first of all in the case of two-dimentional electron gas (2DEG) systems, like surface states of metals, quantum wells, semiconductor heterostructures, thin metallic films and graphene [20–26]. It appears in the presence of an external electric field normal to the two-dimentional electron gas plane or in the presence of a broken inversion symmetry because of interfaces or substrate [19,27]. Spin-orbit coupling can be utilized to achieve efficient spin filtering [28, 29] and due to spin precession it could be used in spin field-effect transistors [30, 31].

In this thesis we combine the graphene and spintronics topics and study how is it possible to control the spin polarization of the graphene electronic structure. The main idea is to find ways to produce a very small and a very large spin polarization or Rashba-type spin splitting in graphene by an external influence, to study which substrates are suitable for growing a high quality graphene layer with very small spin-orbit coupling and which substrates could give us observable in experiments and suitable to applications spin-polarization of Dirac fermions. Graphene for spintronics is very interesting, first of all, because it consists of carbon atoms and has a very weak intrinsic spin-orbit coupling. Electrons have in graphene a very long spin coherence length at room temperature [32–35], a successful control of the spin current in a gate-tunable graphene spin valve was shown [36]. Graphene could serve as a source of spin-polarized electrons [37] and as material for spin-filters [38] and spin field-effect transistors [30, 36]. Transport properties of graphene with an externally induced spin-orbit splitting have been intensively investigated in recent years and important predictions have been made: the spin Hall effect [39], the quantum spin Hall effect [40, 41] and, with an additional exchange interaction, the quantum anomalous Hall effect [42]. The Rashba effect in graphene even enhances the calculated Kondo temperature of adsorbed impurities [43].

The Rashba splitting of metalic surface states is known, on the other hand, for a long time. The best experimental example is the Au(111) surface state measured by angle-resolved photoelectron spectroscopy first in 1996 [21] and we will discuss this in detail in section 2.2.1. The observed large spin-orbit splitting of the Au(111) surface state is attributed to spread of the surface state wave function normal to the surface into the region of nuclear charge and experiencing an influence of atomic spin-orbit splitting; the model was developed in 1966 [44]. The substrate material nuclear charge role was later seen again when states with large spin-orbit splitting in a Au and Ag monolayers on W(110) were observed [26, 45]. It was shown that the size of the splitting does not depend on the atomic number of the Au or Ag overlayer but depends strongly on the substrate. Spin- and angle-resolved photoemission study revealed that the states in electronic structure of deposited thin metallic layers acquire spin polarization through spin-dependent overlayer-substrate hybridization. The effect of induced by substrate spin-orbit splitting was observed also for quantum-well states in gold, silver and aluminium films on W(110) substrate [46, 47]. In the current thesis we will try to use this possibility to induce spin-orbit coupling in overlayers through contact with high-Z substrates to produce a giant Rashba splitting of Dirac fermions in the graphene electronic structure.

The thesis has the following structure. In Chapter 1 we discuss the main experimental techniques used to study the systems in question, namely X-ray Photoelectron Spectroscopy (XPS), Angle-Resolved Photoelectron Spectroscopy (ARPES), Spin-resolved ARPES (SARPES), Low-Energy Electron Diffraction (LEED) as well as an overview of the experimental stations at which experiments have been conducted.

Chapter 2 contains overviews of the two main topics of this thesis, namely the graphene and the Rashba effect. First each of these topics is introduced and then it is shown how to combine them, i.e. how the Rashba effect in graphene should look like. Then Chapter 3 is related to the electronic and spin structure of graphene grown on transition metal ferromagnets. The discovery of intact Dirac cones is discussed as well as the Rashba effect and Dirac cone spin polarization. In Chapter 4 graphene on other low-Z substrates such as silicon carbide and silver is treated, in some sense in continuation of the previous chapter. The main topic aim is to elucidate possibility to induce spin-orbit coupling by interaction with a low-Z substrate.

Chapter 5 is the main chapter of this thesis. It is devoted to the giant Rashba effect in graphene induced by high-Z substrates. The chapter is split into two parts: graphene on gold and graphene on iridium. The first part concerns the electronic and spin structure and the observation of the giant Rashba effect in the graphene/Au system. There are discussions from both experimental and theoretical sides. Also the atmospheric stability of the graphene/Au system is shown. The second part is devoted to the graphene/Ir system: protection of iridium surface states by the graphene layer, a giant Rashba effect and its control by rotational displacement of graphene domains relative to the iridium substrate.

CHAPTER 1

EXPERIMENTAL TECHNIQUES

1.1 Introduction

Photoelectron spectroscopy is one of the most direct and extensively used experimental techniques in solid state physics for the investigation of the electronic structure of materials [48]. It is based on the *photoelectric effect*, i.e.,emission of electrons as a consequence of absorption of photons, first observed by Heinrich Hertz in 1887 [49] and explained by Einstein in 1905 [50]. Later such photoelectric effect developed into a variety of techniques which differ in the energy of photons used and the information about the electronic structure they provide. We will consider in more detail X-Ray Photoelectron Spectroscopy (XPS), Angle-Resolved PhotoElectron Spectroscopy (ARPES) and Spin- and Angle-Resolved PhotoElectron Spectroscopy (SARPES). ARPES is a part of Ultraviolet Photoelectron Spectroscopy (UPS) and is focused on the dispersion of electronic valence bands. SARPES additionally probes the spin polarization in one or several directions. Photon energies in UPS are relatively small, in the ultra-violet range, 10-100 eV. For XPS higher photon energies are used and main focus goes to localized core-levels of the system in study.

1.2 X-Ray Photoelectron Spectroscopy

When light is incident on a sample, it can be absorbed allowing electrons to escape from the material. They carry a certain kinetic energy, which is determined by the electronic structure of the sample and the incident beam energy $\hbar\omega$. There are two main models of such process: The one-step model of photoemission as a transition between initial and final states consisting of wave functions that obey appropriate boundary conditions at the surface as well as a rather simplified three-step model. We will consider in this work only the second one because it has proven to be rather successful [51, 52] and gives enough information on the processes in the systems which we study.

The three-step model of photoemission considers these three independent steps:

1. Photoexcitation of electron by incident light;
2. Travel of the excited electron to the surface;
3. Escape of the electron through the surface potential barrier into vacuum.

Monochromatized light of energy $\hbar\omega$ hits the sample and excites electrons from an occupied initial state Ψ_i with energy E_i to an unoccupied final state Ψ_f with energy E_f. In the one-electron approach the Schrödinger equation $\hat{H}\Psi = i\hbar\frac{\partial\Psi}{\partial t}$ for the electron in electromagnetic field with vector potential $\mathbf{A}$ is:

$$\left[\frac{1}{2m}\left(\hat{p}+\frac{e}{c}\mathbf{A}\right)^2 + V(r)\right]\Psi = i\hbar\frac{\partial\Psi}{\partial t} \tag{1.1}$$

where $\hat{p} = -i\hbar\nabla$ is the momentum operator and V(r) the potential in which electron is moving.

In the dipole approximation we consider the vector potential as small and constant over atomic dimensions, therefore $\nabla\mathbf{A} = 0$ and it is possible to express the hamiltonian by a sum of the stationary state of the unperturbed system and a perturbation: $\hat{H} = \hat{H}_0 + \hat{H}'$, where

$$\hat{H}_0 = \frac{\hat{p}^2}{2m} + V(r) \qquad \hat{H}' = \frac{e}{2mc}(\mathbf{A}\hat{p} + \hat{p}\mathbf{A}) \approx \frac{e}{mc}\mathbf{A}\hat{p} \tag{1.2}$$

The transition rate is given by Fermi's golden rule:

$$P_{if} = \frac{2\pi}{\hbar}| < \Psi_f|\hat{H}'|\Psi_i > |^2\ \delta(E_f - E_i - \hbar\omega) \tag{1.3}$$

Using commutators $[\hat{p},\hat{H}_0] = -i\hbar\nabla V$ and $[\mathbf{r},\hat{H}] = i\hbar\hat{p}/m$ one can write the matrix element in the following form:

$$< \Psi_f|\mathbf{p}|\Psi_i >= im\omega < \Psi_f|\mathbf{r}|\Psi_i >= \frac{i}{\omega} < \Psi_f|\nabla V|\Psi_i > \tag{1.4}$$

So, for a true free electron system with $\nabla V = 0$ the photoemission process does not take place. But at the surface of the sample or close to nuclei $\partial V/\partial z \neq 0$ and a photoeffect occurs [52]. The final state is defined by the band structure of unocupied bands, but for rather high energies a free parabolic final band approximation is most commonly used [48].

The second step of the photoemission process is the travelling of the excited electron to the surface. Electrons may as well travel away from the surface and scatter several times before reaching the surface. The inelastic scattering process gives rise to a large background of secondary electrons in the spectra which is usually subtracted or even ignored. Probability of reaching surface without scattering is determined by the inelastic mean free path λ:

$$\frac{N}{N_0} = \exp\left(-\frac{d}{\lambda}\right) \tag{1.5}$$

where N_0 - initial number of excited photoelectrons, N - number of photoelectrons which reach the surface, d - distance to the surface. The λ value depends in turn on the electron energy and on the interaction strength for that energy with other electrons, phonons etc.

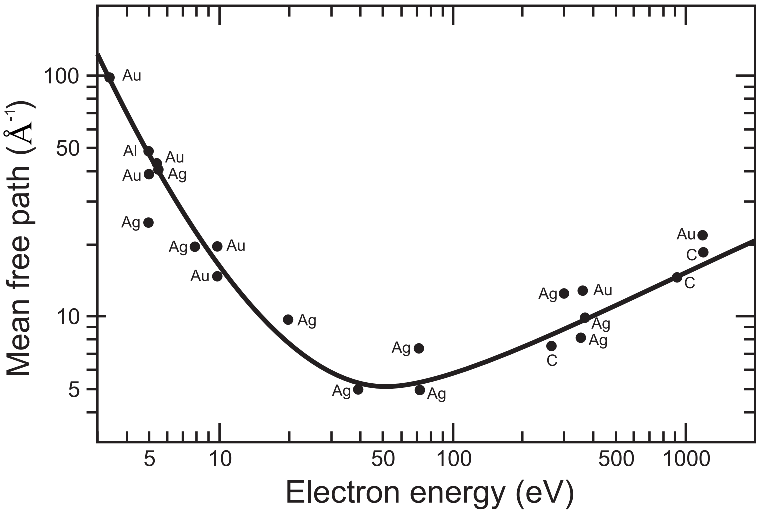

Figure 1.1: *'Universal curve': inelastic mean free path versus electron kinetic energy for various elements [48, 53].*

This dependence is about universal for all materials and is shown in Figure 1.1 [48, 53]. There is a minumum of λ around 50-60 eV kinetic energy, corresponding to an escape depth of about 5 Å. Therefore, ARPES and SARPES are surface sensitive techniques which probe the band structure of the top one or two atomic layers of material. Nevertheless, the initial state wave function Ψ_i may extend into the bulk, allowing to probe the bulk electronic structure as well. At higher energies the escape depth is larger, so that XPS gives more information about the bulk of the material. However, surface components are sometimes also present as shoulders near the main core-level peaks.

The third step of the photoemission process is the escape of the electron through the surface potential barrier into vacuum. This is possible if the photoelectron energy is higher than the work function Φ. The electron kinetic energy E'_{kin} in the vacuum is then:

$$E'_{kin} = \hbar\omega - |E_B| - \Phi \tag{1.6}$$

where E_B is the binding energy of the initial state, i.e. initial energy of the photoelectron before photoexcitation relative to the Fermi energy $E_B = E_F - E_i$. Electron then travels through the vacuum to the analyzer. Sample and analyzer are grounded (Fig. 1.2(a)), so that, they have the same Fermi level. The analyzer's work function Φ_a is different from the sample's work function Φ and, consequently, detected kinetic energy E_{kin} is also different:

$$E_{kin} = \hbar\omega - |E_B| - \Phi_a \tag{1.7}$$

For a detailed picture for energetics of the photoemission and detection processes see Figure 1.2(b), and for the structure of a typical XPS overview spectrum Figure 1.3. In

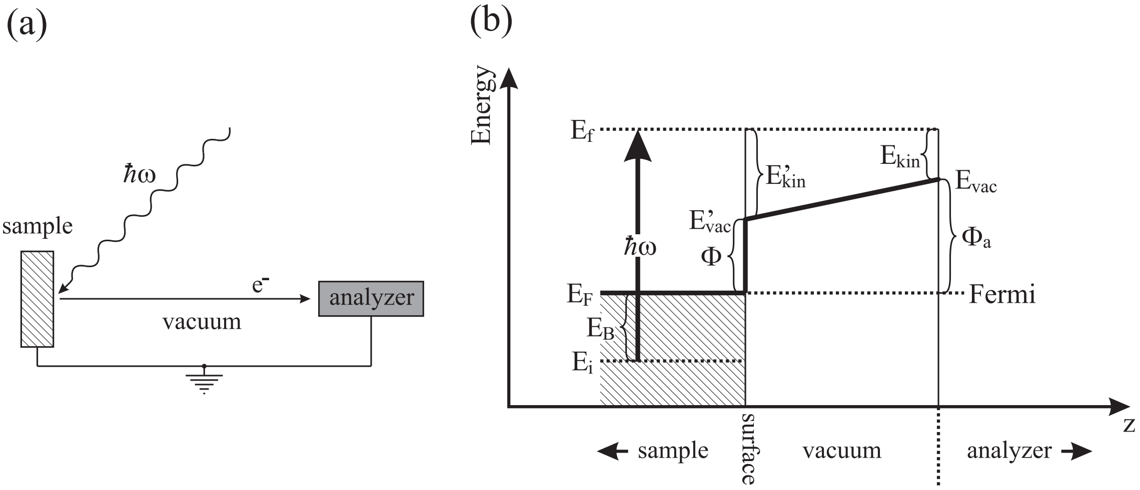

Figure 1.2: *(a) A general schematic of experiment. Photons incident on the sample produce photoelectrons which travel through vacuum to the analyzer. Sample and analyzer are grounded. (b) Energetics of the photoemission and detection processes.* E_i *and* E_f *are initial and final states,* Φ *and* Φ_a *are work functions of sample and analyzer respectivly.*

experiments with metallic samples, the binding energy E_B is usually determined from the spectrum by a direct measurement of the energy separation from the Fermi edge to the peak of interest.

1.3 Angle-Resolved Photoelectron Spectroscopy

Angle-Resolved Photoelectron Spectroscopy (ARPES) is the most commonly used method to study dispersions and other properties of the occupied electronic states in the valence band. Dispersions are energy versus wave vector dependences of the electron in initial state $E_i(\mathbf{k}_i)$. The photon energy $\hbar\omega$ of the incident light in ARPES in the general case is in the vacuum ultra-violet range and its momentum $\mathbf{p}_{ph} = \hbar\omega/c$ is very small compared to the size of the Brillouin zone of the material under study. Therefore, transfer of electrons to the final state during photoexcitation practically happens without change of the wave vector, $\mathbf{k}_f = \mathbf{k}_i$. It is useful to independently consider the components parallel to the surface and perpendicular to the surface, $\mathbf{k}_f = \mathbf{k}_{\parallel}^{in} + \mathbf{k}_{\perp}^{in}$, because they behave differently when the electron crosses the surface of the sample.

Due to the translational symmetry at the crystalline surface $\mathbf{k}_{\parallel}^{out} = \mathbf{k}_{\parallel}^{in} + \mathbf{G}$, where ^{in} and ^{out} denote inside and outside the sample; $\mathbf{G}$ is a reciprocal surface lattice vector. In the following, we will consider only the first Brillouin zone and $\mathbf{k}_{\parallel}^{out} = \mathbf{k}_{\parallel}^{in}$.

Because of the sample's work function Φ and energy conservation, component of the

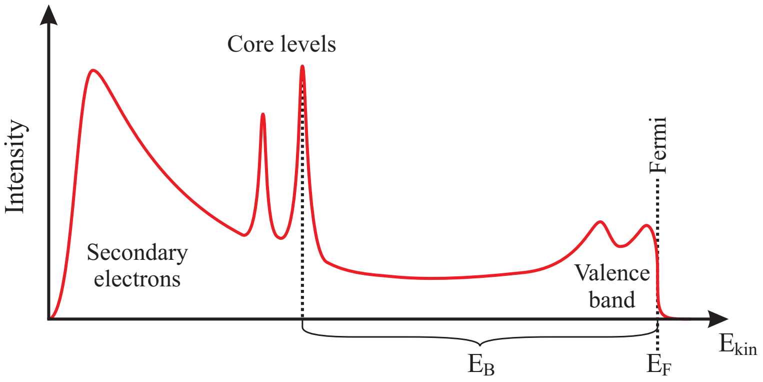

Figure 1.3: *Structure of a typical XPS overview spectrum. Down to about 10 eV below the Fermi level there is the valence band. At smaller kinetic energies E_{kin} (larger binding energies E_B) there are discrete core levels. Closer to zero kinetic energies there is a large secondary electron background.*

wave vector normal to the surface changes during transition of the photoelectron from the sample into vacuum:

$$k_{\perp}^{out} = \sqrt{(k_{\perp}^{in})^2 - \frac{2m\Phi}{\hbar^2}} \tag{1.8}$$

Knowing the kinetic energy and the direction in which the photoelectron moves in vacuum (defined by an angle θ relative to the sample surface normal, see Figure 1.4(a,b)), we have:

$$k_{\perp}^{out} = |\mathbf{k}^{out}|\cos(\theta) = \sqrt{\frac{2mE_{kin}}{\hbar^2}}\cos(\theta) \tag{1.9}$$

$$k_{\perp}^{in} = \sqrt{\frac{2m}{\hbar^2}(E_{kin}\cdot\cos^2(\theta)+\Phi)} \tag{1.10}$$

For the component parallel to the surface:

$$k_{\parallel}^{in} = k_{\parallel}^{out} = |\mathbf{k}^{out}|\sin(\theta) = \sqrt{\frac{2mE_{kin}}{\hbar^2}}\sin(\theta) = \sqrt{\frac{2m(\hbar\omega-|E_B|-\Phi_a)}{\hbar^2}}\sin(\theta) \tag{1.11}$$

If energies are given in units of eV and the wave vector in units of Å, it is possible to write the simplified equation $k_{\parallel}^{in} \approx 0.512\sqrt{\hbar\omega-|E_B|-\Phi_a}\sin(\theta)$. Thus, as a result of measuring the binding energies of bands for different angles one can get full three-dimensional $E_B(\mathbf{k}^{in})$ dispersion relations for the electronic bands in the valence band of the sample. In the case of two-dimentional systems like surface states or one atom thick films there is no dispersion in the direction normal to the surface and $\mathbf{k}_{\parallel}^{in}$ is enough.

In the experiments for the present Thesis hemispherical energy analyzers were used

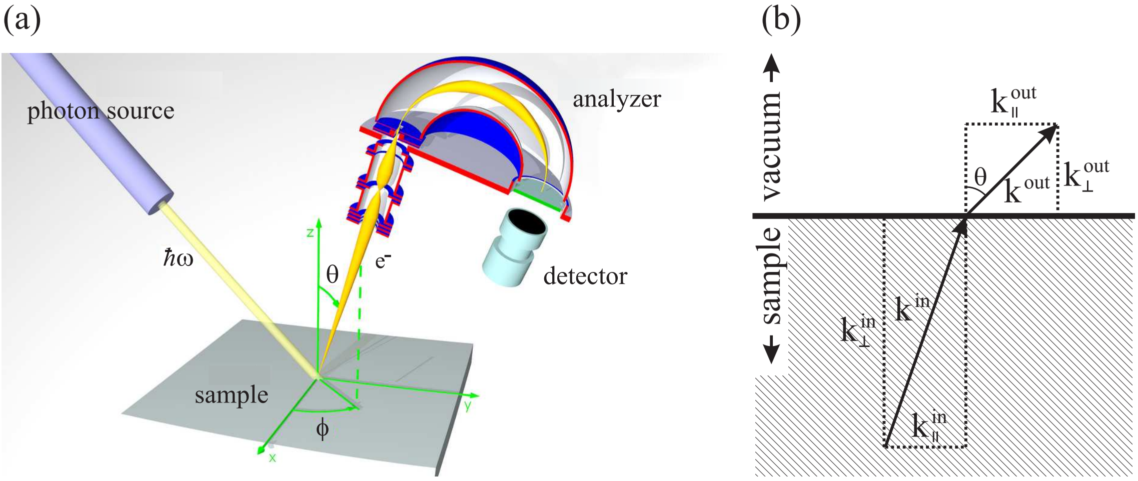

Figure 1.4: *(a) Geometry of the ARPES experiment. Analyzer detects photoelectrons emitted at an angle θ to the surface normal. Figure at the panel (a) is adapted from Ref. [54]. (b) Scheme of refraction of the photoelectron at the sample surface.*

[48], see Figure 1.4(a). A hemispherical analyzer consists of electrostatic lens module, entrance slit, hemispheres, exit slit and detector. Electrostatic lenses focus incoming photoelectrons to the entrance slit, through which electrons enter the space between the hemispheres with a certain kinetic energy. Then, due to the potential difference between the inner and outer hemispheres, electrons propagate on a circular trajectory to the exit slit on the other side of the analyzer. Only electrons which enter the analyzer with a specific kinetic energy can get to the exit slit, and that energy depends on voltages on hemispheres. Due to the small size of the entrance slit, the analyzer selects only the electrons in a specific direction. A finite angle divergence $\Delta\alpha$ determines the angle resolution, usually about 0.1° for the ARPES, 1° for the SARPES (to get higher intensity) and up to 15° for XPS (usually there is no need in angle resolution for XPS).

Behind the exit slit of the analyzer there is a detector which multiplies number of incoming electrons to measurable current. There are two main types of detectors in ARPES: based on channeltron electron multipliers and based on channelplates. With a channeltron type detector the measurement of only one angle and a few energies, depending on the number of channeltrons, at a time is possible and an angle dependence is measured by changing angle between the sample normal and the analyzer; energy spectrum is achieved by scanning different energies in the needed energy region. Channelplate-based detectors, in turn, show angle and energy dependence directly in one image. Scanning of voltages is nevertheless needed to obtain data in a wider energy region.

Summarizing the above, it is possible to measure $I(E_{kin}, \theta, \phi)$ specta of photoelectrons from the sample, where I measured intensity proportional the number of photoelectrons and θ and ϕ are angles between the sample normal and analyzer (see Fig. 1.4(a)). By

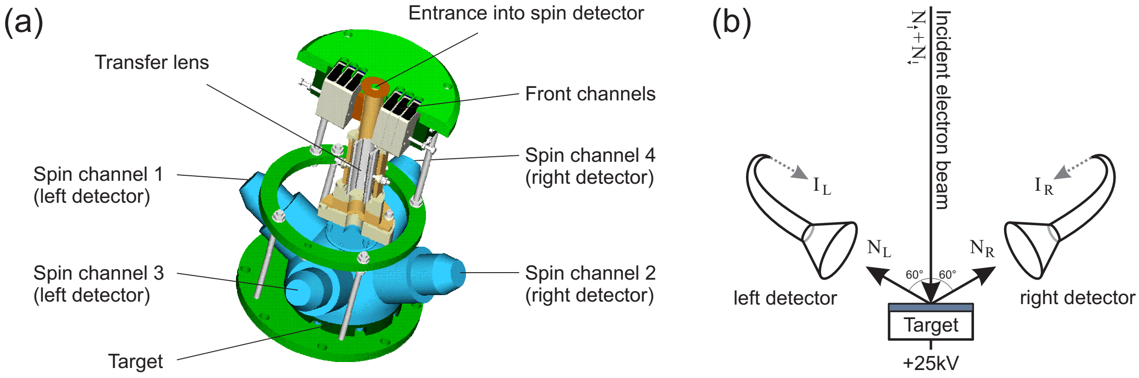

Figure 1.5: *(a) General scheme of the Mott detector [55] and (b) its work principle. Incoming electrons are accelerated by 25 kV and hit a target, part of them scatter backwards (Rutherford scattering) and enter channeltron detectors located at opposite sides. From the difference in measured currents from these detectors the spin polarization is determined.*

converting E_{kin} into E_B and $\mathbf{k}^{in}$ as was shown above, information about the dispersions in the valence band of the sample is obtained.

1.4 Spin- and Angle-Resolved Photoelectron Spectroscopy

Spin- and Angle-Rosolved Photoelectron Spectroscopy (SARPES) is used when information about the spin polarization of the electronic bands under study is required. In the general case the electron spin is preserved during the photoemission process, provided that magnetic fields are absent, i.e., the detected spin direction is the same as of electrons inside the sample before photoexcitation. For detection of the spin polarization and spin direction a conventional hemispherical electron energy analyzer was used equipped with a Rice University-type Mott detector [55, 56], Fig. 1.5. This detector works as follows: After passing the exit slit of the hemispherical analyzer photoelectrons are accelerated by a 25 kV potential and then experience spin-dependent Mott scattering from a target witha a high atomic number. Usually gold or thorium foils are used. After backscattering, electrons enter into one of four channeltron-type detectors located around the target at 90° to each other and 60° to the target surface normal, see Fig. 1.5.

The Mott scattering is spin-dependent. Let $N_\uparrow$ and $N_\downarrow$ be the number of electrons with spin up and down, respectively, hitting the target. A large fraction of these electrons will be lost in the bulk of the target but a small amount will backscatter and enter the detectors. Two opposite detectors will be sensitive to the spin quantization axis normal to the scattering plane: with the counts in the left detector $N_L \propto \frac{1}{2}\left[N_\uparrow(1+S)+N_\downarrow(1-S)\right]$

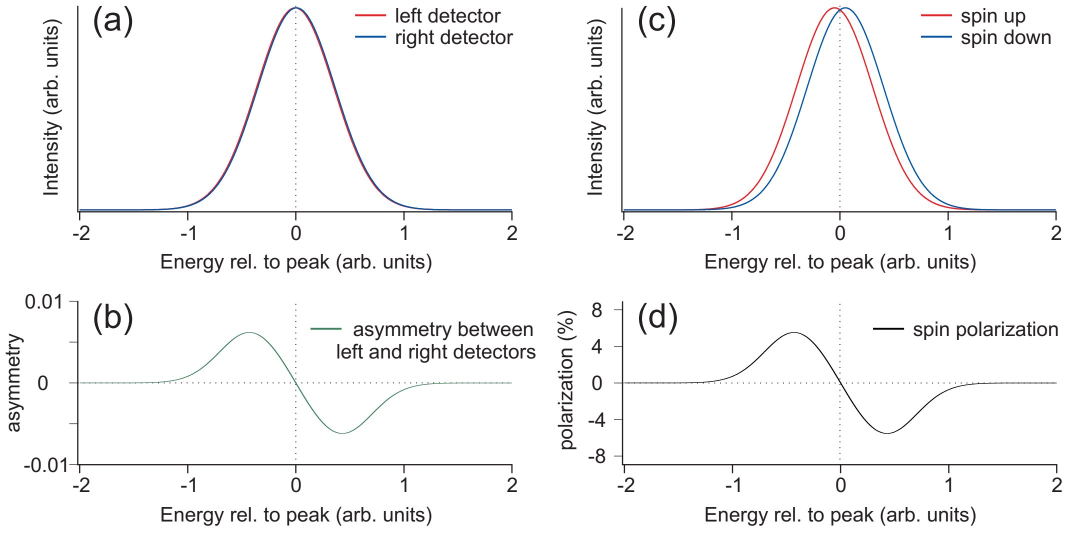

Figure 1.6: *Principle of spin-resolved measurement for an ideal spin-split Gauss peak: (a) result of measurement by left and right detectors; (b) corresponding asymmetry between left and right channels; (c) calculated shapes of spin up and spin down spectra; (d) corresponding spin polarization.*

electrons and those on the right one $N_R \propto \frac{1}{2}\left[N_\uparrow(1-S)+N_\downarrow(1+S)\right]$, where the constant S is called *Sherman function* and characterizes the efficiency of the spin detector, the measured asymmetry between channels is:

$$A_{LR} = \frac{N_L - N_R}{N_L + N_R} = S\frac{N_\uparrow - N_\downarrow}{N_\uparrow + N_\downarrow} = S \cdot P \tag{1.12}$$

where P is the spin polarization of the photoelectrons entering the spin detector. It is possible to obtain the number of spin up and spin down electrons from measured counts N_L and N_R:

$$N_\uparrow \propto \frac{1}{2}(N_L + N_R)(1 + A_{LR}/S) \tag{1.13}$$

$$N_\downarrow \propto \frac{1}{2}(N_L + N_R)(1 - A_{LR}/S) \tag{1.14}$$

In Figure 1.6 this data conversion is demonstrated based for the example of an ideal spin-split Gauss peak. The splitting is 0.1 in energy units, the FWHM is about 0.83 and the dimentionless Sherman function is 0.112. In Fig. 1.6(a) it is shown how the measured spectra look like. The difference between the left and right detectors measurements is too small to see by eyes, but the asymmetry calculated by equation 1.12 and presented in Fig. 1.6(b) clearly shows the presence of a spin splitting. In Fig. 1.6(c,d) spin up and spin

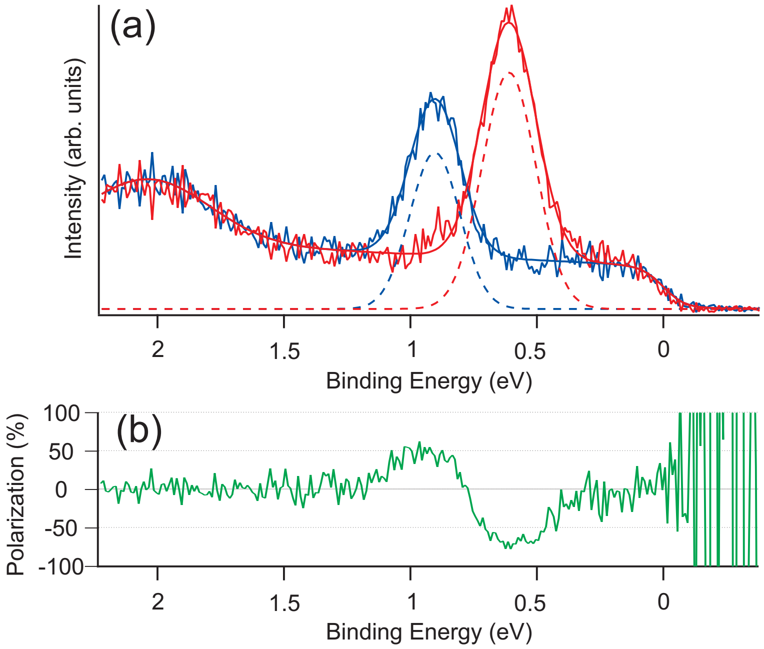

Figure 1.7: *(a) Example of spin-split band in the electronic structure of one monolayer of gold on W(110). Red and blue lines are spin up and spin down spectra from measurements together with their fits; dashed lines are fits of peaks after background substraction. (b) Corresponding spin polarization.*

down peaks and the spin polarization are shown, calculated by equations 1.13, 1.14 and 1.12 corespondingly.

It is interesting to note that such spin-resolved measurements are not limited by the energy resolution of the experiment. Even infinitely small spin splittings can theoretically be resolved if the measurements could be performed with perfect statistics without any noise. In reality, spin-resolved measurements take a large amount of time and at the end after the conversion still have rather large noise. This limits the possibility to determine exact values for splitting and polarization. In Figure 1.7(a) an example of an experimentally obtained spin-resolved spectrum of a spin-split interface state from a monolayer of gold on tungsten (110) is shown (details about this state see in Ref. [26]). Noisy red and blue lines represent spin up and spin down, respectively. Red and blue lines without noise are fitting results; dashed lines represent fits of peaks after background substraction. In Figure 1.7(b) the spin polarization is shown calculated directly as the difference divided by the sum of spin up and spin down spectra. This is typical presentation of spin-resolved measurements results and here the spin polarization at the peak positions is about 50-70%. It is, however, important to note, that in Figure 1.7(b) the polarization of all electrons (peak and background) at a given energy is shown. To determine the polarization of a certain band in the electronic structure, one has to fit the spectra and use

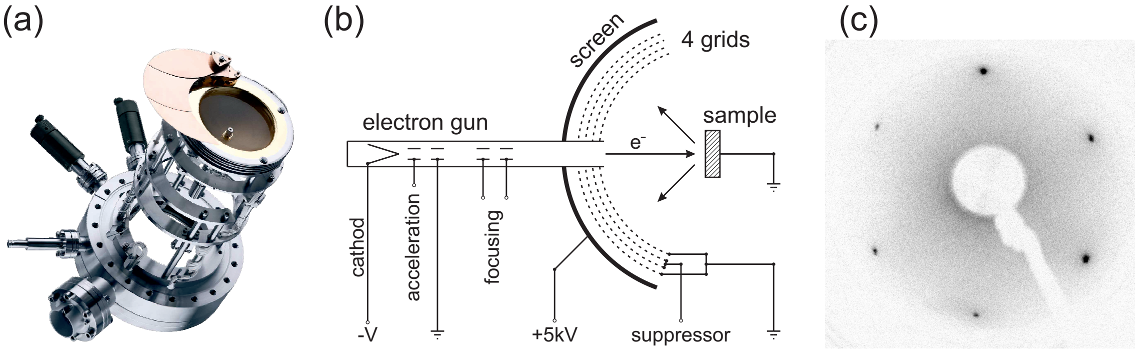

Figure 1.8: *Low Energy Electron Diffraction device [55] (a) and wire diagram explaining its working principle (b). (c) Example of diffraction image obtained by LEED from a clean Ir(111) surface (inverted colours); hexagon of dark spots is produced by diffraction of electron beam from the triangle grid of iridium atoms at the surface.*

for the polarization calculation instead of the electron counts the area under the peak of interest without background and unrelated peaks. In such approach, the spin polarization of each of two components of the split peak of Figure 1.7(a) is about 100%, i.e. each of these components in the band structure consists of only one spin direction. In the case when there is no splitting, but a spin polarization is present, one would see spin up and spin down peaks at the same energy position, but having different intensity.

1.5 Low Energy Electron Diffraction

Low Energy Electron Diffraction (LEED) was used to study the quality of sample surface, its crystallographic structure, the ordering of adsorbate atoms at the surface and for the alignment of the sample in the photoemission experiments along certain hight-symmetry directions. An electron gun produces a beam of electrons with low energy (about 20-200 eV) which hits the sample surface, backscatters, passes several grids and reaches a fluorescent screen at a +5 kV potential. If the surface has an ordered structure, diffraction of elastically reflected beams occurs and is visible as an arranged structure of spots on the fluorescent screen. Because of the small mean free path of electrons at these energies , LEED is a surface sensitive technique with probing depth of only 5-10Å.

In Figure 1.8(a) a conventional LEED device [55] is shown. Figure 1.8(b) is a simplified wire diagram explaining its working principle. The LEED device consists of an electron gun, grids and screen. Electrons are emitted from a cathod under negative potential and are accelerated and focused in the direction of the sample. After reflection from sample surface involving diffraction, the electrons pass four grids and hit the fluorescent screen. Because of a special grounded contact inside of the electron gun after electron acceleration, sample grounding and a grounded first grid, the electrons travel in zero po-

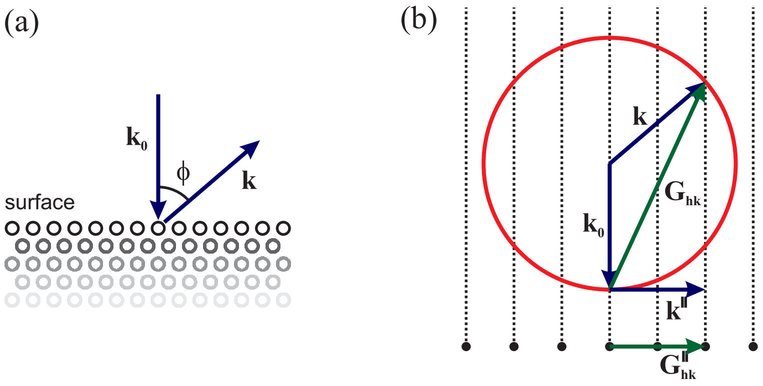

Figure 1.9: *(a) Real space picture. Incident electron beam hits the sample surface normally and scatters in all directions. In certain directions constructive interference happens and diffraction spots appear on the LEED screen. (b) Reciprocal space picture and Ewald construction - graphical presentation of equations 1.17. Each point of the 2-dimensional reciprocal lattice is an infinite rod in the third dimension.*

tential on straight lines inside the experimental chamber. The second and third grid are for suppression of inelastically scattered low energy electrons. The fourth grid is also grounded and protects thre other grids from the +5 kV potential of the screen. Other ways of use are possible, but we don't consider them in this work. Figure 1.8(c) shows the example of a LEED image obtained from a clean Ir(111) surface. The hexagonal structure of the LEED spots means that iridium atoms on the Ir(111) surface are arranged in two-dimensional hexagonal lattice.

The electron beam incident on the sample with momentum p can be considered as *de Broglie* waves with wavelength $\lambda = h/p = h/\sqrt{2m_eE}$ (where h is Planck's constant, m_e - mass of electron, E - electron beam energy). One can write a simplified equation also as well: $\lambda[nm] \approx \sqrt{1.5/E[eV]}$. These waves scatter from the ordered structure of atoms of the surface and interfere with each other. If in some direction distance between atoms (or adatoms) on the surface is d then there are diffraction spots at angles ϕ (relative to the surface normal) given by the *Bragg equation* which describes the conditions for constructive interference:

$$d\sin(\phi) = n\lambda \tag{1.15}$$

From this equation it is clear that angle-distances ϕ on the LEED screen are inverse proportional to the real distances d; thus, reciprocal space description in LEED pictures analysis is commonly used.

Let us consider a lattice of atoms at the surface defined by primitive vectors $(\mathbf{a},\mathbf{b})$.

Primitive vectors of the reciprocal lattice are then:

$$\mathbf{a}^* = \frac{2\pi\,\mathbf{b}\times\mathbf{n}}{|\mathbf{a}\times\mathbf{b}|} \qquad \mathbf{b}^* = \frac{2\pi\,\mathbf{n}\times\mathbf{a}}{|\mathbf{a}\times\mathbf{b}|} \tag{1.16}$$

where $\mathbf{n}$ is the unit vector normal to the surface [57]. By the *Laue condition*, incident electrons of wave vector $\mathbf{k_0}$ and scattered electrons of wave vector $\mathbf{k}$ obey the equations:

$$|\mathbf{k}| = |\mathbf{k_0}| = \frac{2\pi}{\lambda} \qquad \mathbf{k}^{\|} = \mathbf{G}_{hk}^{\|} = h\mathbf{a}^* + k\mathbf{b}^* \tag{1.17}$$

where h and k are integers.

Graphically these equations can be presented as a so-called *Ewald construction* for the case of a 2-dimensional lattice [58], see Figure 1.9. A real space picture is shown in Figure 1.9(a) and the corresponding reciprocal lattice picture is shown in Figure 1.9(b). Both are side view representations. Because scattering occurs mostly at the surface layer (which is 2-dimensional), the reciprocal space lattice is also 2-dimensional, but along the third axis each point spreads infinitely like rods. Projections $\mathbf{G}_{hk}^{\|}$ are diskrete values depending on integer h and k. The length of the scattered wave vector is the same as that of the incident wave vector; its possible directions are such that the vector's start and end are both on rods.

Note that there is inverse proportionality of distances on the LEED picture relative to real distances at the surface. This leads to the effect, that long range superstructures due to adatoms or a moiré pattern are visible in the LEED pictures as small superstructures around main LEED spots.

1.6 Experimental stations

All measurements were done at the BESSY-II synchrotron, Berlin. Electrons are emitted by an electron gun and accelerated in a microtron and a synchrotron to the energy of 1.7 GeV. Then electrons are injected into the storage ring where they live for 8 hours before the next injection. During these 8 hours there is a current of ∼150-300 mA due to moving electrons by approximately circular closed orbit in the storage ring. This orbit is not a perfect circle, it consist of many straight parts and *insertion devices* such as *bending magnets* and *undulators*. In bending magnets (also called as *dipoles*) electrons with horizontal speed come into a vertical magnetic field. The Lorentz force acts perpendicular to both the magnetic field and the electron speed and deflect electrons from the straight line movement, this leads to emission of *synchrotron radiation* by a tangent line as a result of acceleration due to the normal to electron movement direction Lorentz force. In undulators there are many bending magnets with opposite magnetic field direction and the synchrotron radiation from each of them participate in interference. As a result an emission angle is smaller and energy spectrum is narrower but intensity is much larger compared to the case when radiaton from each bending magnet is directly added without interference. Except the high radiation intensity modern undulators allow to control polarization of the emitted synchrotron light.

After the bending magnets and undulators electrons continue to move in the storage ring but radiation goes by straight lines into many beamlines around the storage ring. In beamlines radiation passes monochromator which selects the needed photon energy and a number of focusing mirrors. As a result, photons are focused in small focus points inside preparation chambers which are located at the end of beamlines. During the work on this thesis several BESSY beamlines were used, two branches of UE-112 beamline, BUS beamline, RGBL beamline.

Several experimental stations were used for experiments. The main are: '*1-square*' station for high resolution angle-resolved photoelectron spectroscopy and '*PHOENEXS*' for spin-resolved measurements. The first one, '*1-square*' station, is equipped with Scienta R8000 [59] hemispherical electron energy analyzer and a 6-axes automated cryomanipulator. Energy and angle resolution were 6 meV and 0.3°, respectively. The '*PHOENEXS*' station has a SPECS PHOIBOS 150 hemispherical electron energy analyzer [55] coupled to a Rice University Mott-type spin polarimeter [55,56] operated at 26 kV. Overall energy and angular resolutions of the experiments were 80 meV and 1°. Details about the work principle of the hemispherical analyzers and the Mott-detector were presented above in sections 1.3 and 1.4. Scanning tunneling microscopy (STM) measurements were made in a separate station equipped with Omicron VT SPM [60]. STM measurements were done at room temperature with tungsten tips.

All mentioned experimental stations consist of ultra-high vacuum (UHV) chambers with $\sim 10^{-10}$ mbar base pressure. In each of these systems there are analytical chamber (where measurements were conducted), preparation chamber (where the main sample preparation procedures were conducted) and a *load-lock* system (through which samples were transfered between air and UHV). Each experimental station contains low-energy electron diffraction (LEED) module (was discussed in section 1.5), exchangeable evaporators of different materials, quatz microbalance, leak-valve for controlled gas injection, sputter gun, high temperature heater (up to 2000°C) and wobble-sticks for sample transfer.

CHAPTER 2

GRAPHENE AND RASHBA EFFECT

2.1 Graphene

Graphene is a single layer of carbon atoms arranged in a honeycomb crystal structure. It is a carbon allotrope similar to graphite but consists of only one layer, i.e., graphene is two-dimensional. The carbon-carbon distance in-plane is $d = 1.42$ Å, but graphene has two atoms in unit cell and, thus, the lattice constant of graphene is $a = \sqrt{3}d = 2.46$ Å.

It is possible to grow graphene on many different substrates by various methods, such as:

1. segregation of dissolved carbon contamination from the substrate bulk to the surface [2];

2. *cracking* of hydrocarbons on hot surface [3–5];

3. intercalation of materials under the graphene layer [6, 7, 10];

4. thermal decomposition of SiC [8, 9];

5. micromechanical cleavage of bulk graphite [11, 13].

In this chapter we will not consider the growth methods in details, they will be discussed in the corresponding chapters specifically to the systems in question. The history of graphene, its peculiar properties and possible applications have shortly been discussed in the introduction. We will focus here on the theoretical description of the electronic structure of a free ideal graphene layer, because the large number of its properties is due to its peculiar electronic structure.

We will consider the graphene electronic structure from point of view of the tight binding approximation, where the electronic band structure is calculated using a set of wave functions made of superpositions of wave functions for isolated atoms. In graphene the carbon $2s$ and $2p$ orbitals undergo a sp^2-hybridization and for each carbon atom form three in-plane sp^2 bonds and one out-of-plane p_z bond. In the graphene electronic structure they form three σ and one π band. For the peculiar graphene electronic properties, mostly the π band plays a role and we will consider at this stage only the π band dispersion.

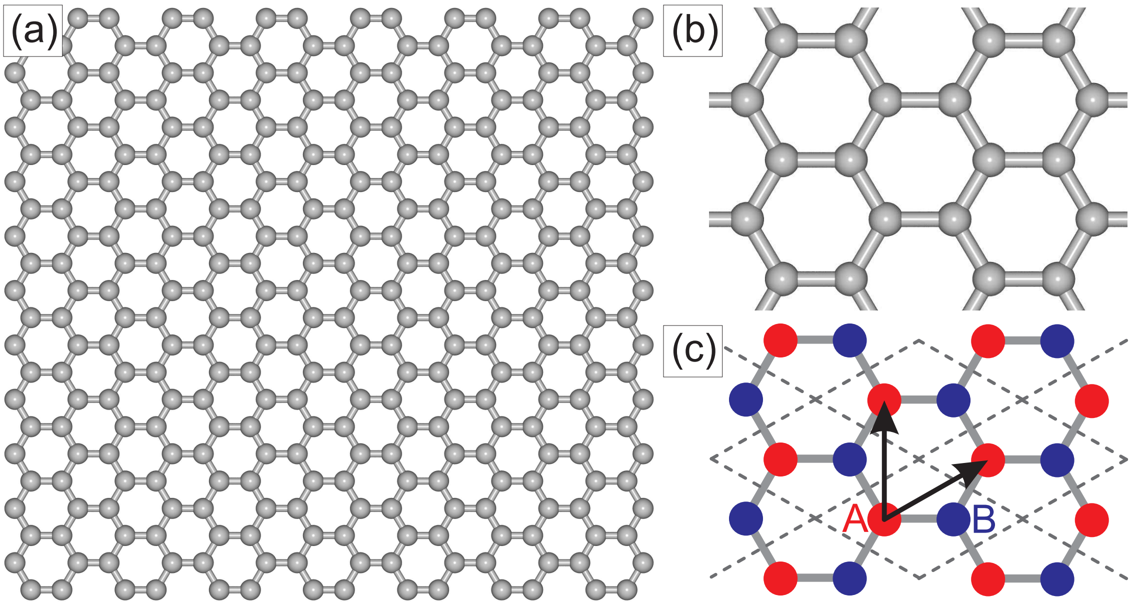

Figure 2.1: *(a) Graphene layer: layer of carbon atoms in honeycomb arrangment. (b) Magnified view and (c) explanation of the crystal structure. Unit cells are marked with dashed lines; arrows show unit vectors. Each unit cell contains two carbon atoms marked as 'A' (red) and 'B' (blue). Number of red and blue atoms form two hexagonal sublattices.*

Let $X(r)$ be a normalized wavefunction for the $2p_z$ orbital of an isolated carbon atom of the graphene layer. By Bloch's theorem and because the graphene layer consists of two sublattices A and B (see Fig. 2.1(c)), we have [1, 61]:

$$\psi = \phi_1 + \lambda\phi_2 \tag{2.1}$$

$$\phi_1 = \frac{1}{\sqrt{N}} \sum_A \exp\left[i\mathbf{k}\cdot\mathbf{r}_A\right] X(\mathbf{r}-\mathbf{r}_A) \tag{2.2}$$

$$\phi_2 = \frac{1}{\sqrt{N}} \sum_B \exp\left[i\mathbf{k}\cdot\mathbf{r}_B\right] X(\mathbf{r}-\mathbf{r}_B) \tag{2.3}$$

where N is the number of unit cells in the crystal.

Substitute 2.1 in the Schrödinger equation

$$H\psi = E\psi \tag{2.4}$$

multiply by ϕ_1^* and ϕ_2^* and integrate over all volume. As a result we get:

$$\begin{cases} H_{11} + \lambda H_{12} = ES_{11} + \lambda ES_{12} \\ H_{21} + \lambda H_{22} = ES_{21} + \lambda ES_{22} \end{cases} \tag{2.5}$$

where

$$H_{ij} = \int \phi_i^* H \phi_j d\tau \qquad S_{ij} = \int \phi_i^* \phi_j d\tau \tag{2.6}$$

The atomic wavefunctions $X(\mathbf{r})$ are normilized in such a way that:

$$\int X^*(\mathbf{r}) X(\mathbf{r}) d\tau = 1 \tag{2.7}$$

In this case holds $S_{11} = S_{22} = 1$. We assume also, that there is no direct overlap between atomic wavefunctions of neighbour atoms, thus, $S_{12} = S_{21} = 0$. From the definition of H_{ij} follows that $H_{12} = H_{21}^*$.

It is possible to present equations 2.5 in a matrix form:

$$\begin{pmatrix} H_{11} - E & H_{12} \\ H_{21} & H_{22} - E \end{pmatrix} \begin{pmatrix} 1 \\ \lambda \end{pmatrix} = 0 \tag{2.8}$$

The solution is:

$$E = \frac{1}{2}\left[H_{11} + H_{22} \pm \sqrt{(H_{11} - H_{22})^2 + 4|H_{12}|^2}\right] \tag{2.9}$$

Assuming from the symmetry that $H_{11} = H_{22}$, we get

$$E = H_{11} \pm |H_{12}| \tag{2.10}$$

We omit exchange integrals between atoms that are not neighbours. However, only atoms of sublattice B are the neighbours of atoms of sublattice A and vice versa. In this case the exchange integrals between atoms of the same sublattice are zero and we have

$$H_{11} = \int X^*(\mathbf{r}) H X(\mathbf{r}) d\tau = E_0 \tag{2.11}$$

Thus, for the graphene energy dispersion the main role will be played only by the H_{12} term, so we will skip E_0 and write for simplicity:

$$E = \pm |H_{12}| \tag{2.12}$$

There are three neighbour atoms near any selected atom, their coordinates are:

$$\left(a/\sqrt{3}, 0\right) \qquad \left(-a/2\sqrt{3}, a/2\right) \qquad \left(-a/2\sqrt{3}, -a/2\right) \tag{2.13}$$

where $a = 2.46$ Å lattice constant of graphene (shown by black arrows in Fig. 2.1(c)).

Inserting coordinates 2.13 into 2.2 and 2.3 and simplifying trigonometrical expressions we obtain the energy dispersion:

$$E(\mathbf{k}) = \pm\gamma\sqrt{1 + 4\cos^2(\frac{a}{2}k_y) + 4\cos(\frac{a}{2}k_y)\cos(\frac{\sqrt{3}a}{2}k_x)} \tag{2.14}$$

where $\gamma \approx 2.8$ eV is the nearest-neighbour hopping energy:

$$\gamma = \int X^*(\mathbf{r} - \rho) H X(\mathbf{r}) d\tau \tag{2.15}$$

and ρ is the vector to nearest neighbours.

The energy dispersion 2.14 is shown in Figure 2.2. There are occupied π and unoccupied π^* bands touching each other at 6 so-called Dirac points located at the $\overline{\mathrm{K}}$ points of the graphene Brillouin zone. A magnified view near the $\overline{\mathrm{K}}$ point is presented in Fig. 2.2(c), where the dispersion looks like a cone. For ideal freestanding graphene, the Dirac points are exactly at the Fermi level. Therefore, graphene is a zero gap semiconductor or semimetal. To prove that the dispersion is in fact a cone, one can calculate the dispersion behaviour near the $\overline{\mathrm{K}}$ point by inserting $\mathbf{k} = (k_x, k_y) = \mathbf{K} + \mathbf{q}$ into equation 2.14, where $\mathbf{q}$ is a momentum relative to $\overline{\mathrm{K}}$ and has a small magnitude ($|\mathbf{q}| << |\mathbf{K}|$). Using $\sin(x) \approx x$

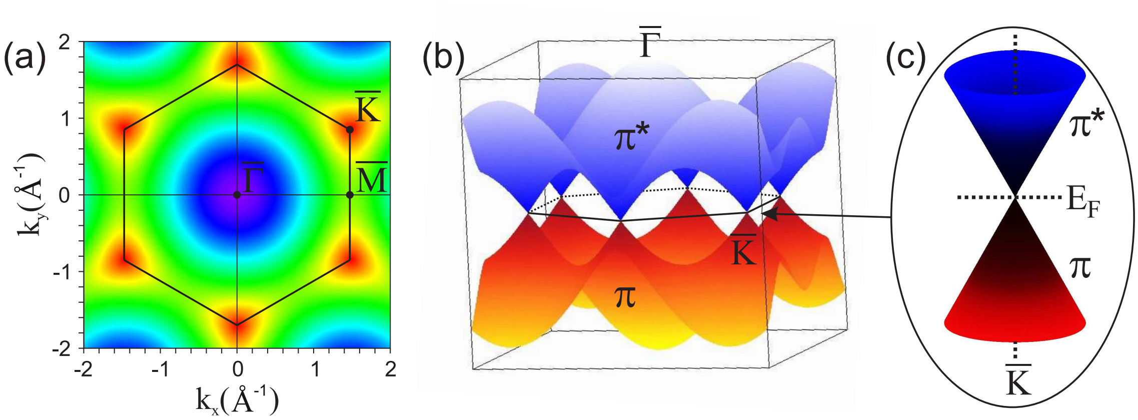

Figure 2.2: *Graphene Brillouin zone (a) and electronic structure (b). Top (blue) band is π^* unoccupied band, bottom (red) is occupied π band. At $\overline{\mathrm{K}}$ points they touch each other at the Dirac points located at the Fermi level. At (c) magnified view of the $\overline{\mathrm{K}}$ point is shown, the so-called Dirac cone.*

and $\cos(x) \approx 1 - x^2/2$ one gets:

$$E(\mathbf{q}) \approx \pm\frac{\sqrt{3}}{2}\gamma a|\mathbf{q}| = \pm\upsilon_F|\mathbf{q}| \tag{2.16}$$

Thus, near the $\overline{\mathrm{K}}$ point there exists a linear $E(\mathbf{q})$ dispersion. $\upsilon_F \approx 1\times10^6$ m/s is the corresponding Fermi velocity.

The linear energy dispersion is very unusual for the electronic structure of materials. It is a distinctive feature of relativistic Dirac fermions with zero rest mass [13], as it appears to neutrinos. Fermi velocity here plays the role of an effective speed of light.

2.2 Rashba Effect

2.2.1 Rashba effect in case of 2D electron gas

The Rashba effect is very important for spintronics and other applications, because it creates a spin polarization of electronic states in nonmagnetic systems. The effect was discovered by Emmanuel I. Rashba and published in 1960 [19]. The Rashba splitting manifests itself predominantly in the case of two-dimentional electron gas (2DEG) systems, like surface states of metals, quantum wells, semiconductor heterostructures, thin metallic films and graphene [20–26].

It is known, that a magnetic field affects electrons and leads in atoms to the so-called *Zeeman splitting* of spin up and spin down electron states. Surprisingly, a splitting of electron states appears also when the electron moves in zero magnetic field, but in a

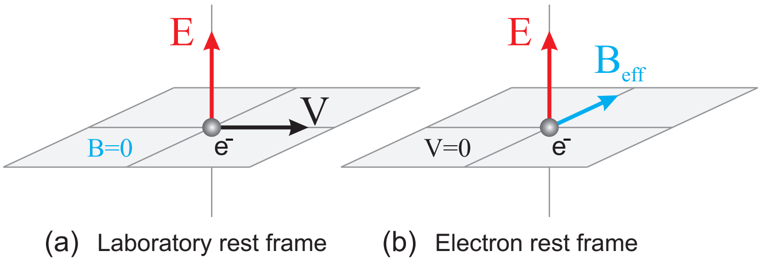

(a) Laboratory rest frame (b) Electron rest frame

Figure 2.3: *Travel of an electron in perpendicular electric field seen in (a) laboratory rest frame and (b) electron rest frame. In the latter case an effective magnetic field* $\mathbf{B}_{eff}$ *appears.*

non zero external electric field. In this case the *effective magnetic field* plays a role, which appears from the electron's point of view (electron rest frame), Figure 2.3. If in the laboratory rest frame the electron moves with velocity **v** in a perpendicular external electric field **E**, then the effective magnetic field is:

$$\mathbf{B}_{\mathtt{eff}} = \frac{1}{c^2}\mathbf{E}\times\mathbf{v} \tag{2.17}$$

Based on the Dirac equation it is possible to extend the hamiltonian for the case of spin-orbit coupling:

$$\mathbf{H}_{\mathsf{SO}} = -\frac{e\hbar}{4m_e^2c^2}\sigma(\mathbf{E}\times\mathbf{p}) = -\frac{\mu_{\mathsf{B}}}{2m_ec^2}\sigma(\mathbf{E}\times\mathbf{p}) \tag{2.18}$$

where μ_{B} is the Bohr magneton, m_e the mass of electron, **p** the electron momentum, and $\sigma = (\sigma_x, \sigma_y, \sigma_z)$ the vector of Pauli matrices, which is directly related to the spin operator: $\hat{\mathbf{S}} = \frac{\hbar}{2}\sigma$.

$$\sigma_x = \begin{pmatrix} 0 & 1 \\ 1 & 0 \end{pmatrix} \qquad \sigma_y = \begin{pmatrix} 0 & -i \\ i & 0 \end{pmatrix} \qquad \sigma_z = \begin{pmatrix} 1 & 0 \\ 0 & -1 \end{pmatrix} \tag{2.19}$$

The last part of equation 2.18 is the effective magnetic field discussed above.

When electrons move in a 2-dimensional plane with momentum $\mathbf{p} = \hbar\mathbf{k} = \hbar(k_x, k_y, 0)$ and the external electric field $E = (0, 0, E_z)$ is normal to that plane, then the hamiltonian 2.18 transforms into:

$$\mathbf{H}_{\mathsf{SO}} = \frac{\hbar\mu_{\mathsf{B}}}{2m_ec^2}E_z(\sigma_xk_y - \sigma_yk_x) = \alpha_R(\sigma_xk_y - \sigma_yk_x) = \alpha_R\begin{pmatrix} 0 & k_y + ik_x \\ k_y - ik_x & 0 \end{pmatrix} \tag{2.20}$$

The constant α_R is also called *Rashba parameter* and depends linearly on the electric field

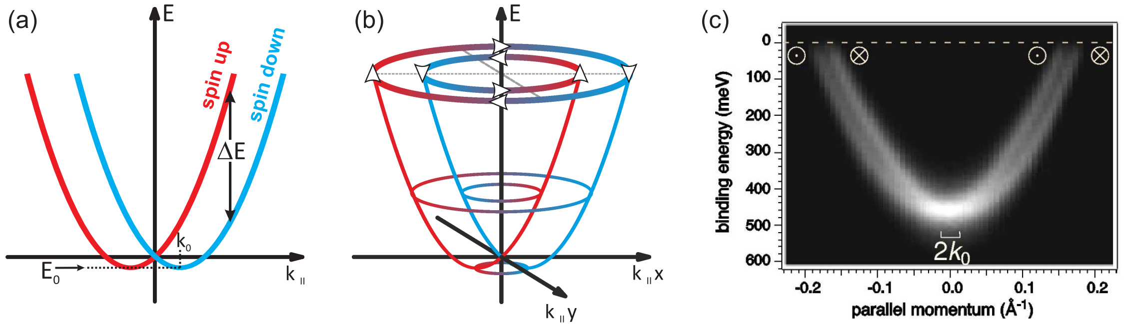

Figure 2.4: *(a) Spin-splitting of free electron parabola to two components with opposite spin: red - spin up and blue - spin down. (b) Same, but shown in two $k_{\|}$ dimentions. Arrows on top show spin-directions at different points, spin rotates when one goes around E axis. (c) Experimental observation by ARPES of spin-splitted surface state bands of Au(111). Figure (c) was taken from ref. [62]*

E_z normal to the surface or in other words, on the potential gradient $-\frac{\partial\Phi(z)}{\partial z}$. Eigenvalues are $\pm\alpha_R\sqrt{k_x^2+k_y^2} = \pm\alpha_R k_{\|}$

Due to this dependence of the Rashba parameter on the potential gradient normal to the surface, the Rashba effect appears under nonsymmetrical conditions. Time reversal symmetry demands that $E(k,\uparrow) = E(-k,\downarrow)$ [22], inversion symmetry means that $E(k,\downarrow) = E(-k,\downarrow)$. Together these equations give $E(k,\uparrow) = E(k,\downarrow)$, i.e., in a system with inversion symmetry spin up and spin down bands degenerate. In two-dimentional planes like surfaces and interfaces when different materials are present or their conditions differ on different sides of the plane, a potential gradient appears, the Rashba parameter becomes nonzero, and $E(k,\uparrow) \neq E(k,\downarrow)$.

In the case of a two-dimentional free electron gas, the full solution is represented by two parabolic bands with opposite spins shifted by $k_{\|}$ relative to each other, see Figure 2.4:

$$E_{\pm}(k_{\|}) = \frac{\hbar^2 k_{\|}^2}{2m_e} \pm \alpha_R k_{\|} \tag{2.21}$$

These parabolas have minima at $\pm k_0$ with energy E_0:

$$k_0 = \frac{m_e\alpha_R}{\hbar^2} \qquad E_0 = -\frac{m_e\alpha_R^2}{2\hbar^2} \tag{2.22}$$

The energy splitting between spin up and spin down is $\Delta E(k_{\|}) = 2\alpha_R k_{\|}$, i.e., has a linear dependence $k_{\|}$, and reverses with $k_{\|}$.

Figure 2.4(a) shows a model of Rashba-split free electron parabolas $E_{\pm}(k_{\|})$ and Fig. 2.4(b) shows a three-dimentional view on these. Arrows at the top show how the spins rotate about $k_{\|} = 0$ and transform from spin up on one side to spin down on the other side.

Figure 2.4(c) was taken from [62] and shows the experimental observation of spin-split Au(111) surface states by angle-resolved photoemission.

As was discussed above, the electric field E_z normal to the surface or interface plays the main role for existence and size of the Rashba effect. There are several possibilities for their origin:

1. applied external electric field
2. workfunction step at the sample surface or interface between two materials
3. high nuclear charge.

The workfunction step leads to splittings of the order of 10^{-6} eV on the Fermi level [22]. This is much smaller than the experimentally observed values on surfaces of high-Z materials. For example, the energy splitting of Au(111) surface state close to the Fermi is ≈ 0.1 eV [21, 62].

The nuclear charge explains the large spin-orbit splitting in the case of high-Z materials. The surface state wavefunction is not perfectly two-dimensional, but spreads normal to the surface into the region of the nuclear potential, which is proportional to Z and is much larger than size of the workfunction step. More detailed model takes atomic spin-orbit splitting into account. In the case of gold, the spin-orbit splitting of the $6p$ level is 0.47 eV [63]. The Hamiltonian for spin-orbit coupling modifies to [44, 64]:

$$H'_{SOC} = \frac{\xi}{\hbar} L \cdot \sigma \tag{2.23}$$

where ξ is of order of atomic spin-orbit splitting. Then energy splitting is:

$$\Delta E(k_{\|}) \approx 2\xi k_{\|} \tag{2.24}$$

and gives result close to experimental values for high-Z materials.

2.2.2 Rashba effect in case of graphene

To discuss the case of graphene properly, we must separate the spin-orbit coupling effects into *intrinsic* and *extrinsic* ones. Intrinsic spin-orbit coupling is related to the graphene layer itself without influence from the environment, such as substrate or external fields. The intrinsic spin-orbit coupling in graphene is very weak with splittings of the order of 0.05 meV or even less [65, 66]. For spintronics such weak spin-orbit coupling is advantageous because it leads to a long spin coherence length of $\sim$1.5–2 μm [32–34]. Theoretically, the spin coherence length could even be 10 times higer [35] and, therefore, there is still room for future implementation of graphene as a possible element in spintronics devices. An externally induced spin-orbit splitting could occur if the graphene layer is in contact with a specific substrate or there are impurities on or in the graphene [7, 67]. A

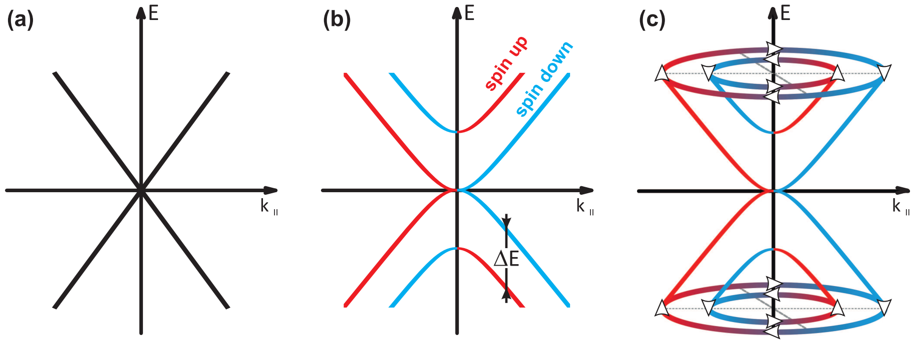

Figure 2.5: *(a) Dirac cone of free graphene without spin-orbit interaction. (b,c) Two- and three-dimensional view of the graphene band structure near the* $\overline{\mathrm{K}}$ *point in the presence of extrinsic (Rashba) spin-orbit coupling.*

large spin-orbit coupling in graphene could open the way for graphene as active element of spintronic devices such as the Datta-Das spin field-effect transistor [30]. Recently, we observed that a large Rashba-type spin-orbit coupling can be induced in thin metal films due to interaction with a high-Z substrate [45, 47] and that this works for graphene as well [7]. In the present thesis and in the corresponding publication [68] we discuss the observation and the origin of a giant Rashba splitting of the Dirac cone when the graphene layer is located on top of gold or iridium substrates.

In the case of a conventional two-dimensional free electron gas the Rashba effect is observed at the $\overline{\Gamma}$ point of the Brillouin zone as a $k_{\|}$ shift of parabolic bands of different spin in opposite directions. Therefore the energy splitting depends linearly on the $k_{\|}$ value. In the case of a spin-orbit split graphene Dirac cone there are many differences. First of all, the Dirac cones in the graphene electronic structure are located far away from the $\overline{\Gamma}$ point, i.e., at six $\overline{\mathrm{K}}$ points as shown in Figure 2.2. Secondly, the split bands resemble near $\overline{\mathrm{K}}$ the peculiar band structure of bilayer graphene [69], with an energy gap between upper and lower branches of one spin and no gap between branches of the other spin [70]. And finally, the energy splitting between spin up and spin down bands for the case of graphene is constant, i.e. there is no $k_{\|}$ dependence of energy splitting. Such behaviour was calculated in Ref. [70] based on a 4×4 Hamiltonian of graphene with extrinsic spin-orbit coupling from Ref. [40]:

$$H = \hbar \upsilon_F (\sigma \cdot k) + \frac{1}{2}\lambda(\sigma \times s)_z \tag{2.25}$$

Here, υ_F is the Fermi velocity, λ is a spin-orbit coupling constant, σ are Pauli matrices for the pseudospin, and s are Pauli matrices for the real spin.

The resulting equations for the band structure around the $\overline{\mathrm{K}}$ point are [70]:

$$E_{\nu\mu}(k) = \frac{\nu\mu}{2}\left(\sqrt{\lambda^2 + (2\hbar\upsilon_F k)^2} - \mu\lambda\right) \tag{2.26}$$

where $\mu = \pm 1$ corresponds to spin and $\nu = \pm 1$ to chirality. The spin-orbit splitting is $\Delta E = |\lambda|$ and is constant. Spins are in-plane and rotate about the $\overline{\mathrm{K}}$ point. A graphical presentation of this solution is shown in Figure 2.5. In panel (a) there is the Dirac cone of free graphene without spin-orbit interaction. In panels (b) and (c) there is the Dirac cone for the case of an externally induced spin-orbit splitting. The panel (b) shows this in a two-dimensional cut view and the panel (c) in a three-dimensional view. Pure blue and red colours denote spin directions towards the viewer and away from the viewer, normal to the image surface. It has been found that the photoemission process could be affected by interference as due to the A–B sublattices influencing the photoemission intensity and the observed spin-polarization direction [71]. For the valence band electrons the main influence of such interference is in the $\overline{\Gamma\mathrm{K}}$ direction but beyond the $\overline{\mathrm{K}}$ point. Spin-resolved photoemission measurements are usually conducted in other directions and the giant spin rotation effect proposed in Ref. [71] has not yet been observed experimentally.

CHAPTER 3

GRAPHENE ON FERROMAGNETS

3.1 Introduction

We discussed in the previous section that the Rashba effect depends strongly on the potential gradient normal to the surface and that there are several possible sources of such gradient such as: (i) applied external electric field, (ii) workfunction step at the sample surface, (iii) nuclear potential of high-Z substrate atoms. If the graphene π band wave function spread into the location of substrate atom wave functions, a contribution from the potential gradient around the nuclei of the substrate atoms becomes possible. This is possible by hybridization between the graphene π band and substrate bands. For materials with higher atomic number Z the effect will be larger than for materials with low atomic number, thus, for low-Z substrates under the graphene layer we can straightforwardly predict the absence of a Rashba effect and spin-split bands in the graphene band structure. Despite this reasoning, several experiments indicating the opposite appeared in the literature. In graphene on nickel a large energy shift up to 255 meV of the graphene π band was observed by angle-resolved photoemission when the magnetization of the graphene/Ni(111) system is reversed [72]. In graphene grown by thermal decomposition on SiC an anisotropic spin splitting of the π band of up to $\sim$200 meV was observed by spin- and angle-resolved photoemission [73].

In order to study ways to externally induce and control the spin polarizaton and spin-orbit splitting of the electronic bands in graphene we need to examine these effects. We conducted a number of experiments by means of the spin- and angle-resolved photoemission of graphene on different substrates, both low-Z and high-Z. Results of our study concerning of giant energy shift Ref. [72] were presented before [74, 75]. In the current chapter we will investigate graphene on ferromagnets (nickel and cobalt) in various ways regarding their electronic and spin structure.

3.2 Preparation

Several methods of graphene preparation are known with different methods more or less suitable for different substrates. The graphene monolayer on Ni(111) was already prepared and studied in the 1970s by segregation of carbon atoms from the bulk to the nickel surface [2], later by the so-called *cracking* procedure [3–7, 10, 76] and by thermal decom-

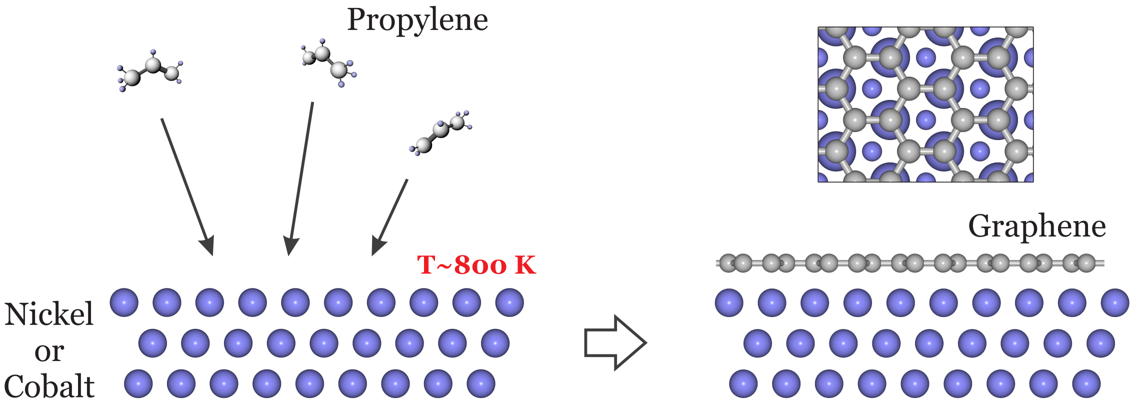

Figure 3.1: *Procedure of Propylene (C_3H_6) cracking and the resulting structure of graphene. In the inset, larger substrate atoms indicate the top Ni (Co) layer, smaller ones the second layer, and the third layer atoms are hidden under the carbon atoms.*

position of SiC [8, 9, 77]. Later a micromechanical cleavage method using bulk graphite was shown [11, 13].

We used the cracking procedure to grow graphene on nickel and cobalt surfaces due to the simplicity of this method and the large scale high quality graphene layers that are obtained as a result. This method is shown schematically in Figure 3.1. The sample is heated by the electron bombardment method to ~ 800 K and propylene gas (C_3H_6) at pressures around 10^{-6} mbar is introduced into the vacuum chamber for 5 min. Propylene molecules in contact with the hot Ni or Co surface break up and the carbon atoms assemble to form the graphene layer. This process is self-limiting and only one graphene layer grows due to the fact that Ni and Co atoms on the surface serve as catalyst for the cracking of the C_3H_6 molecules. So, after the first graphene layer is formed, it cannot catalyze the formation of a second layer. There is still the possibility that more graphene layers could form at the interface between Ni or Co and the graphene layer due to carbon atoms segregating from the bulk of nickel and cobalt but higher temperatures and longer heating time are needed for this to happen. The self-limitation of the graphene growth is an advantage of this method over other graphene growth methods such as the thermal graphitization of SiC.

The structure of the resulting graphene layer is shown at the right side of Figure 3.1. Carbon atoms are on top of the Ni atoms; the second Ni layer atoms are under the centers of graphene hexagons. This structure is based on the LEED intensity analysis made in Ref. [78] and confirmed directly by STM for graphene islands on top of Co(0001) [79].

Due to technological reasons and better structural quality the Ni(111) and Co(0001) substrates were $\sim 15-20$ monolayer thick films grown on W(110) crystal surface. Tungsten was cleaned by cycles of oxygen treatments at ~ 900 K and *flashes* (short heating to ~ 2000 K) to remove carbide and to remove adsorbed oxygen, respectively. Nickel

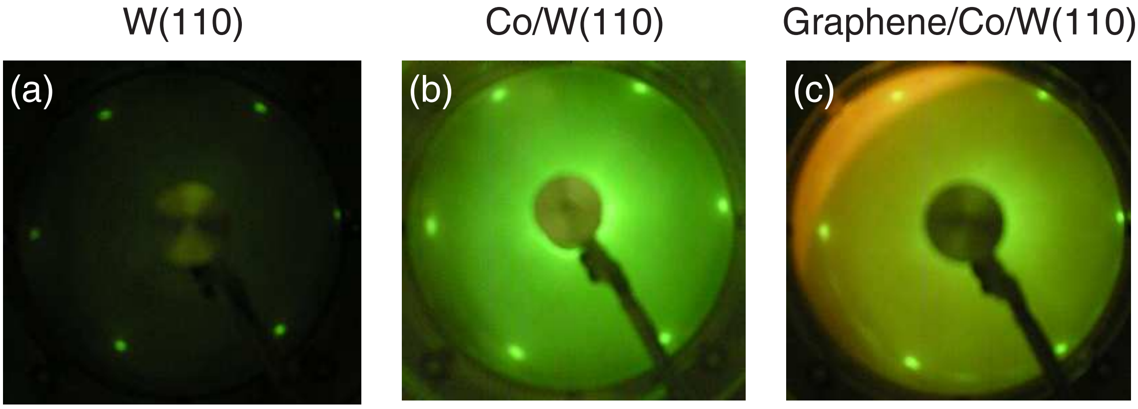

Figure 3.2: *Low-Energy Electron Diffraction images from (a) W(110), (b) Cobalt film on W(110) and (c) graphene/Co(0001)/W(110).*

and cobalt films were deposited from electron beam evaporotors and were subsequently annealed.

The quality of the tungsten surface, the nickel (cobalt) films and of the resulting graphene layer was checked by LEED and photoemission (ARPES and XPS). Figures 3.2(a-c) show LEED images from the clean W(110) surface, a Co(0001) film and from graphene on cobalt, respectively. Tungsten has a body-centered cubic crystal structure, the LEED image from its clean (110) surface appears like a hexagon, but is streched-out in one direction. In XPS the cleanliness of the tungsten surface is clearly visible by the presence of surface components of the W $4f$ core levels, see Figure 3.3. In the presence of carbide there is an additional complicated structure of spots in the LEED image, in the presence of oxygen there is a clear (2×2) reconstruction. Near the W $4f$ core levels additional peaks at higher binding energies appear and surface components have smaller intensity or fully disappear. Nickel has a cubic close-packed crystal structure, cobalt has a hexagonal close-packed crystal structure, but both Ni(111) and Co(0001) surfaces which are obtained by growing nickel and cobalt on the tungsten (110) surface have a hexagonal atomic arrangment and the LEED patterns are hexagons.

There is only a small mismatch $\sim 2\,\%$ between the graphene lattice constant and surface lattices Ni(111) and Co(0001). Thus, graphene on these surfaces grows with high quality and in registry with substrates. The orientation of the graphene layer is fully consistent on the whole sample area and from experiment to experiment; it is related to the direction of the underlying W crystal. In the LEED image from graphene on cobalt (Figure 3.2(c)) there are additional circle segments which correspond to the presence of rotated graphene domains, but these segments are weak meaning that the number or size of the rotated domains is small.

The Scanning Tunneling Microscopy (STM) characterization of graphene/Ni(111) and graphene/Co(0001) shows good quality of graphene layer, Figure 3.4. STM images show

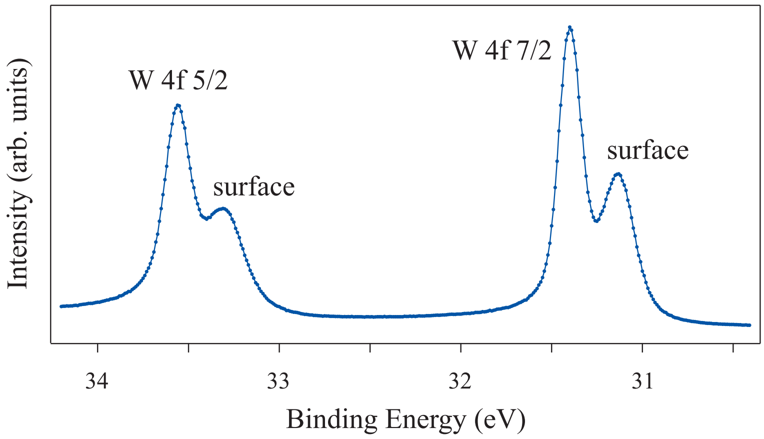

Figure 3.3: *Tungsten W 4f core levels measured at* $h\nu = 110$ *eV photon energy. Such spectrum is very useful for the check of the W(110) surface quality. If the surface is clean there are sharp and intence surface components near the main bulk core peaks.*

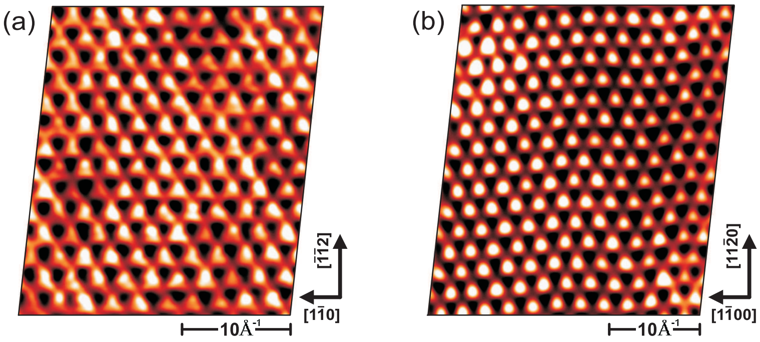

Figure 3.4: *STM from graphene on Ni(111) (a) and on Co(0001) (b). Tunneling parameters:* $V_t = +2$ *mV,* $I_t = 25$ *nA.*

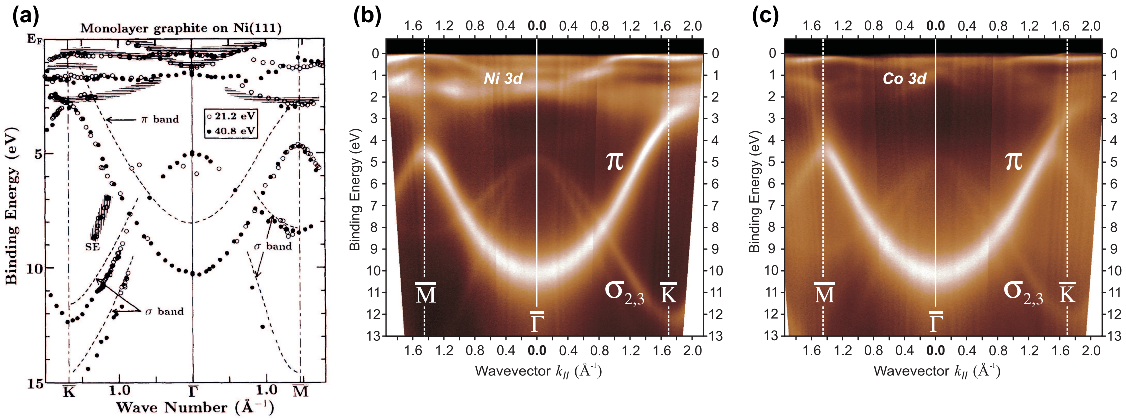

Figure 3.5: *(a) Open and filled circles denote the experimental band structure of graphene/Ni(111), broken curves indicate bulk graphite dispersion and dashed areas near the Fermi level show Ni d states. Figure (a) is from ref. [4], photon energies are* $h\nu = 21.2$ *and* 40.8 *eV. (b) Angle-resolved photoemission data of graphene/Ni(111) and (c) of graphene/Co(0001). Photon energy* $h\nu = 62$ *eV.*

also that there is no sixfold symmetry as would be expected for a free graphene layer, but a threefold symmetry is observed. This is evidence for symmetry breaking between *A* and *B* graphene sublattices, i.e., carbon atoms of one graphene sublattice are on top of the nickel or cobalt atoms and carbon atoms of the other sublattice are on top of the third layer atoms of the substrate (see Fig. 3.1).

3.3 Electronic structure and intact Dirac cones

The electronic structure of graphene on nickel is characterized by a large shift of the graphene π band to higher binding energy as compared to the electronic structure of the free graphene layer [4, 7, 76, 80]. Figure 3.5(a) shows the experimental band structure of the graphene/Ni(111) system obtained by photoelectron spectroscopy with He I ($h\nu = 21.2$ eV) and He II ($h\nu = 40.8$ eV) excitation sources. The Figure is from the first investigation of this system in Ref. [4]. In the present work the electronic structures of graphene on Ni(111) and graphene on Co(0001) systems were studied and results are presented in Figure 3.5 panels (b) and (c), respectively. The presented measurements were performed in the $\overline{\Gamma M}$ and $\overline{\Gamma K}$ directions of the graphene Brillouin zone. One can see Ni (Co) *d* states near the Fermi level and two graphene σ bands dispersing from 5 eV to higher binding energies. The graphene π band reaches from ~ 10 eV at the $\overline{\Gamma}$ point up to ~ 4.5 eV at the $\overline{M}$ point, and up to ~ 3 eV at the $\overline{K}$ point. After crossing of the Brillouin zone border at the $\overline{K}$ point, the graphene π band hybridizes with Ni (Co) *d* states. The strong shift of the graphene π band by ~ 2 eV as compared to the case of free graphene and graphite (dashes in Figure 3.5) and clearly visible effects of hybridization with Ni (Co) states indicate a strong interaction of the graphene layer with the substrate.

From first sight, there is no apparent Dirac-cone-type dispersion around the $\overline{\mathrm{K}}$ point and for a long time it was believed that the Dirac cone is destroyed in these systems due to strong graphene-Ni (Co) interaction and a resulting breaking of the symmetry between A and B sublattices [6, 81]. Density functional theory (DFT) and tight binding calculations also showed a large gap at the $\overline{\mathrm{K}}$ point [38, 82]. Despite this, a thorough view at the experimental data, both ours and that published by other groups, shows that the graphene π band crosses the $\overline{\mathrm{K}}$ point without any break or detectable gap there. To study such unexpected behaviour, we conducted a full angle-resolved photoemission mapping of the region around the $\overline{\mathrm{K}}$ point for both graphene on nickel and graphene on cobalt as well as and high-resolution angle-resolved measurements through the $\overline{\mathrm{K}}$ point in the direction normal to $\overline{\Gamma\mathrm{K}}$. The results are published [83] and shown in Figures 3.6(a-d). The measurements were conducted at various photon energies both at room temperature and at low temperature to improve the energy resolution and to test the effect of the thermal lattice expansion on the electronic structure. The intact Dirac cone is visible with an intense Dirac point at 2.84 eV binding energy. The enhancement of intensity exactly at the Dirac point tells us that there is no gap. In Figures 3.6(e-f) the same structure of the intact Dirac cone is observed for the case of graphene on cobalt. The Dirac point is at 2.82 eV binding energy. The measurement direction is schematically shown in panel (g). The reason why the Dirac cone is not observed in the dispersion in the $\overline{\Gamma\mathrm{K}}$ direction is a destructive interference of photoelectrons from two graphene sublattices. This effect has been studied in graphite [84]. At the crossing from the first into the second Brillouin zone in the $\overline{\Gamma\mathrm{K}}$ this interference has the effect that in the first Brillouin zone (before the $\overline{\mathrm{K}}$ point) only the graphene π branch is visible and the π^* branch is not visible, but in the second Brillouin zone after the $\overline{\mathrm{K}}$ point the opposite happens. Due to this effect in the $\overline{\Gamma\mathrm{K}}$ direction Dirac cone is not recognized, but only one graphene band which is π before the $\overline{\mathrm{K}}$ point and π^* after. In the measurements normal to the $\overline{\Gamma\mathrm{K}}$ direction both sides of the dispersion are in fully symmetrical conditions, so that both π and π^* branches are fully visible and the Dirac cone and Dirac point are observed. The presence of this strong interference effect indicates that the observed Dirac-cone-like band structure is from the graphene layer, not from the nickel (cobalt) substrate. No measurements of these systems in such symmetrical direction were done before. A sampling of the Dirac cone at different photon energies as presented in Figures 3.6(a-d) shows an energy shift of the nickel states with the photon energy or, in other words, shows a dispersion of nickel states in the $k_\perp$ direction. But at the same time the Dirac point and Dirac cone positions and shape are preserved confirming the two-dimensional nature. This additionally proves that the observed Dirac-cone-type band structure originates from graphene and not from the bulk nickel (cobalt) states.

Thus, our measurements clearly show the presence of intact Dirac cones in systems where the symmetry between A and B graphene sublattices is broken. Also a strong n-doping of graphene with the 2.82-2.84 eV shift of the Dirac point to higher binding

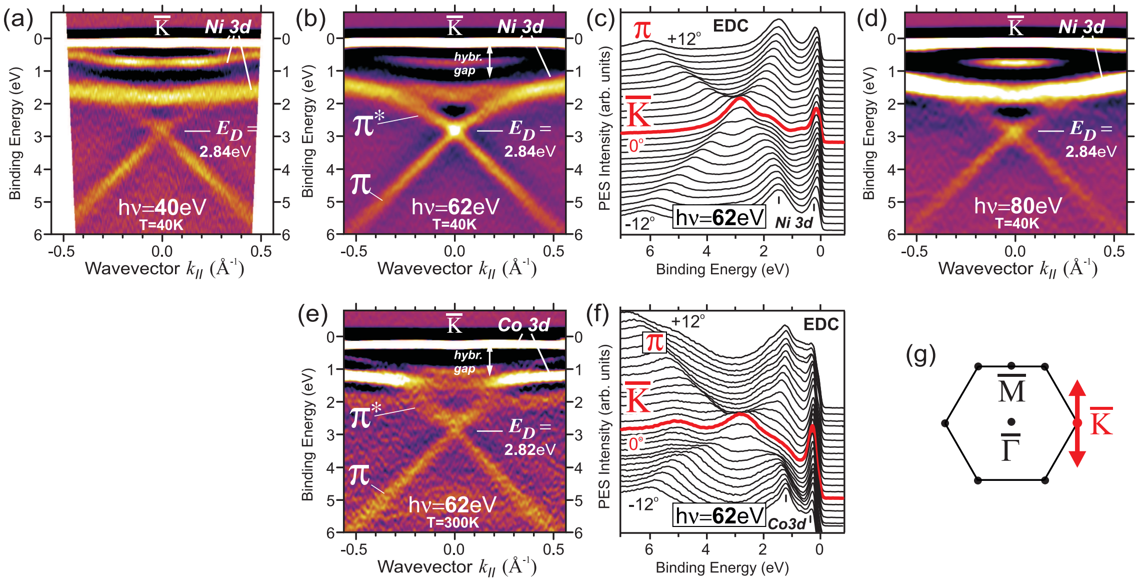

Figure 3.6: *Experimental band structure normal to the $\overline{\Gamma K}$ direction through the $\overline{K}$ point for (a-d) graphene/Ni(111) and (e-f) graphene/Co(0001). The presented band structures were measured at room temperature in the case of graphene on cobalt and at low temperature (~ 40 K) in the case graphene on nickel. In panels (a,b,d,e) the second derivative of photoemission intensity over energy is presented. Panels (c) and (f) show line cuts (energy distribution curves, EDC) of raw data from panels (b) and (e). The intact Dirac cone is clearly visible in all of the presented figures. (g) Schematic view of the measurement direction.*

energies is observed. A giant hybridization gap is in fact also observed, but it is located at binding energies lower than 2 eV (see Figures 3.6(b) and (e)) and away from the Dirac point. Note that this gap is a common hybridization effect not related to the effects of sublattice symmetry breaking and opening of a gap at the Dirac point.

3.4 Absence of Rashba effect

As mentioned above, in graphene on nickel a large energy shift up to 255 meV of the graphene π band was observed by angle-resolved photoemission as a result of reversal of the magnetization orientation of the graphene/Ni(111) system [72]. The results were interpreted as showing a Rashba effect in a ferromagnet and it was supposed that the graphene π states become spin-polarized due to hybridization with the Ni substrate. Controlling of the spin of electrons in graphene by the external magnetic field which switches the magnetization of the nickel could be important for spintronics applications, but the measurements of Ref. [72] do not include a direct proof by spin-resolved photoemission of the presence of spin polarization or spin-splitting in the graphene. To check that the observed energy shift has some relation to the electron spin we conducted such spin-resolved experiments and showed the absence of any detectable spin-orbit splitting of the graphene π band. Those results were published [74] and discussed in a PhD Thesis [75]. In the current chapter the subject will be discussed very shortly because it it is necessary as starting point for the discussions of the spin-resolved data in the following chapter.

Figure 3.7 shows a direct measurement by spin- and angle-resolved photoelectron spectroscopy of the graphene π band at $k_{\|} = 0.7$ Å^{-1} along the $\overline{\Gamma\mathrm{M}}$ direction, i.e., the position where the large shift was observed in Ref. [72]. Blue and red lines are spin up spectrum ($I^{\uparrow}$) and spin down spectrum ($I^{\downarrow}$), respectively. The spin polarization was calculated as

$$p = \frac{I^{\uparrow} - I^{\downarrow}}{I^{\uparrow} + I^{\downarrow}} \tag{3.1}$$

and is presented at the bottom part of the Figure 3.7. There is a strong spin polarization of the nickel 3d states which are located close to the Fermi level, but absolutely no spin polarization or spin splitting of the graphene π band. Thus, the effect reported in Ref. [72] is neither the Rashba nor an exchange interaction effect.

Magnetic moment and exchange splitting of the 3d states of cobalt are ~ 3 times larger as compared to nickel [85, 86]. Thus, if the exchange or Rashba-type splitting of the graphene π band take place in the graphene/Co(0001) system, they should be better visible than in the graphene on nickel case. Based on this, similar experiments with graphene/Co(0001) were done. As was discussed above, geometric and electronic structures of graphene/Ni(111) and graphene/Co(0001) are very similar. But due to the fact that the easy magnetization directions in these systems are rotated by 90° relative to each other, experiments in both $\overline{\Gamma\mathrm{K}}$ and $\overline{\Gamma\mathrm{M}}$ directions were done. The result is same as for the

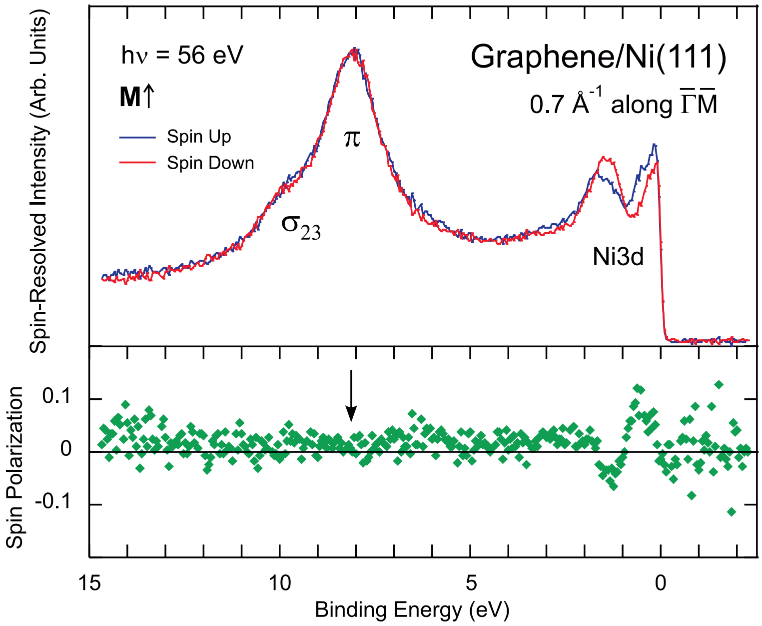

Figure 3.7: *Spin- and angle-resolved photoemission of graphene/Ni(111) measured at* $h\nu = 56$ *eV at* $k_{\|} = 0.7$ Å^{-1} *along the* $\overline{\Gamma\mathrm{M}}$ *direction. Blue and red spectra correspond to opposite spin orientation, the bottom panel shows the spin polarization. The sample was remanently magnetized and the Ni was an epitaxial film on W(110).*

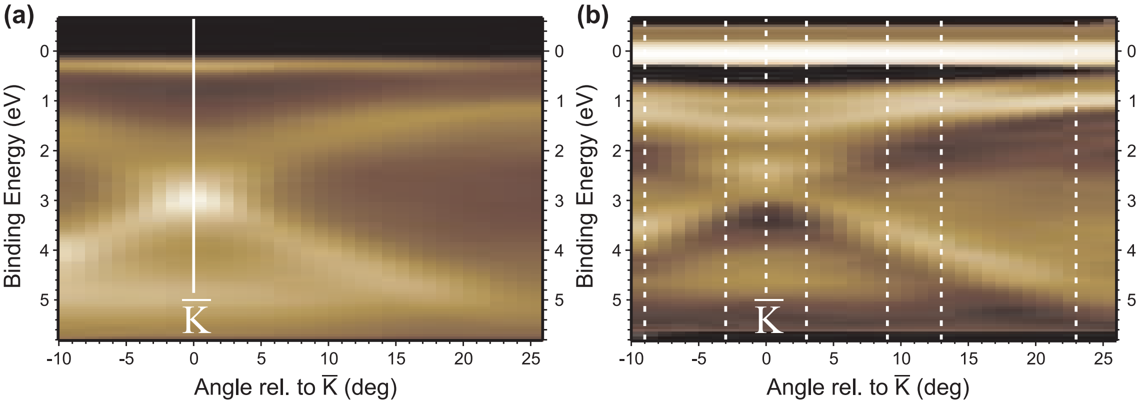

Figure 3.8: *(a) ARPES measurement of graphene/Co around the $\overline{\mathrm{K}}$ point of the graphene Brillouin zone normal to the $\overline{\Gamma\mathrm{K}}$ direction. (b) First derivative of intensity over energy of the data from panel (a). The measurement was done at the spin- and angle-resolved photoemission experimental station and the dashed lines in (b) show where spin-resolved spectra were measured. Photon energy $h\nu = 62$ eV.*

case of graphene on nickel, i.e., absence of the Rashba or exchange-type spin splitting of the graphene π band.

As a final remark it is worthwile to mention that the discussed absence of a Rashba effect in graphene on nickel and cobalt is in agreement with our expectations. In any case it remains possible to use both systems for spintronics as a source of spin-polarized electrons [37], for spin-filters [38] or as a substrate for graphene on other metals like gold [6], copper [80], iron [87] and others with their own peculiar spin properties. We will return to this point and pick two prominent examples in chapters 4.3 and 5.1.

3.5 Dirac cone spin polarization

The above mentioned investigations of the spin splitting of the graphene π band in graphene on ferromagnets were done before we discovered the presence of the intact Dirac cone in these systems. The measurements were done at the $\overline{\Gamma}$ point and other points in the graphene Brillouin zone along different directions. However the main focus was on $k_{\|}$ wave vector values around half the distance from $\overline{\Gamma}$ to $\overline{\mathrm{K}}$ and $\overline{\mathrm{M}}$, because exactly there the maximum effect was predicted in Ref. [72]. After our discovery of intact Dirac cones in graphene on nickel and cobalt [83] we expanded our search for possible spin-related effects in these systems to the region of the Dirac cone and the hybridization of the graphene π band with the nickel (cobalt) 3d states. Due to the fact that magnetic moment and exchange splitting of the 3d states of cobalt are ~ 3 times larger as compared to nickel we selected and studied the graphene on cobalt system.

In Figure 3.8 data from the spin-resolved photoemission experimental station is shown, measured near the $\overline{\mathrm{K}}$ point of the graphene Brillouin zone in the direction normal to $\overline{\Gamma\mathrm{K}}$. This spin-integrated measurements are required to make sure that the spin-resolved spectra probe the Dirac cone. The data as presented as measured in panel (a) and as first derivative over energy in panel (b). At the $\overline{\mathrm{K}}$ point the graphene Dirac point is clearly visible as a bright spot at ~ 2.9 eV binding energy. The enhanced intensity at the Dirac point is reproduced and means that graphene π bands cross at this point without a detectable gap. Dashed lines in Figure 3.8(b) show where the spin-resolved spectra were obtained. We measured the spin-resolved spectra for two opposite magnetization directions of the sample (both magnetizations along the $\overline{\Gamma\mathrm{M}}$ ([$1\bar{1}00$] of Co) direction) and for two light polarizations: linear horizontal (predominantly p type) and linear vertical (s type). In the presented dispersion of Figure 3.8(a,b) we can clearly follow how the graphene π band going from high to low binding energies and after passing the Dirac point starts to hybridize with cobalt 3d states which are located in the region of $\sim 0-2$ eV binding energy. These cobalt states are known to be spin polarized. Note that their spin polarization must reverse when the sample magnetization is reversed. Presence of these spin polarized cobalt states when the graphene layer is on top is by itself interesting for spintronics devices due to theoretical possibility of using these states in spin filter devices [88]. However, the graphene Dirac cone was believed to be destroyed and its possible spin polarization or spin splitting were not studied. From another point of view it would be very promising to detect a spin polarization or spin splitting of the Dirac fermions, because their high mobility could be maintained, especially with the possibility of an external control by electric or magnetic fields. As we discussed before there is no detectable spin splitting or polarization of the graphene π band from the $\overline{\Gamma}$ point up to $\sim 2/3$ of the $\overline{\Gamma\mathrm{K}}$ distance.

Here we focus on the spin-resolved measurements of the π band around the $\overline{\mathrm{K}}$ point. They are presented in Figures 3.9, 3.10, 3.11. The Figure 3.9(a) shows spin-resolved spectra measured at the $\overline{\mathrm{K}}$ point of the graphene Brillouin zone. The red line shows the spin up (majority spin) spectrum, the blue line shows the spin down (minority spin) spectrum. There are:

1. A large spin polarized background (spin down in panel (a)).
2. At ~ 5.2 eV binding energy a trace of the graphene π band dispersion around the $\overline{\mathrm{M}}$ point visible in the $\overline{\Gamma\mathrm{K}}$ direction due to rotated domains. The peak itself is not spin polarized (if one removes the background spin polarization).
3. In the region $\sim 2.4-3$ eV binding energy the graphene Dirac point with dominant spin up polarization is located.
4. From ~ 2 eV and up to the Fermi level there are spin polarized cobalt 3d states.

The observed strong spin polarization of the graphene Dirac point is of significant interest here both from a fundamental point of view and for possible use in spintronics devices. The nature of this spin polarization will be the topic of further verification and discussion in the remainder of this section.

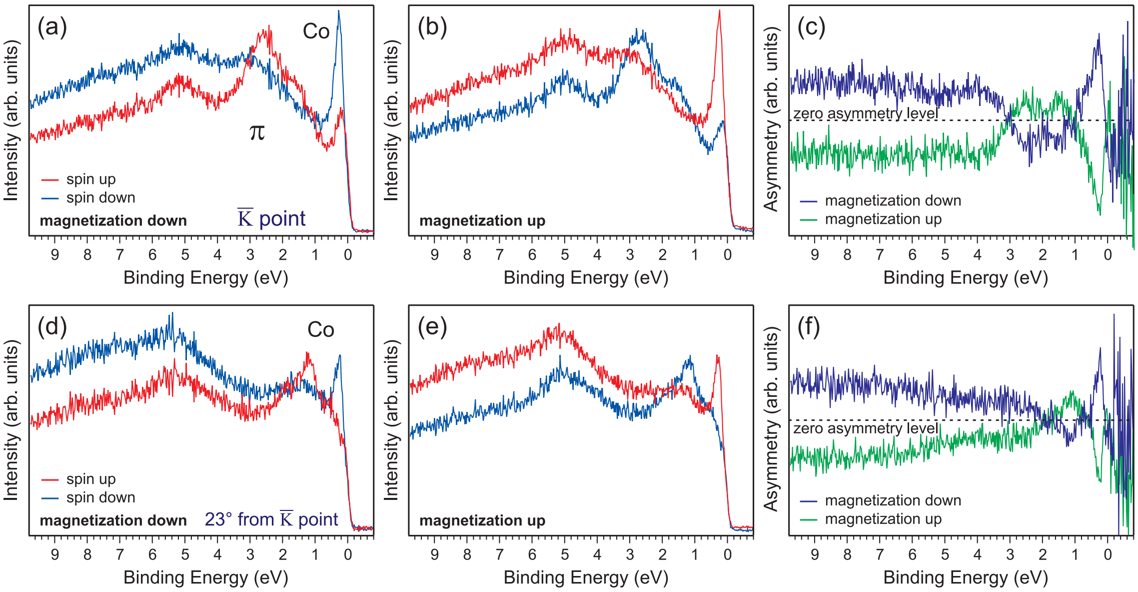

Figure 3.9: *(a,b) Spin-resolved spectra at the* $\overline{\mathrm{K}}$ *point of the graphene Brillouin zone. (a) and (b) were measured for opposite magnetization directions. (c) Asymmetries are shown from panels (a) (blue) and (b) (gren). The zero asymmetry level is shown as dashed line. (d-f) Same for* 23° *away from* $\overline{\mathrm{K}}$ *point.*

At the Figure 3.9(b) spin-resolved spectra similar to the spectra from panel (a) are shown, but measured after reversal of the magnetization. Spectra in panels (a) and (b) are identical, but with spin up and spin down electrons exchanged. In particular the Dirac point spin polarization has reversed together with that of the cobalt states. In panel (c) the spin asymmetries for both magnetization directions are shown. This is required since the background spin polarization as well as the absolute spin polarization of other peaks depend strongly on the correct determination of the *zero asymmetry* level. From a single spin-resolved measurement it is usually not known where the zero asymmetry level is located, and the measurement of both magnetization directions after one another solves this problem in our case as it is visible in panel (c): the zero asymmetry level is located at the symmetry line of both spin asymmetries, or in other words, passes through the points where the asymmetry value does not change after the sample is magnetized in the opposite direction. Figures 3.9(d-f) display the same measurements as (a-c) but for an emission angle 23° from the $\overline{\mathrm{K}}$ point. There only the cobalt 3d states close to the Fermi level visible with which the graphene π band hybridizes. Other angles were measured as well and show a smooth transition from the Dirac point into the cobalt 3d states (spectra not shown here).

As was seen in Figure 3.8 the dispersion and photoemission intensities are symmetrical relative to the $\overline{\mathrm{K}}$ point. We checked if there a reversal of spin polarization of any of the observed bands. The results are presented in Figure 3.10. Spectra for two opposite an-

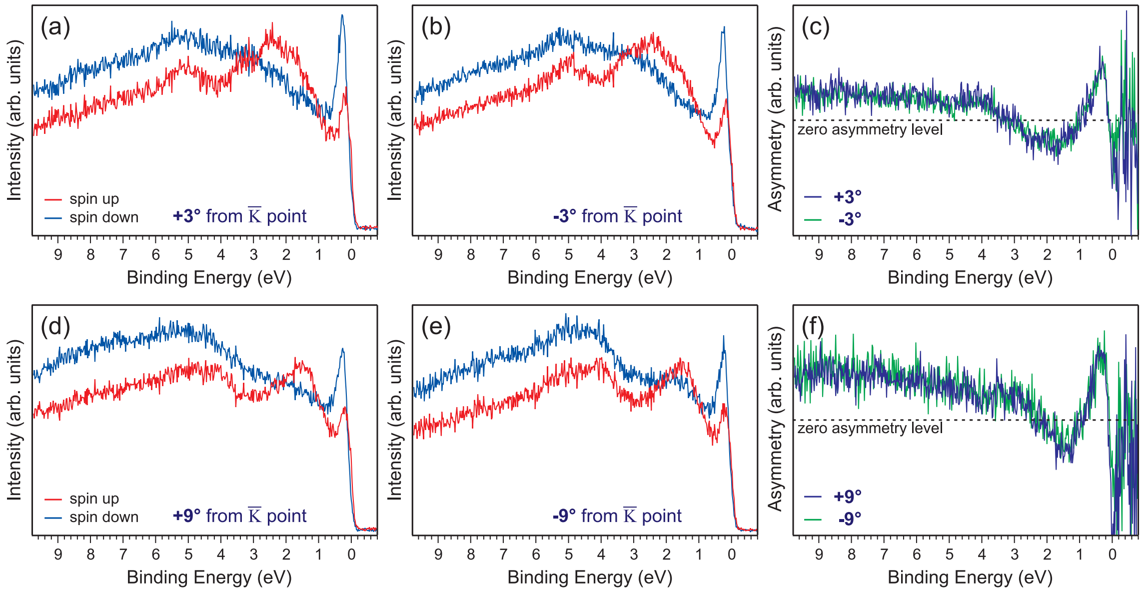

Figure 3.10: *Comparison of spin-resolved spectra for two symmetrically located points relative to the* $\overline{\mathrm{K}}$ *point: (a,b) for ±3° and (d,e) for ±9° from the* $\overline{\mathrm{K}}$ *point. (c,f) Comparison of asymmetries for corresponding opposite points. Spectra and asymmetries are identical.*

gles relative to the $\overline{\mathrm{K}}$ point look identical and their spin asymmetries as well. This means that for both cobalt and graphene the spin polarization is symmetrical relative to the $\overline{\Gamma\mathrm{K}}$ direction. As was shown in section 2.2.2 concerning the Rashba effect, a Rashba-type spin-orbit splitting leads in graphene to the inversion of the spin polarization for two opposite sides of the $\overline{\mathrm{K}}$ point. Our observation of absence of such reversal means that if there is a Rashba-type splitting it is very small, and the measured spin polarization is a ferromagnetic one with the origin in the cobalt 3*d* states. Via spin-dependent hybridization the cobalt 3*d* states polarize the graphene π states.

The graphene π band intensity in the photoemission is very sensitive to the light polarization due to p_z origin of the π band. For the measurement close to the $\overline{\mathrm{K}}$ point the sample has been rotated by a polar angle out of normal. With a linear horizontal (predominantly *p* type) light polarization we reached a minimum angle between the π orbitals and the electric field vector of the incident photon beam thus giving the maximum π band intensity in the photoemission due to matrix element effects. When the light polarization is changed to the linear vertical (*s* type), the π band intensity drops significantly and this helps to separate graphene and cobalt contributions. The comparison of spin-resolved spectra for the two polarizations is shown in Figure 3.11. In panels (a) and (c) the linear horizontal polarization is presented and in panels (b) and (d) the linear vertical one. In the case of vertical polarization the graphene π peak intensity drops down significantly as expected (panel (b)). Such approach makes a preliminary fit of the measured data possible. The

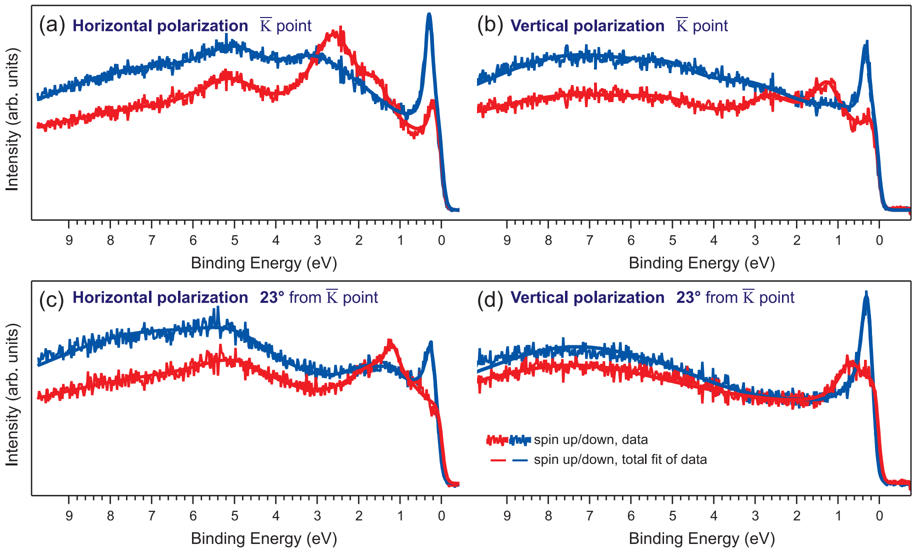

Figure 3.11: *(a,b) Measurements at the* $\overline{\text{K}}$ *point for two light polarizations: (a) standard linear horizontal polarization and (b) linear vertical polarization at wich the graphene* π *band intensity is suppressed. Solid lines are fits of the measured spectra. The fit was conducted at the same time for both polarizations, with identical resulting peaks positions, but different intensities. (c,d) Same for* 23° *away from* $\overline{\text{K}}$ *point.*

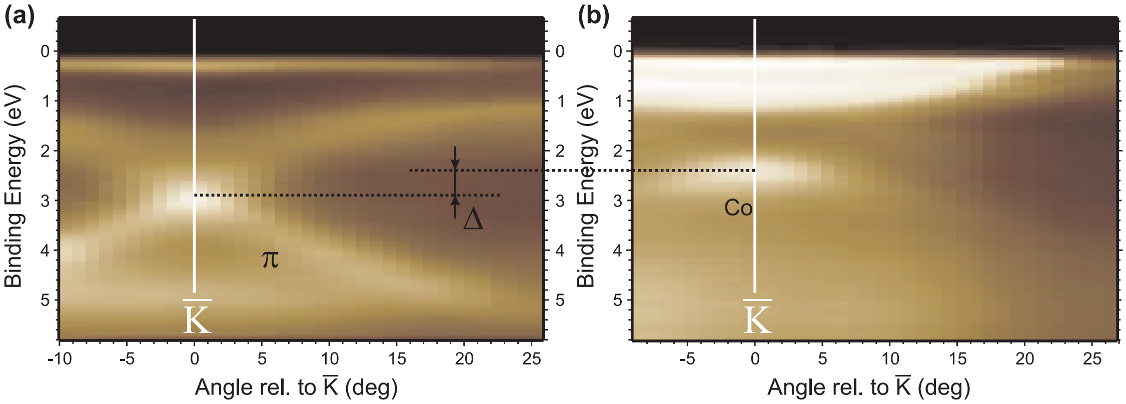

Figure 3.12: *Comparison of dispersions near the* $\overline{\mathrm{K}}$ *point for (a) graphene on cobalt and (b) bare cobalt. Energetically close to the graphene Dirac point there is a cobalt state with dispersion to higher binding energies. The energy difference between the Dirac point and the cobalt state is* $\Delta \sim 0.4$ *eV.*

fitting procedure was conducted at the same time for both beam polarizations, the peak positions and widths for two polarizations were kept the same but peak intensities were allowed to change. In Figure 3.11 the fit result is shown by solid red and blue lines. The fit could allow to discuss spin polarizations of all the bands participating in the fit independently, but due to several possible fit solutions we refrain from doing this here and leave it to further study. The main result of the fitting attempts is that possible solutions have additional cobalt components near the Dirac point. From a theoretical point of view in literature there is information confirming this conclusion [89]. It must be determined how the cobalt components contribute to the spin polarization of the π peak in the spectrum

To experimentally prove additional cobalt states in region of the graphene Dirac point, studies of the Co(0001) without graphene were done exactly in the same geometry as for the graphene/Co(0001). Results of the angle-resolved photoemission measurements are shown in Figure 3.12. In panel (a) the case of graphene on cobalt is shown and at the panel (b) the case of cobalt without graphene. Around ~ 2.4 eV binding energy there is a cobalt state with dispersion to higher binding energies. Comparing to Ref. [89] one can conclude that there are contributions of both a minority spin *sp* band and non-dispersing a minority spin *d* band. The peak position at the $\overline{\mathrm{K}}$ point is shifted compared to the Dirac point by $\Delta \sim 0.4$ eV. There are also much more intense cobalt states close to Fermi level as compared to the graphene/Co case. Note that when the cobalt surface is covered by the graphene layer, the photoemission intensity of all the observed cobalt states drops down. Thus, a contribution of the cobalt state close to the Dirac point to the graphene/Co spectra at the $\overline{\mathrm{K}}$ point should be visible maximally as a small shoulder.

To study the influence of the cobalt state on the spin polarization of the Dirac point in the graphene/Co system we conducted spin-resolved measurements of the Co(0001) and

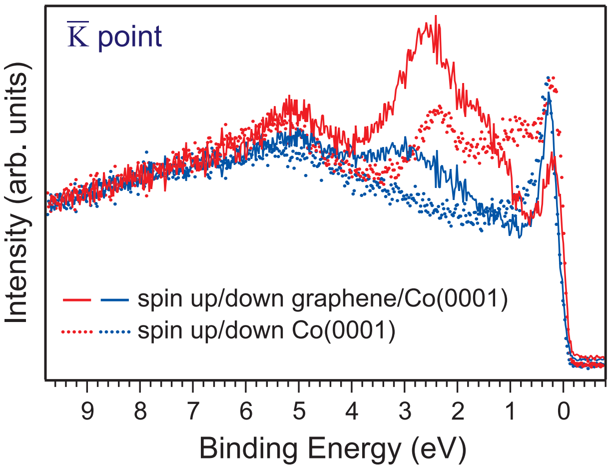

Figure 3.13: *Spin-resolved spectra at the* $\overline{\mathrm{K}}$ *point for graphene on cobalt (solid lines) and cobalt itself (dots). In this figure the spectra were normalized to the same background level.*

compared them to the graphene/Co(0001) for the same geometry. The results are presented in Figure 3.13. Solid lines represent graphene on cobalt and dots represent cobalt without graphene. To see relative intensities of peaks the background spin polarization was removed in this figure by normalization. In the spectrum of Co(0001) there is a fully spin-polarized peak at ~ 2.4 eV binding energy. 100% spin polarization of this peak could make a strong influence to the spin polarization of the Dirac point when graphene is on top of cobalt. There are two possible ways:

1. Direct hybridization with the graphene π bands which form the Dirac cone.
2. Superposition of independent photoemission intensities from this peak and the graphene Dirac cone.

Direct hybridization of this cobalt band with the graphene π band does not happen because in the angle-resolved measurements presented on Figures 3.8 and 3.12 there is no apparent hybridization gap at the corresponding place. In case of hybridization the graphene dispersion should break, like it breaks further away from $\overline{\mathrm{K}}$ when hybridizing with cobalt 3*d* states at $\sim 1-1.5$ eV binding energy. Superposition of photoelectron intensities should in any case occur. The question is for the relative impact of the cobalt state spin polarization on the spin polarization of the Dirac point. Looking on the Figure 3.13 such impact should be considered small, because:

1. The total spin up photoemission intensity at the Dirac point in the case of graphene on cobalt is larger than in the case of cobalt without graphene. This is clearly visible in figure 3.13 where the background spin polarization was removed, but it is also valid if one considers the true measured count rates.

2. After the graphene layer is put on top of cobalt, the photoelectron intensity of the peak in question becomes even smaller.

3. The first derivative in Figure 3.8(b) displays the flat Co state under the graphene while in absolute intensities of Figure 3.8(a) its contribution cannot be seen in comparison with the intence Dirac point.

So, the observed spin-polarization of the Dirac cone could not be explained fully by the cobalt peak spin polarization under the graphene layer. Nevertheless it plays a role of up to $1/3$ of the size of the observed Dirac cone spin polarization. The main part, as was discussed already, originates in the hybridization with spin polarized 3*d* cobalt states more close to the Fermi level.

The main conclusion of the presented discussion is that the ferromagnetic substrate induces a spin polarization into the peculiar graphene Dirac cone. By applying a magnetic field this spin polarization could be reversed. Such spin polarized Dirac fermions are interesting from a fundamental point of view and as additional possibility for using graphene in spintronics.

CHAPTER 4

GRAPHENE ON LOW-*Z* MATERIALS

4.1 Introduction

In graphene on silicon carbide (SiC) an anisotropic splitting of the π band of up to $\sim$200 meV was observed by spin- and angle-resolved photoemission [73]. This finding lacked a clear explanation and contradicts the expectation that in order to induce a spin splitting in graphene by the substrate, the substrate should be a high-*Z* material. Both silicon and carbon of the SiC substrate are low-*Z* atoms and have a small intraatomic potential gradient to produce a detectable spin splitting of the graphene π band. The potential gradient due to the workfunction step is also not enough to give rise to the spin splitting [22]. After submission of the present result [] the interpretation of the *arXiv* publication [73] in terms of a Rashba-type spin splitting of the graphene π band was revoked by the authors in their second preprint version leaving the question for the size of the spin-orbit splitting in graphene/SiC explicitly open [90]. Here the results for graphene on SiC and graphene on silver obtained by means of spin- and angle-resolved photoemission are presented in a more general context and with the following objections: 1) to directly check by experiment if the Rashba effect can exist in such systems, 2) to check the performance of the spin detector when applied to systems without substantial spin-orbit splitting, 3) to characterize the graphene/SiC and graphene/Ag systems for further comparison of their electronic and spin structure with other systems, like graphene on gold and iridium.

In Chapter 3.2 two examples of low-*Z* substrates under the graphene layer were already discussed: nickel and cobalt. The measurements showed no Rashba-type spin-orbit splitting in these systems in agreement with our expectations, but the presence of a ferromagnetic spin polarization of the graphene Dirac cone was discovered. Now we will continue to discuss low-*Z* substrates, the graphene/SiC system in detail and the graphene/Ag system briefly.

4.2 Graphene on SiC(0001)

4.2.1 Preparation

We discussed the cracking procedure to produce a graphene monolayer on nickel and cobalt surfaces. For graphene on SiC another method is usually used - the thermal decomposition of silicon carbide [8, 9, 77, 91]. When heated to high temperatures, a silicon carbide surface evaporates silicon atoms leaving on the surface graphene layers. By controlling temperature and heating time it is possible to grow monolayer graphene as well as multilayer graphene and graphite. There are several SiC crystal polytypes and the main ones are $3C(\beta)$ cubic silicon carbide, $4H$ and $6H(\alpha)$ hexagonal silicon carbides. The hexagonal $6H$-SiC(0001) surface can be of two types: Si-terminated SiC(0001) and C-terminated SiC(000$\bar{1}$) [91]. On the Si-terminated surface graphene grows of high quality and in registry with the substrate, but on the C-terminated silicon carbide the graphene-surface interaction is smaller and graphene grows in rotated domains which lowers uniformity of the graphene layer. In our study we prepared and characterized graphene on both cubic and hexagonal SiC, but in the present thesis only the graphene on Si-terminated $6H$-SiC(0001) will be discussed.

At first, the substrate was by our collaborators at Erlangen University etched in molecular hydrogen at a pressure of 1 bar and a temperature of 1550°C to remove polishing damage. A surface covered by a silicate adlayer [92] forms. Then by annealing of the sample at a temperature of 1650°C in 1 bar of argon a sequence of low-energy electron diffraction image occurs showing the following transformations [8]: $(\sqrt{3}\times\sqrt{3})R30^\circ$, $(6\sqrt{6}\times 6\sqrt{6})R30^\circ$ then (1×1) one monolayer graphene structure together with $(6\sqrt{6}\times 6\sqrt{6})R30^\circ$ reconstruction and finally the (1×1) graphite structure. Figure 4.1 shows the typical LEED image for the case of close to monolayer coverage. The structure $(6\sqrt{6}\times 6\sqrt{6})R30^\circ$ is also called *zero layer* or *buffer layer* graphene, it is often used as a starting point of experiments when a pure graphene monolayer or multilayer is grown or graphene is intercalated by other atoms like gold [93] is formed. Graphene monolayer grows on top of this zero layer phase and its interaction with the substrate is rather small because the zero layer serves as passivation layer for the SiC substrate and decouples the graphene monolayer from it [94]. For the present samples the thermal decomposition procedure was stopped when ~ 1 graphene layer was formed. The coverage was confirmed by x-ray photoelectron spectroscopy (XPS). Several samples were then transferred in air from Erlangen to the spin- and angle-resolved photoemission setup and cleaned *in situ* by annealing to temperatures below 1000°C.

4.2.2 Electronic structure

The formation of the electronic structure of the graphene/SiC(0001) measured by angle-resolved photoelectron spectroscopy in $\overline{\Gamma\mathrm{K}}$ and $\overline{\Gamma\mathrm{M}}$ directions is presented in Figure 4.2 taken from Ref. [94]. Panel (a) shows the zero layer graphene and panel (b) for 1 monolayer graphene on top of the zero layer. The most striking difference between their electronic structures is that the zero layer graphene system is nonmetallic and there is no π band, as characteristic of graphene. The σ states are clearly visible and this means that the atomic structure of this layer is very similar to that of the graphene monolayer, but the π band is destroyed due to strong interaction with the substrate. When the graphene monolayer is formed on top of the zero layer, the intact and intense π band is clearly visi-

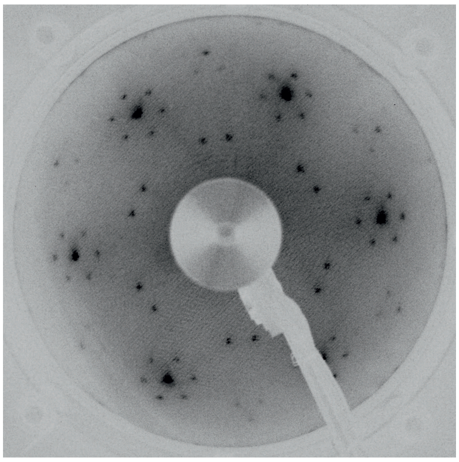

Figure 4.1: *Low-energy electron diffraction (LEED) image of close to monolayer coverage of graphene on SiC(0001).*

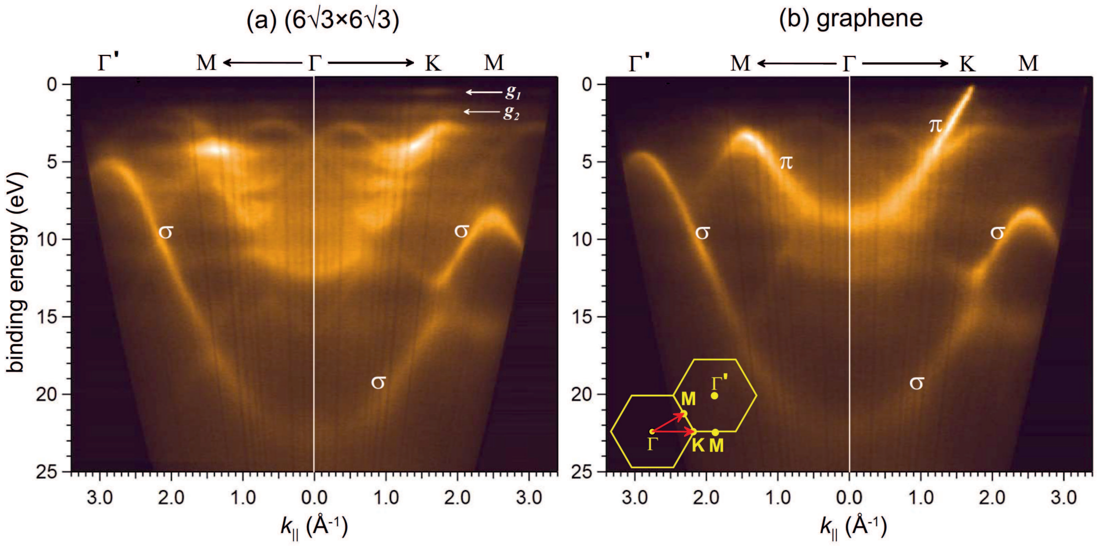

Figure 4.2: *The band structure in* $\overline{\Gamma\mathrm{K}}$ *and* $\overline{\Gamma\mathrm{M}}$ *directions of (a) zero layer graphene and (b) 1 monolayer graphene/SiC(0001) measured by means of angle-resolved photoemission. Photon energy* $h\nu = 50$ *eV. This figure is taken from Ref. [94].*

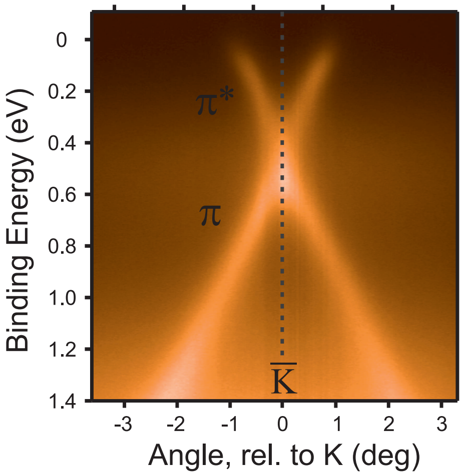

Figure 4.3: *Graphene/SiC(0001) Dirac cone. Measurements done by angle-resolved photoemission near the* $\overline{\mathrm{K}}$ *point of the graphene Brillouin zone in the direction normal to* $\overline{\Gamma\mathrm{K}}$ *at* $h\nu = 62$ *eV.*

ble (Figure 4.2(b)). It approaches the Fermi level at the $\overline{\mathrm{K}}$ point of the graphene Brillouin zone as expected for the graphene layer.

Due to the destructive interference of photoelectrons from the two graphene sublattices [84] the $\overline{\Gamma\mathrm{K}}$ direction is not ideal for seeing the graphene Dirac cone in details. To do this, measurements near the $\overline{\mathrm{K}}$ point in the direction normal to $\overline{\Gamma\mathrm{K}}$ were done and the result is shown in Figure 4.3. The *n*-doped [8, 95] intact Dirac cone dispersion characteristic of massless Dirac fermions is clearly visible with the Dirac point $\sim$ 420 meV below the Fermi level. From the photoemission, no gap is visible at the Dirac point but it should be mentioned that in the literature there was a long discussion on this topic [91, 93, 96].

4.2.3 Absence of Rashba effect

The determination of the spin-orbit splitting by spin-resolved photoemission is principally possible with very high accuracy due to the fact that the photoemission spectra are counted by separate counters. In particular, the measurable splitting is not limited by the energy resolution but by the acquired statistics and systematic errors. Because not only a giant spin splitting but also a strong anisotropy of it was predicted varying between >200 meV and zero splitting [73], we sample a substantial number of **k**-points in different directions around the $\overline{\mathrm{K}}$ point. Because spin-resolved measurements are time consuming, we limited the acquisition time for each measurement to allow for statistical and systematic errors below 10 meV. Two samples of monolayer graphene on SiC(0001) were studied by spin- and angle-resolved photoemission at a photon energy of $h\nu = 55$ eV, we will call them sample A and sample B. The overall energy (of electrons and photons) and angular

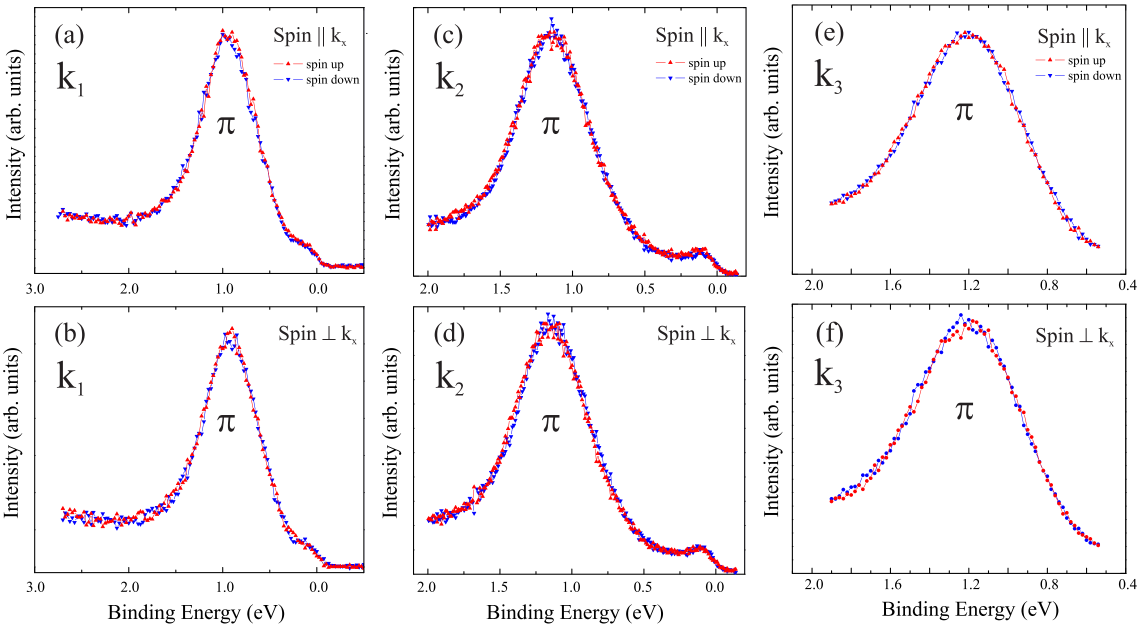

Figure 4.4: *Spin- and angle-resolved photoemission from three different points in the graphene Brillouin zone for two perpendicular spin quantization axes. (a,b) Sample A, point* $\mathbf{k}_1$ *on the* $\overline{\Gamma \mathrm{K}}$ *line. (c,d) Sample B at point* $\mathbf{k}_2$ *where the maximum splitting was predicted in Ref. [73]. (e,f) Sample B at point* $\mathbf{k}_3$ *where 200 meV splitting was reported in Ref. [73]. No splitting of the graphene π peak is seen.*

resolution of the experiments were 80 meV and 1°. The base pressure was $2 \cdot 10^{-10}$ mbar, and experiments were done at room temperature.

Figures 4.4(a,c,e) and (b,d,f) display data for the two perpendicular spin quantization axes in the graphene plane which the present measurement probes, parallel to the $\overline{\Gamma \mathrm{K}}$ direction ($\mathbf{k}_x$) and normal to it. Panels (a,b) show data from sample A at the point $\mathbf{k}_1$ of the graphene Brillouin zone ($\mathbf{k}_1$ position is shown in Fig. 4.5). Panels (c,d) show data from sample B at point $\mathbf{k}_2$, where the maximum splitting was predicted [73] but which has not been probed before in experiment [73]. Panels (e,f) show a measurement from the sample B at point $\mathbf{k}_3$ where 200 meV splitting was reported at first. Only the π peak is measured here but with improved statistics. No splitting is seen. Figure 4.5 shows as crosses all the points in the graphene Brillouin zone around the $\overline{\mathrm{K}}$ point where our spin-resolved measurements were conducted. The thick black line is a calculated constant energy surface ~ 0.8 eV below the Dirac point. The spectra have been analyzed by the procedures which will be explained in the text below and no splitting was observed with the confidence limit being of the order of 10 meV.

Each individual measurement, i.e., each $\mathbf{k}$-point, gives four spin-resolved spectra $I_x^{\uparrow}(E)$, $I_x^{\downarrow}(E)$, $I_y^{\uparrow}(E)$, and $I_y^{\downarrow}(E)$, where E is the binding energy. For each measurement, the spin-orbit splittings of the π-band $\Delta_{SO,x}$ and $\Delta_{SO,y}$ for spin quantization along x ($\parallel \overline{\Gamma K}$) and y

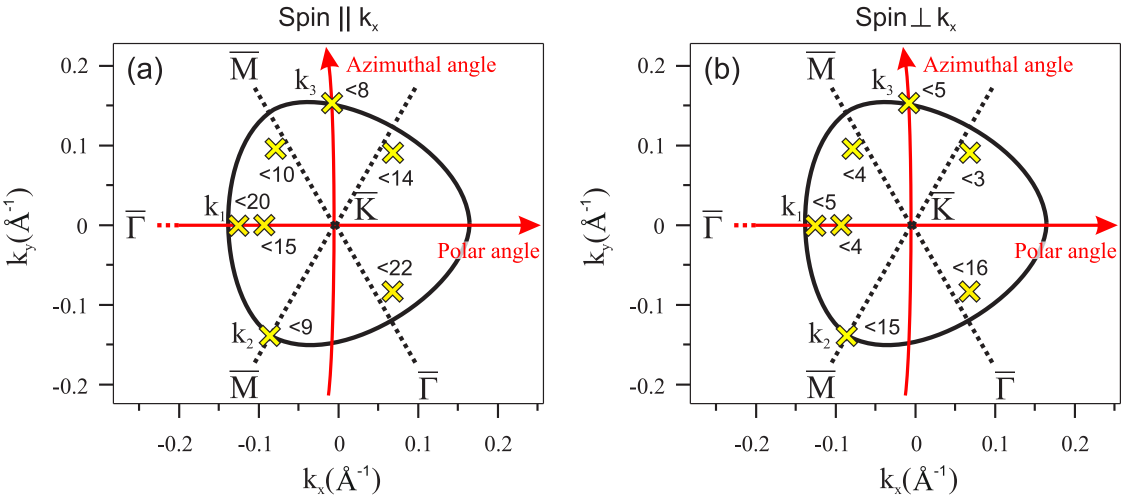

Figure 4.5: *Region near the* $\overline{\mathrm{K}}$ *point of the graphene Brillouin zone with a black thick line showing a calculated constant energy surface (at* ~ 0.8 *eV below the Dirac point). Crosses denote points where the spin-resolved measurements were done. The upper limit of the spin splitting of each measurement (*δ_{UL} *in meV) is given at each measured* ***k*** *point separately for spin quantization axes (a) along x (*$\parallel \overline{\Gamma K}$*) and (b) along y (*$\perp \overline{\Gamma K}$*).*

($\perp \overline{\Gamma K}$), respectively, have been determined as follows: As the lineshape in angle-resolved photoemission is not defined as straightforwardly as, e. g., in core-level photoemission, we decided not to fit the π-peak shape but to calculate the centroid (geometric center) of the π-peak for each spin independently after subtraction of the background $B(E)$, i. e.:

$$E^{\uparrow}_{cent,x} = \frac{\sum [E \cdot (I^{\uparrow}_x(E) - B(E))]}{\sum [I^{\uparrow}_x(E) - B(E)]} \tag{4.1}$$

where the sum is over all data points in the peak. The resulting splittings are then:

$$\Delta_{SO,x} = E^{\uparrow}_{cent,x} - E^{\downarrow}_{cent,x} \tag{4.2}$$

$$\Delta_{SO,y} = E^{\uparrow}_{cent,y} - E^{\downarrow}_{cent,y} \tag{4.3}$$

An alternative approach for determining the splitting has been used as well, it is shown schematically in Figure 4.6. In this case the splitting $\Delta_{SO,x}$ (analogous for y) is an average over spin splittings Δ_i for every data point on the sides of the peak, $\Delta_i = E^{\uparrow}_i - E^{\downarrow}_i$. $E^{\uparrow}_i$ and $E^{\downarrow}_i$ are determined from the condition $I^{\uparrow}_i(E^{\uparrow}_i) = I^{\downarrow}_i(E^{\downarrow}_i)$ by linear interpolation in order to assure a one-to-one correspondence between data points in the spin-up and spin-down spectra. Both approaches gave the same results for Δ_{SO} for all **k**-points. The statistical error σ_x has then been calculated as the standard deviation of the mean value $\Delta_{SO,x}$.

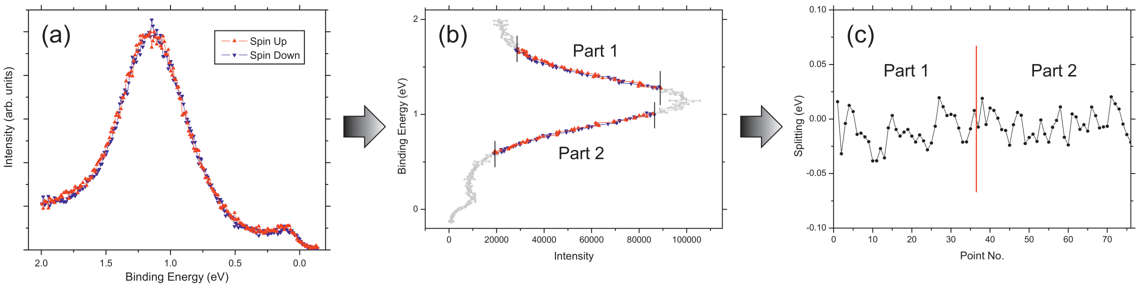

Figure 4.6: *One out of several ways to determine the spin splitting of the graphene π peak.*

We found that σ_x and σ_y become so small that they are smaller than the systematic errors of the experiment. The systematic error of the spin-resolved photoemission spectrum results mainly from the sample alignment for an individual measurement, and it changes for each new **k**-point since each new **k**-point requires a new sample alignment. One possible way to control this systematic error is to reverse the spin splitting by subsequently comparing **+k** with **-k** as we will do for the Rashba-type spin-orbit splitting in of graphene/Au in chapter 5. This is not possible in the present experiment because we do not observe a Rashba splitting. In each measurement we sampled a different **k**-point, therefore we cannot reduce the systematic error $\delta\Delta_{SO}$ below the measured value for the spin splitting, i. e., $\delta\Delta_{SO} = |\Delta_{SO}|$. Therefore, the upper limit of the spin splitting at each **k**-point is $\delta_{UL,x} = |\Delta_{SO,x}| + \sigma_x$.

We took particular care to sample both supposed [73] areas of large and small splitting. Our seven probed **k**-points are marked in the Figure 4.5 by yellow crosses. The upper limits of the spin splittings are shown there near the crosses separately for the two spin quantization directions in the graphene plane x [$\parallel \overline{\Gamma K}$, Fig. 4.5(a)] and y [$\perp \overline{\Gamma K}$, Fig. 4.5(b)] which the present experiment probes. The upper limits are in each case $\sim$ 20 meV or less.

The anisotropy of the Rashba splitting was in Ref. [73] supported by theory. To reestimate the size and anisotropy of Rashba-type spin-orbit splitting for graphene on SiC in view of our experimental results density functional theory calculations in the generalized gradient approximation using the full-potential linearized augmented planewave method were performed for us by G. Bihlmayer at Jülich. He assumed a geometry matching a $p(2\times 2)$ graphene unit cell to a $(\sqrt{3}\times\sqrt{3})R30^\circ$ unit cell of 6H-SiC(0001), similarly to the model employed in Ref. [97] with two carbon layers on the SiC. The substrate was modeled by a film of six bilayers of SiC where the dangling bonds of the lower surface were saturated with H. This avoids coupling effects through the film. The structural parameters were taken from Ref. [97]. Although the structural model can be refined [98], it is reasonable to assume that the present model captures the spin-orbit effects in this system quite well.

Three different SiC terminations, a Si- and a C-terminated one, as well as a C-terminated

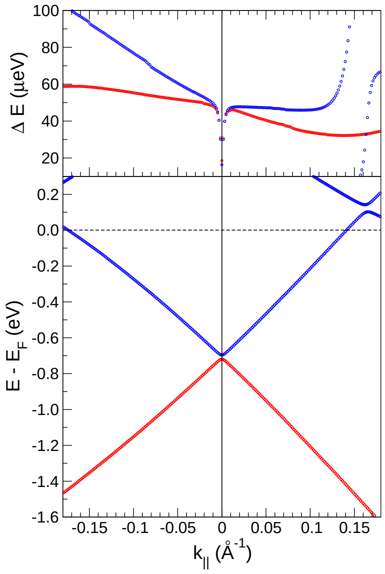

Figure 4.7: *Lower panel: Dirac cone of graphene on a C-terminated SiC substrate with a C-deficient interface layer.* $k_{\|} = 0$ *indicates the* $\overline{\mathrm{K}}$ *-point, negative* $k_{\|}$ *values signify the direction towards* $\overline{\Gamma}$ *, positive* $k_{\|}$ *values towards* $\overline{\mathrm{M}}$ *. Upper panel: Spin-orbit splitting of the upper (blue) and lower (red) branch of the Dirac-cone formed by the* p_z *band. At the* $\overline{\mathrm{K}}$ *point, the splitting reduces to about* $20\mu eV$*, at a band-crossing at around* $0.15\AA^{-1}$ *it can reach more than 0.1 meV. Calculations courtesy of G. Bihlmayer (Jülich).*

substrate with a C-deficient interface layer were compared in these calculations. In all three cases the Rashba-type spin-orbit splitting of the valence-band part of the p_z bands at the $\overline{\mathrm{K}}$ point was far below the resolution limits of our experiment. Slight variations come from the different surface terminations, ranging from 0.02 meV for the Si- and C-terminated surface to 0.05 meV for the C-deficient one. According to the model of spin-orbit splitting in graphene [66, 70, 99] this value is the Rashba contribution, i.e. the part that is induced by the substrate. In addition, these calculations also give the intrinsic spin-orbit splitting for the graphene, which are of the same order of magnitude, 25 μeV, in good agreement with previous calculations [66, 99]. In addition, a dangling bond is observed above the Fermi level which cannot be accessed by photoemission. Where this flat band crosses the Dirac cone, locally an enhancement of the spin-orbit splitting by a factor 5 - 10 occurs. Finally, the anisotropy of the splitting was investigated, i.e., the fact that the spin-orbit splitting of the occupied branches develops differently along $\overline{\mathrm{K}\Gamma}$ and $\overline{\mathrm{KM}}$.

The spin-orbit splitting is found to vary up to 50%: Figure 4.7 shows the Dirac-cone on a C-terminated SiC substrate with a C-deficient interface layer. Indeed, the branches show a different evolution of the spin-orbit splitting in the direction $\overline{\mathrm{K}\Gamma}$ (negative $k_{\|}$ values)

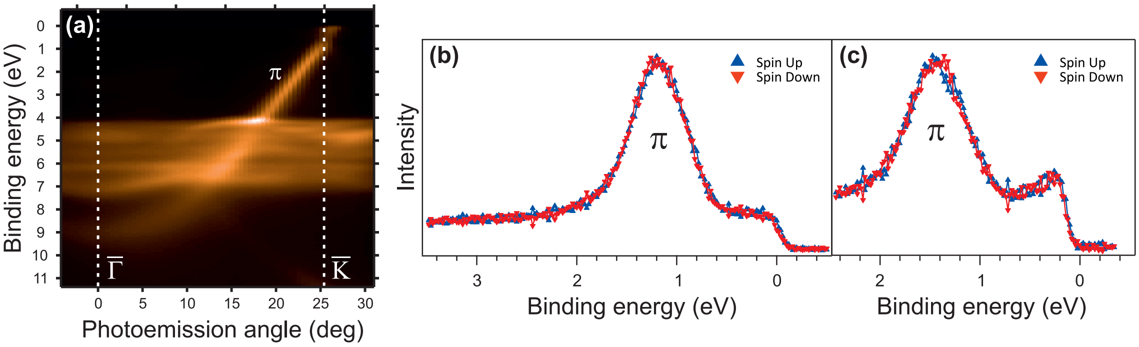

Figure 4.8: *(a) Band structure of graphene/Ag in the* $\overline{\Gamma K}$ *direction. In the region of 4-7 eV binding energy the flat dispersion of Ag 4d states is seen. (b,c) Spin- and angle-resolved photoelectron spectra showing the absence of a detectable spin-orbit splitting of the graphene π band.*

and $\overline{KM}$ (positive $k_{||}$ values) that is, moreover, dependent on the branch of the π band. The upward dispersing branch π^* shows a rather constant splitting of $50-60\mu$eV until it crosses another band at 0.15$Å^{-1}$, where the splitting gets significantly enhanced. The downward dispersing branch π starts at $-0.17Å^{-1}$ with a large spin-orbit splitting of 100μeV, which drops to 35μeV in the direction $\overline{KM}$.

We discussed above that there is no sizable Rashba effect in the experiments of graphene/Ni(111) and graphene/Co(0001). The present results for graphene/SiC(0001) are also in agreement with our conclusion that a sizable Rashba splitting in graphene requires the proximity to a heavy element such as Au [7]. We will discuss this in chapter 5 using a Ni substrate and Au intercalation. As a outlook, it has actually been demonstrated that the system graphene/SiC(0001) can be intercalated with a Au monolayer [93, 100]. This would be a promising semiconductor system for achieving a Rashba-type spin-orbit splitting at the Fermi level in graphene.

4.3 Graphene on Silver

Graphene on silver was prepared by the *intercalation* procedure where a silver (or gold, copper etc.) layer is put on top of graphene/Ni(111) and the system is annealed for ∼5 min at a temperature around 600 K. During annealing the deposited metal goes under the graphene layer and decouples graphene from the substrate. This procedure will be discussed in detail in Section 5.1.1 for Au layer. The intercalation procedure of gold is schematically shown in Figure 5.1, for the case of silver the procedure is the same.

The electronic structure of graphene/Ag is shown in Figure 4.8(a). It is rather similar to the free graphene electronic structure, but there are also several substantial differences:

1. The full graphene π band is shifted to higher binding energy by ~ 1 eV in average and reaches 9 eV binding energy in the $\overline{\Gamma}$ point.
2. This corresponds to n-doping and the Dirac point is at ~ 0.6 eV binding energy.
3. We observe a gap at the $\overline{\mathrm{K}}$ point of the graphene Brillouin zone, i.e., at the Dirac point.

The graphene π band crosses silver bulk states in the 4–7 eV binding energy region without apparent hybridization between them. However, the intence flat *d* band at 4 eV could indicate a hybridization with the graphene π band. Due to destructive interference of photoelectrons from two graphene sublattices [84] in the $\overline{\Gamma\mathrm{K}}$ direction only parts of the graphene π and π^* bands are visible around the $\overline{\mathrm{K}}$ point: In the first Brillouin zone only the π band is visible, in the second Brillouin zone only the π^* band is visible as a small intensity spot close to the Fermi level.

Spin-resolved measurements are presented in Figures 4.8(a,b). They were measured at $h\nu = 62$ eV photon energy at several k points close to the $\overline{\mathrm{K}}$ point. Similarly to the graphene/SiC case which we discussed in Section 4.2, there is no detectable spin-orbit splitting of the graphene π band. This result is fully expectable since Ag is low-Z material. The absence of a sizable spin splitting in graphene on low-Z materials is also a perfect test for the functional calibration of the spin detector, the correctness of which is a precondition for the proper characterization of spin effects in graphene on high spin-orbit materials.

CHAPTER 5

GRAPHENE ON HIGH-Z MATERIALS

5.1 Graphene on gold

As it was mentioned before in the Thesis the intrinsic spin-orbit coupling in graphene is very weak. The splittings are of the order of 0.02 meV as concluded in section 4.2 an agreement with previous calculations [66, 99]. For spintronics such weak spin-orbit coupling is good because it leads to a long spin coherence length of the size of ∼1.5–2 μm [32–34]. We also mentioned in the introduction that an externally induced large spin-orbit coupling in graphene could open the way for graphene as the channel material in the Datta-Das spin field-effect transistor [30]. The element gold is often used to demonstrate large spin-orbit coupling effects [21, 101]. There are spin-split surface states at the $\overline{\Gamma}$ point in the region of the Fermi level [21]. We have discussed these surface state as an example of the Rashba-type spin-orbit splitting in section 2.2.1 [21, 102, 103]. The band dispersion of graphene with broken up-down symmetry required for the Rashba effect was calculated in Ref. [70] and was discussed in section 2.2.2, see Figure 2.5. In zero magnetic field, the band topology was predicted to be similar to that of the unbiased spinless bilayer graphene but with an additional spin texture which is tangential to the circular constant-energy surfaces.

Previously we studied the graphene/Au/Ni(111) system by spin- and angle-resolved photoemission and published the observation of $\sim$ 13 meV spin splitting of the grapheen π band [7]. This splitting is due to the influence of the Au and is three orders of magnitude larger than the $\sim$ 0.02 meV intrinsic spin-orbit splitting in graphene. In the current chapter we will show that the spin splitting can be further enhanced by an order of magnitude. We will discuss the spin- and angle-resolved photoelectron spectroscopy characterization of the graphene/Au/Ni(111) system and show $\sim$ 100 meV splitting. The value of splitting is nearly constant at different points of the graphene Dirac cone and reverses with reversal of the wave vector in full agreement with the calculated Rashba effect for graphene. Because this splitting is so large compared to the case of the free graphene layer, we call it a *Giant Rashba effect*.

The graphene π band dispersion is linear as for freestanding graphene and reaches the Fermi level. The splitting extends to the Fermi level as well, i.e., the Fermi surface is spin split and spin polarized, keeping in mind that the spin polarization vanishes when integrated over k. We will show that a spin-dependent hybridization of the graphene π

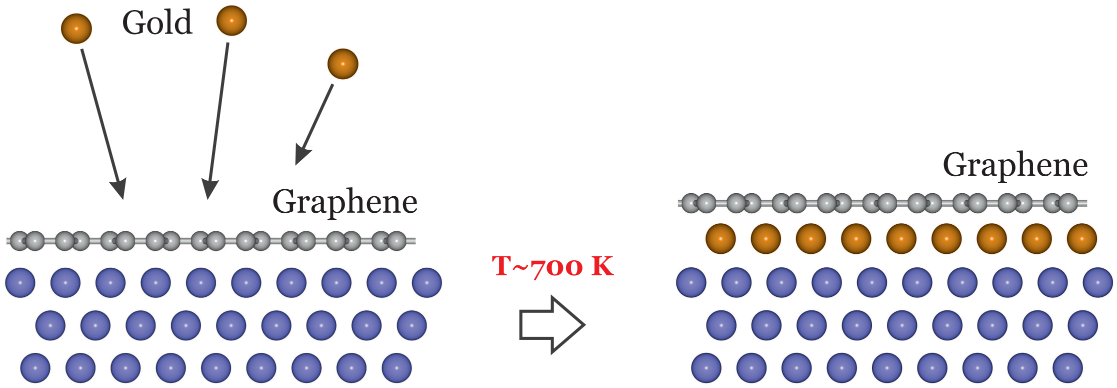

Figure 5.1: *Schematic view of intercalation of gold between graphene and nickel. About 1-1.5 monolayer of gold is deposited on top of graphene and subsequently annealed.*

band with gold 5*d* states is a source of the observed giant Rashba effect in the graphene. The observation of different superstructures of gold under the graphene layer as well as the results from *ab initio* calculations will be discussed. Based on the *ab initio* calculations, the giant spin-orbit splitting is attributed to dilute Au atoms that are very close to the carbon atoms, i. e., closer than the Au atoms in an ideal Au monolayer in contact with the graphene.

5.1.1 Preparation and electronic structure

To prepare graphene/Au/Ni(111) we used the procedure of propylene (C_3H_6) *cracking* to make a graphene/Ni(111) system first. This procedure and the sample characterization were discussed in section 3.2 and schematically shown in Figure 3.1. The result of the cracking is a large-scale high-quality graphene layer on nickel. After that, a gold layer is inserted under the graphene layer by the intercalation procedure. The mass equivalend of about 1-1.5 monolayer of gold is deposited on top of the graphene/Ni at room temperature and the system is subsequently annealed at about 700 K for $\sim$5 min. The intercalation procedure is schematically shown in Figure 5.1. It is important to note that the intercalation of Au is self-limited at a concentration of about 1-1.2 ML. If more Au is deposited, STM and ARPES show that exceeding material remains on top of graphene and forms large 3D islands. We characterized the graphene/Au/Ni(111) system with a number of experimental techniques: LEED, STM, photoelectron spectroscopy of core levels (XPS), high resolution angle-resolved photoelectron spectroscopy (ARPES) and by spin-resolved photoelectron spectroscopy (SARPES). A part of this characterizations was published in Ref. [7]. STM and LEED from graphene on gold show a large scale uniform graphene coverage with a moiré superstructure which is caused by a small lattice mismatch between layers. In the present Thesis new data is reported. Angle-resolved photoelectron spectroscopy measurements were done in different directions in the graphene Brillouin

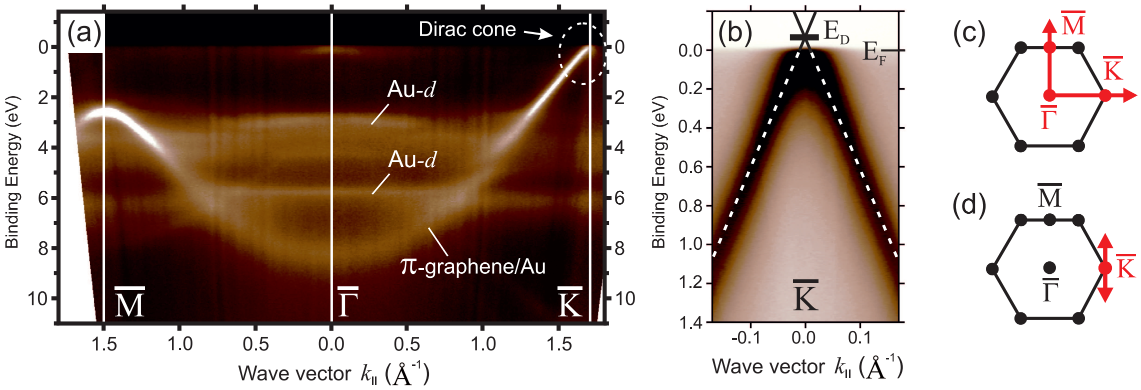

Figure 5.2: *Electronic structure of graphene/Au/Ni(111) measured by angle-resolved photoelectron spectroscopy at* $h\nu = 62$ *eV. (a) Large angle and energy range overview in the* $\overline{\Gamma\mathrm{K}}$ *and* $\overline{\Gamma\mathrm{M}}$ *directions. (b) Magnified view of the Dirac cone region measured normal to the* $\overline{\Gamma\mathrm{K}}$ *direction. (c,d) Directions of corresponding measurements. Horizontal axes in both (a) and (b) panels are in-plane wave vectors but in (a) they are measured relative to the* $\overline{\Gamma}$ *point and in (b) relative to the* $\overline{\mathrm{K}}$ *point.*

zone, at different photon energies and polarizations, different concentrations of gold, different temperatures and other preparation conditions. Figure 5.2(a) shows a large angle and energy scale overview of the band structure of graphene/Au/Ni(111) measured at a photon energy $h\nu = 62$ eV in the $\overline{\Gamma\mathrm{K}}$ and $\overline{\Gamma\mathrm{M}}$ directions. The graphene π band extends from ~ 8.2 eV binding energy at the $\overline{\Gamma}$ point to ~ 2.6 at the $\overline{\mathrm{M}}$ point and to the Fermi level at the $\overline{\mathrm{K}}$ point of the graphene Brillouin zone. It crosses gold 5d states in the 2.5-6.5 eV binding energy region. The energy at the $\overline{\Gamma}$ point compared to the graphene/Ni case is by ~ 2 eV shifted to lower binding energies. Figure 5.2(b) shows a magnified view of the region near the $\overline{\mathrm{K}}$ point measured in the direction normal to $\overline{\Gamma\mathrm{K}}$ to observe both branches of the π band at the same intensity. There, the dispersion is that of a linear Dirac cone with the Dirac point close to the Fermi level (slightly p-doped). Such dispersion is the peculiar property of a freestanding graphene layer. Both the energy position at the $\overline{\Gamma}$ point and the presence of an intact Dirac cone show that the intercalated gold layer decouples graphene from the nickel substrate and transforms the graphene band structure into a quasifreestanding one. These observations are in full agreement with previous studies of this system [6, 7, 95, 104].

5.1.2 Giant Rashba effect in graphene

Figure 5.3 shows the spin- and angle-resolved photoemission measurements of graphene/Au/Ni(111). Panel (a) shows the π band with its linear quasirelativistic dispersion, and crosses indicate where spin-resolved photoemission spectra (b–d) have been measured. The splitting between spin-up spectra $I^{\uparrow}(E)$ (upward triangles) and spin-down spectra $I^{\downarrow}(E)$ (downward

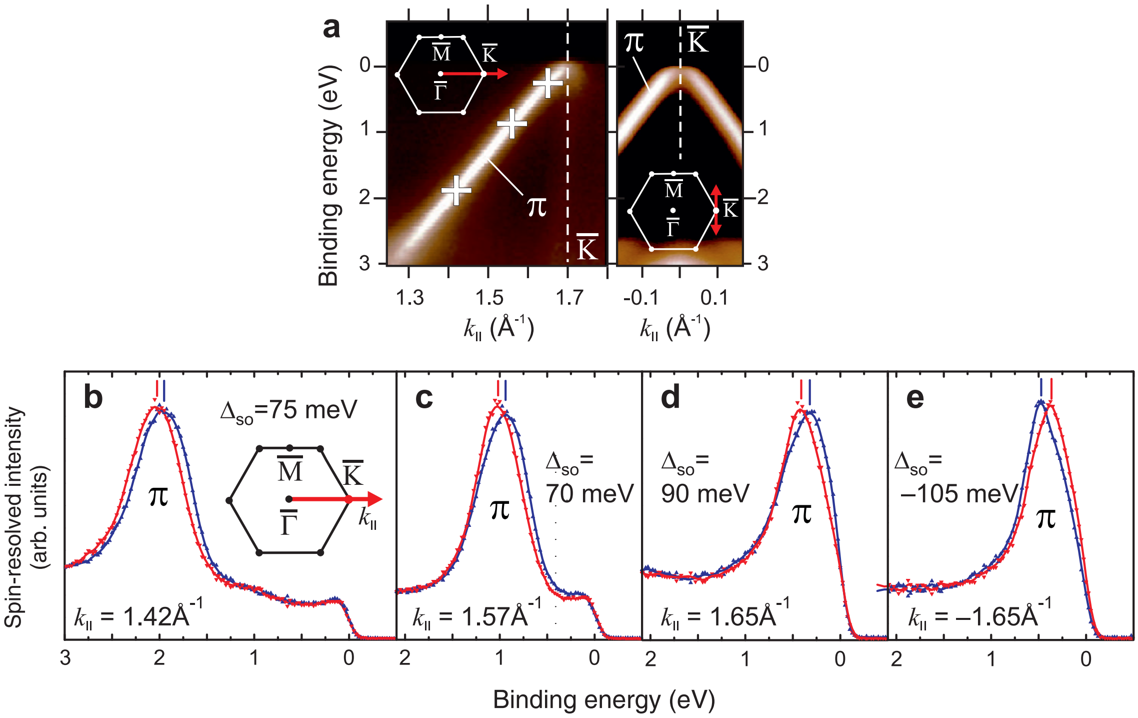

Figure 5.3: *Giant spin-orbit splitting* Δ_{so} *of the graphene* π *band. (a) Angle-resolved photoemission near the* $\overline{\mathrm{K}}$ *point of the graphene Brillouin zone of graphene/Au/Ni(111). Crosses indicate where the Dirac cone of the graphene* π*-states is probed by (b–d) spin- and angle-resolved photoemission spectra (h*ν = *62 eV). Blue and red lines in panels (b–e) are spin up and spin down spectra. (e) The spin splitting reverses with the sign of* $k_{\parallel}$*. In panels (a) and (b) the directions in the graphene Brillouin zone where corresponding measurements were done are shown as insets.*

triangles) is clearly visible and amounts near the Fermi level to 90 meV at $k_{\|} = 1.65$ Å^{-1} and -105 meV at $k_{\|} = -1.65$ Å^{-1}. Apparently, the sign of the splitting reverses with the sign of $k_{\|}$ as expected for a Rashba effect (see panels (d) and (e)). This giant spin splitting is the central experimental result of the present Thesis. Note that the splitting exceeds also the room-temperature broadening, and together with the fact that it extends to the Fermi energy, it becomes directly relevant for transport applications. In fact, transport properties of graphene with an externally induced spin-orbit splitting have been intensively investigated in recent years [39, 41, 42] and important predictions have been made: the spin Hall effect [39], the quantum spin Hall effect [40, 41] and, with an additional exchange interaction, the quantum anomalous Hall effect [42]. In brief, the spin Hall effect describes spin accumulation, the quantum spin Hall effect can be described as the quantum Hall effect with the external magnetic field replaced by the effective magnetic field of Figure 2.3 and is the two-dimensional version of a topological insulator, and the quantum anomalous Hall effect combines the spin-orbit splitting with an exchange splitting of similar size.

To establish the connection between our previous 13 meV data and the new 100 meV data, we undertook a closer inspection of the spin-resolved spectra of Figure 5.3. They reveal that the system is inhomogeneous and the high-splitting phase ($\sim$ 100 meV) and the low-splitting phase ($\sim$ 10 meV) are present simultaneously. Line fits and spectral decompositions (Figure 5.4) show that the high-splitting phase makes up between one third and two thirds of the spectral weight. Note that the photoemission experiment averages over a macroscopic sample region of about 200 μm $\times$ 200 μm so that the two phases roughly share this area. Returning to Figure 5.4, the decomposition is possible due to the energy shift between the two phases with the low-splitting phase observed at about 200–500 meV higher binding energy. The fit of the spectra was done under the most simple assumption: in addition to the spin-up and spin-down components (here at lower binding energy) we allow for a non-split component (as an approximation to the small splitting of 13 meV) (green line). Because the four displayed spectra stem from three measurements with slightly different ratios between the coexisting phases, their ratios are allowed to vary in the fit as well. The negative wave vector $k_{\|}$=-1.65 Å^{-1} shown in panel (d) can only be reached by a large change in the electron emission angle. This changed also the light polarization conditions and an additional component to roughly model the appearance of the Ni 3*d* state at the Fermi energy (yellow line) had to be introduced in this case. Finally, it should be mentioned that the giant magnitude of the splitting and the distribution of the spectral weight between the high-splitting and low-splitting phases ranging from 1 : 2 to 2 : 1 have been reproduced in experiments in several *in situ* preparations and at different beamlines.

5.1.3 Hybridization as the source of the giant splitting

We want to discuss the electronic origin of this strongly enhanced spin splitting including the reason for the two phases of low and high splitting and the relation to our previous

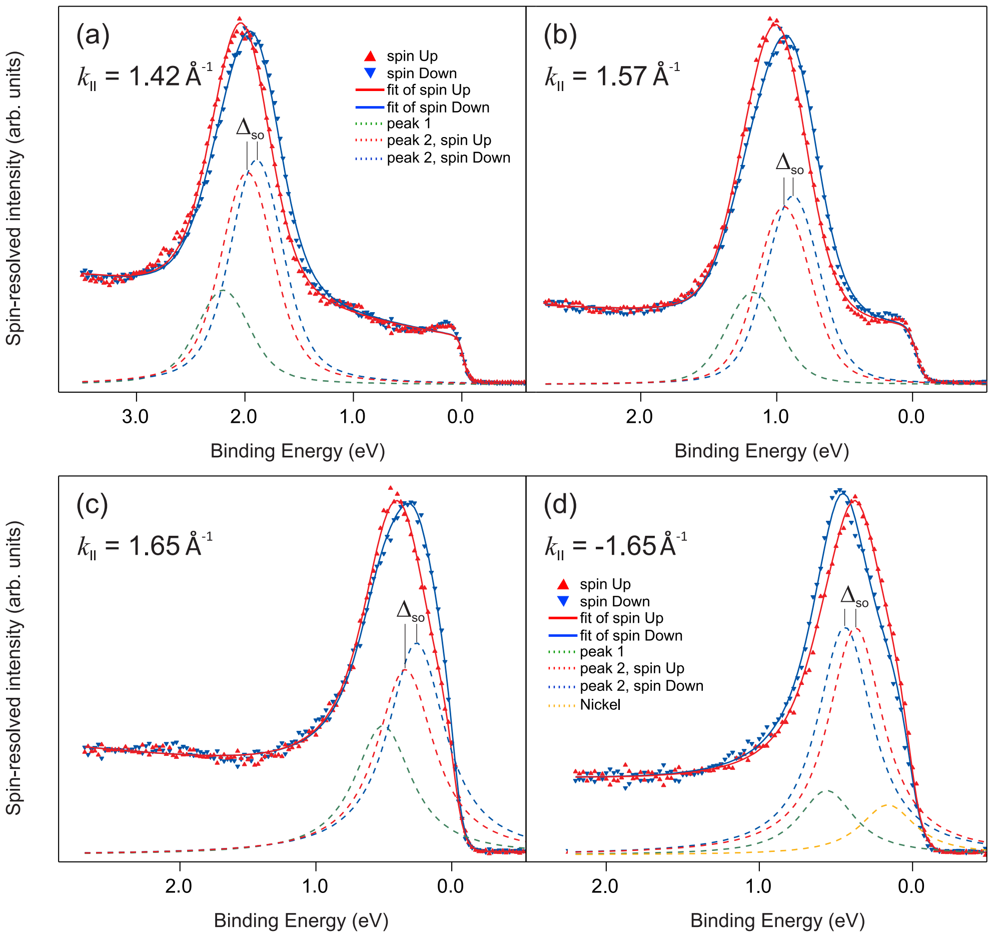

Figure 5.4: *Fit of the spin-resolved spectra from Figure 5.3 revealing contribution of the phase with low spin orbit splitting to the spin-resolved spectra. The non-split component at higher binding energy (green) models the ≈13 meV spin-orbit split band observed in our previous study [7].*

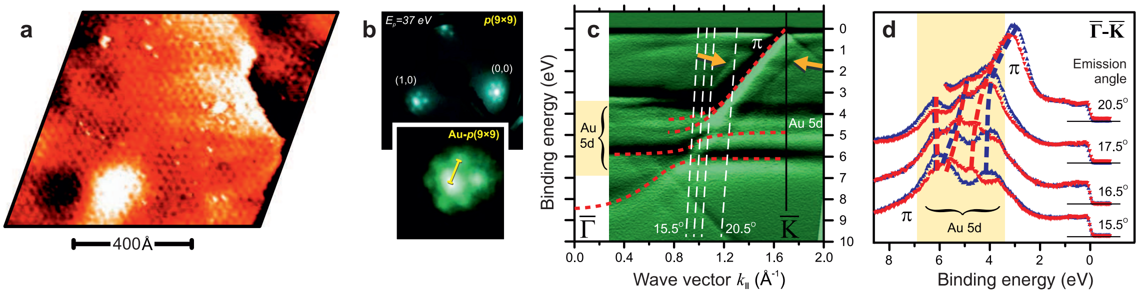

Figure 5.5: *(a) Scanning tunneling microscopy and (b) low-energy electron diffraction for 1.1 ML of gold under the graphene layer with a* 9 × 9 *moiré-type superstructure. (c) Angle-resolved photoemission (first derivative of the intensity over energy). Hybridization between the* π *band of graphene and* 5d *states of Au is emphasized by the dashed red lines. White dashed lines denote the* $k_{\parallel}$ *values for which the spin-resolved spectra displayed in (d) were measured (*$h\nu = 62$ *eV). (d) Spin-resolved measurements in the region of hybridization between the graphene and gold bands. It is seen that the spin-split* π *states develop directly out of a large spin-orbit splitting of Au* 5d *states. Blue and red triangles denote spectra for opposite spin.*

results. Direct probing as well as controlling of the Au interlayer as the likely source of the giant Rashba splitting are challenging because most of the Au atoms are located underneath the graphene layer. Basically, we can only control the nominal amount of Au deposited on top of the graphene/Ni before intercalation which typically exceeds the subsequently intercalated amount. While graphene and Ni(111) have a lattice mismatch of only 1.2%, the mismatch between the graphene and Au(111) is much larger ($\sim$ 14%). Therefore, the intercalated monolayer of Au cannot reach the same atomic density as the Ni. Probing of the resulting interfacial structure is possible by STM and by LEED as is shown in Figure 5.5(a,b) for 1.1 ML of gold under the graphene layer with a 9 × 9 moiré superstructure. The moiré effect reveals the superstructure through the periodic beatings developing because of the mismatch between the graphene lattice and the Au monolayer. Note that in Ref. [7] this structure was roughly assigned as 10 × 10.

Unfortunately, the core levels do not allow to draw any conclusions about the structure of gold under the graphene layer as the shape and the energy positions of the $4f$ states of Au do not change during the intercalation process. This is shown, as an example, for graphene on Co(0001) in Figure 5.6. The Au $4f$ spectra before and after intercalation do not show a core-level shift which could be used to identify the sites of Au atoms. While Au $4f$ does not visibly change, the C 1s spectra show a shift indicating successful intercalation.

We argue that for observing the spin-orbit splitting of the size of 100 meV in the graphene/Au system, the spin-resolved ARPES measurements are required because the ARPES spectrum without spin-resolution as presented in Figure 5.7(a) reveals only a

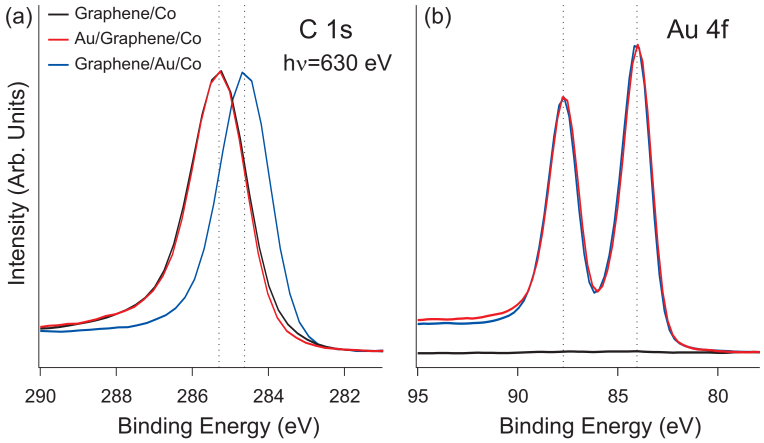

Figure 5.6: *Characterization by core-level spectra of gold intercalation under the graphene on Co(0001). After synthesis of graphene (black) the Au (≈1.5 ML) is deposited at room temperature (red) and subsequently intercalated by annealing (blue). The data shown are for Co(0001) instead of Ni(111) but are otherwise comparable. The spectra have been normalized to equal maximum intensity.*

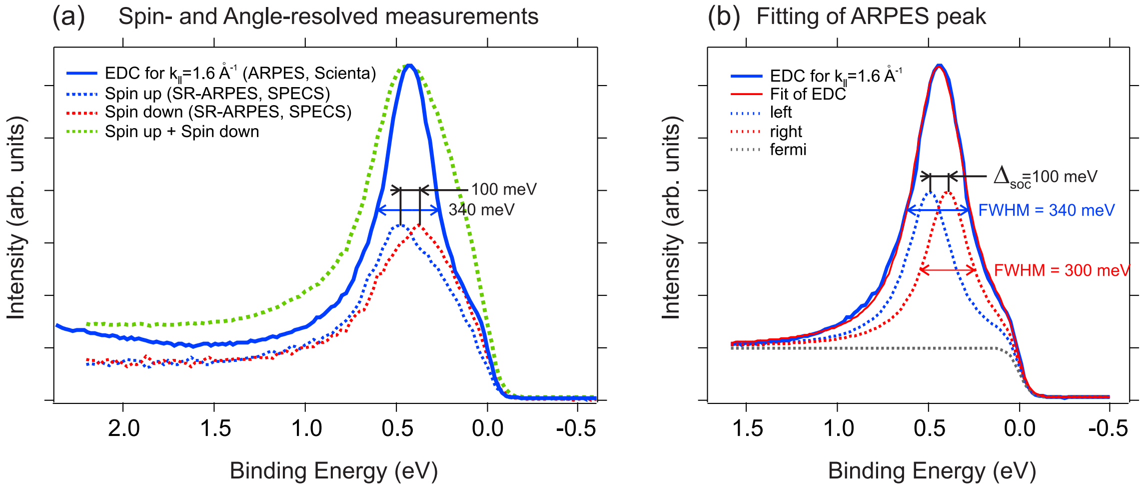

Figure 5.7: *Consistency of spin-resolved and non-spin-resolved ARPES measurements. (a) Dashed blue and red lines denote spin-up and spin-down spectra from spin-resolved ARPES setup. The green dashed line is a sum of experimental spin up and spin down spectra. The thick blue line shows experimental data from the high-resolution ARPES setup. (b) Blue and red dashed lines to model the* 100 *meV spin splitting with* 300 *meV FWHM peaks. The thick red line shows a sum of blue and red dashed lines. The thick blue line shows the same high-resolution experimental data as in panel (a).*

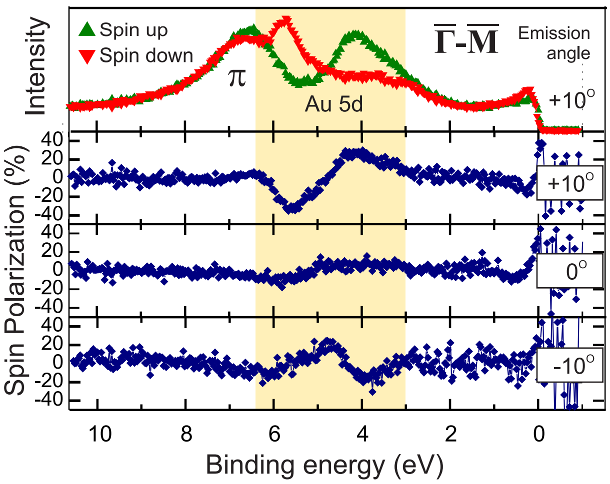

Figure 5.8: *Comparison of* $+k_{\|} = 0.6$ *Å*$^{-1}$ *(*$+10^\circ$*) and* $-k_{\|}$ *data (*-10°*) for graphene/Au/Ni(111). The behavior of the spin polarization [*$p = (I_\uparrow - I_\downarrow)/(I_\uparrow + I_\downarrow)$*] shows an almost vanishing spin polarization at* $k_{\|} = 0$*, as expected for a Rashba effect, and a rather clear reversal for* $-k_{\|}$ *if we take into account that the spin polarization of Au 5d states is also subject to spectroscopic effects such as the linear dichroism of Au 5d emission [105] which do not reverse with the sign of* $k_{\|}$*. This means that the Rashba-type spin-orbit splitting of the graphene* π *states is accompanied by a Rashba effect on the Au monolayer itself. Such effect has similarly been observed for Au/W(110) [26,46].*

sharp peak without any apparent splitting. The summation of the spin-up and the spin-down spectra gives a broad peak (dashed green line) in panel (a). On the other hand, the ARPES data [solid blue line in (a)] is sharper due to higher angle resolution of the angle-resolved photoemission setup. Therefore, in (b) we have simulated the summation of two peaks split by 100 meV for the case of better angular resolution in the angle-resolved experiment. It is seen that also in this case no splitting of spin-integrated peak appears and it is not possible to distinguish a spin splitting at such broadening and splitting sizes without direct spin resolution.

Figures 5.3(a) and 5.5(c) show that the graphene electronic structure resembles that of the freestanding graphene. The Au layer prevents any considerable carbon-Ni hybridization which would modify the dispersion of the π band near the Fermi energy as discussed in section 4.3. Nevertheless, also in the quasifreestanding phase with intact Dirac cone (Figure 5.5(c)) several hybridization points between the π states of graphene and 5*d* states of Au are revealed at the binding energies between 4 and 6.5 eV. This is also much clearer than for the Ag intercalation in Fig. 4.8. In addition, replicas of the graphene π band shifted to smaller and larger values of the wave vector $k_{\|}$ are observed (orange arrows in Figure 5.5(c)). Their shift in $k_{\|}$ amounts to between 1/7 and 1/9 of the $\overline{\Gamma \mathrm{K}}$ distance. The STM image in Figure 5.5(a) shows a moiré pattern of a similar periodicity. The observed superstructure can be identified by the LEED more accurately than by STM as a 9×9 (Figure 5.5(b)). This is in good agreement with the periodicity of the band replicas in the photoemission spectra. Dashed lines in Figure 5.5(c) show where we probed the hybridization points by the spin-resolved spectra (Figure 5.5(d)). These spectra reveal that the giant $\sim$ 100 meV spin splitting of the π band smoothly merges into an even larger spin splitting ($\sim$ 0.6 eV) of the Au 5*d* states. This provides a strong indication that the spin-dependent hybridization of the carbon π states with the *d* states of the heavy Au is the origin of the giant Rashba splitting in graphene. For probing if the spin splitting of the Au is also of Rashba type, spin-resolved measurements for two opposite directions of the in-plane wave vector were performed, and the results are shown in the Figure 5.8. It is seen that most features of the spin polarization show a reversal.

Interestingly, when a larger nominal amount of Au is deposited on top of graphene prior to intercalation, it forms after intercalation a slightly different 8×8 superstructure. Figures 5.9 and 5.10 show the characterization by STM, LEED and ARPES of the graphene/Au/Ni(111) system after intercalation of different amountsof Au in which the transition from the 9×9 to the 8×8 superstructure manifests itself. In Figure 5.9(a) graphene on bare Ni(111) shows a pronounced 3-fold symmetry in STM and (e) a clear $p(1 \times 1)$ pattern in LEED which means that graphene is perfectly in registry to the Ni substrate. In panel (b) graphene on Ni(111) intercalated with various submonolayer amounts of Au is shown. Underneath of the graphene, the Au forms islands of various dimensions and shapes. STM scans of these islands exhibit the $p(9 \times 9)$ moiré superstucture. This superstructure is attributed to the lattice mismatch between Au and Ni. The interatomic distances are in bulk Au 2.88 Å and in bulk Ni 2.48 Å. Since the lattices of graphene and Ni(111) match exactly, it is not surprising that 1 ML Au/Ni(111) also forms a $p(9 \times 9)$ structure at room temperature [106, 107]. We find that underneath the graphene, this structure is rather stable independently of the exact amount of intercalated Au. These $p(9 \times 9)$ islands always co-exist with areas which resemble cluster superlattices (marked with green arrows). Those areas can be attributed to the formation of an interfacial alloy between Ni and Au under the graphene. Such surface alloy has been observed for Au/Ni(111) after annealing [108]. However, these clusters cover only a minor part of the sample surface and were not found relevant to our results. The fact that we do not observe large areas of alloyed Au under the graphene is understandable: It was shown and demonstrated for carbon monoxide that the presence of another species reverses the process again (de-alloying) [108] so that the graphene layer is expected to prevent the alloying of Au with Ni. In Figures 5.9(c,f) graphene on Ni intercalated with a full Au monolayer (nominally 1.1 ML) demonstrates in STM and LEED a perfectly periodic moiré pattern. A quantitative analysis is easier by the LEED than by the STM since the LEED superstructure can be evaluated relative to the distance between (0,0) and (1,0) spots without the need for any calibration. Our data reveals that the moiré is due to a $p(9 \times 9)$ superstructure. On panels (d,g) it is shown that further increase of the Au amount leads to a $p(8 \times 8)$ structure which is less ordered in STM but clearly distinguishable in LEED. When the Au is deposited as a wedge, scanning the sample during LEED shows a clear jump from

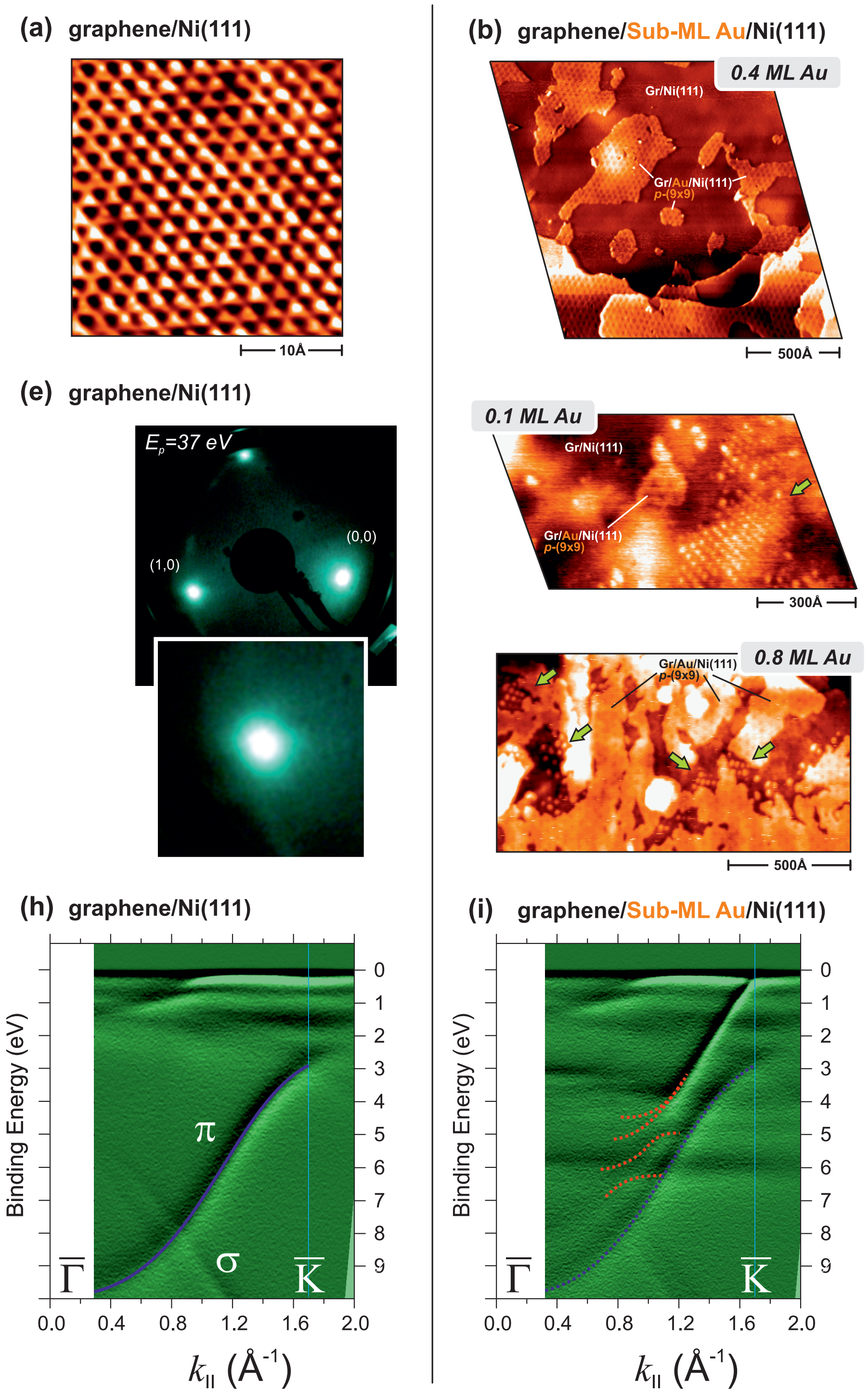

Figure 5.9: *(Figure is located on two pages.) Characterization by STM, LEED and ARPES of the graphene/Au/Ni(111) systems intercalated by increasing amounts of Au. The first column shows results for graphene/Ni. The second column shows results for various submonolayer amounts of Au. The third column shows graphene on Ni intercalated with a full Au monolayer (nominally 1.1 ML) with* 9×9 *reconstruction. The fourth column shows that a further increased amount of gold leads to a* 8×8 *reconstruction and an additional hybridization around 3 eV binding energy.*

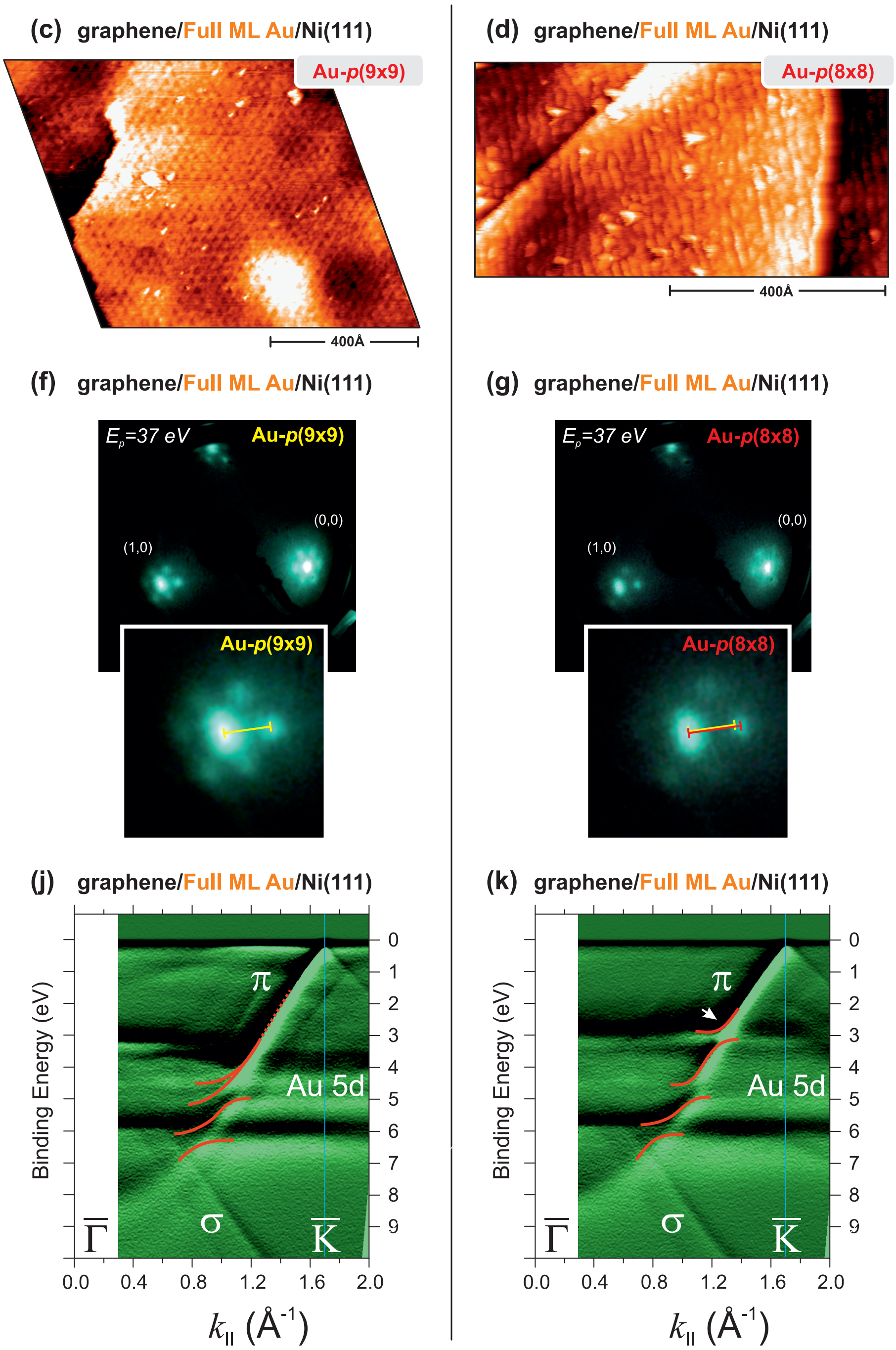
(c) graphene/Full ML Au/Ni(111)
Au-p(9x9)
400Å
(d) graphene/Full ML Au/Ni(111)
Au-p(8x8)
400Å
(f) graphene/Full ML Au/Ni(111)
E_p=37 eV
Au-p(9x9)
(1,0)
(0,0)
Au-p(9x9)
(g) graphene/Full ML Au/Ni(111)
E_p=37 eV
Au-p(8x8)
(1,0)
(0,0)
Au-p(8x8)
(j) graphene/Full ML Au/Ni(111)
Binding Energy (eV)
π
Au 5d
σ
Γ̄
K̄
0 1 2 3 4 5 6 7 8 9
0.0 0.4 0.8 1.2 1.6 2.0
$k_{\parallel}$ (Å^{-1})
(k) graphene/Full ML Au/Ni(111)
Binding Energy (eV)
π
Au 5d
σ
Γ̄
K̄
0 1 2 3 4 5 6 7 8 9
0.0 0.4 0.8 1.2 1.6 2.0
$k_{\parallel}$ (Å^{-1})

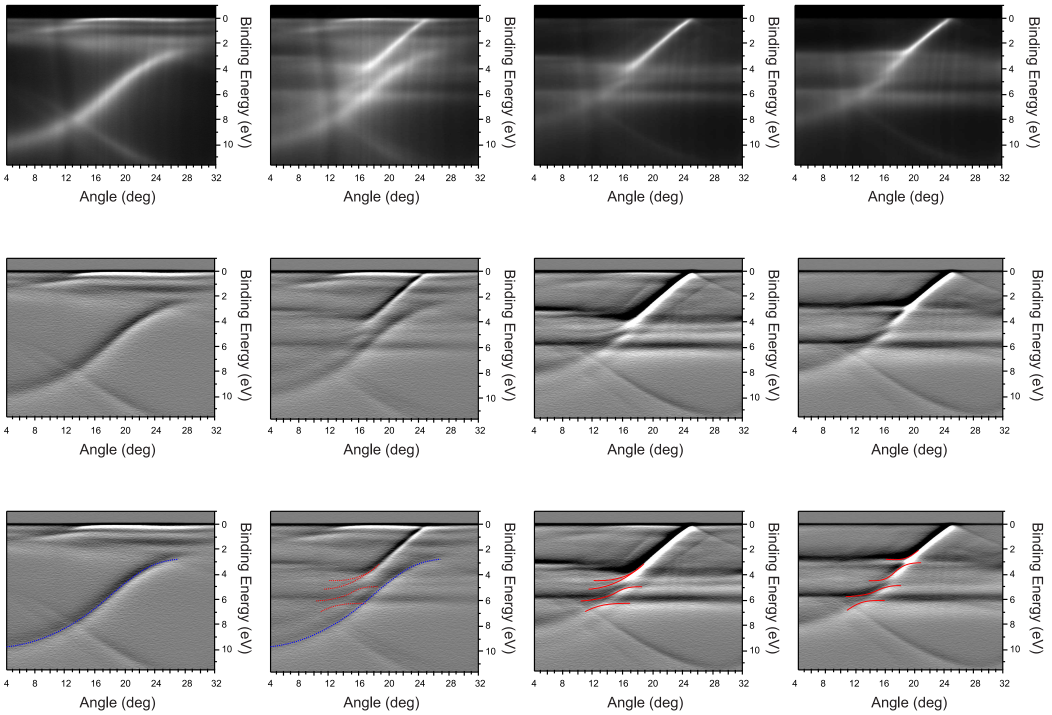

Figure 5.10: *Raw ARPES data from Figure 5.9. Raw intensity (top) and first derivative of intensity over energy without (middle) and with coloured lines emphasizing dispersion of hybridized bands (bottom).*

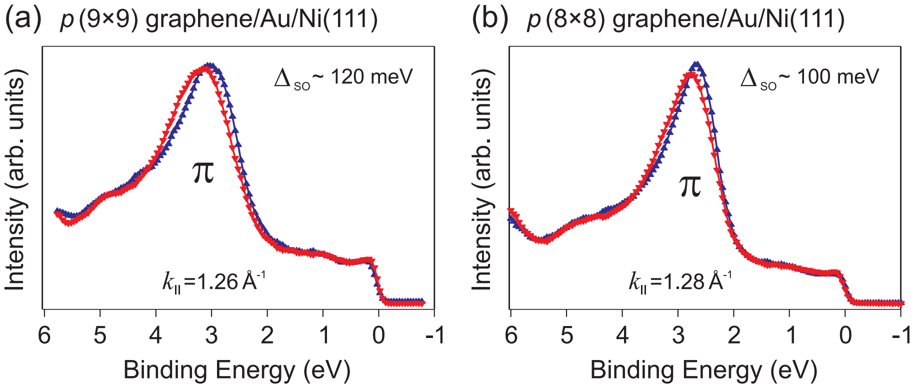

Figure 5.11: *Comparison of spin-orbit splittings of $p(9\times9)$ and $p(8\times8)$ superstructures. The spin splittings are approximately the same and large in both cases.*

the $p(9\times9)$ to the $p(8\times8)$ structure at a certain nominal concentration of Au close to 1 ML. In panels (h-k) the corresponding development of the hybridization of graphene with Au states from such a wedge-type sample is shown. The $p(8\times8)$ phase leads to an additional hybridization around 3 eV binding energy. However, rather surprisingly this hybridization does not further enhance the giant spin-orbit splitting as is seen from Figure 5.11. This indicates that the differences between the 9×9 and 8×8 superstructures play no role for the giant spin-orbit splitting.

Now we turn to *ab initio* theory in order to clarify the origin of the giant spin splitting. The calculations were again kindly performed by G. Bihlmayer. Modelling the 9×9 or 8×8 superstructures of the graphene/Au/Ni system would increase the unit cell by two orders of magnitude as compared to graphene. Moreover, it is unnecessary because both superstructures show a similar spin-orbit splitting. A $p(1\times1)$ structure with an on-top position for graphene on the Au monolayer has been chosen instead as is shown in Figure 5.12(a). The Au monolayer was assumed to be pseudomorphic [meaning $p(1\times1)$] also to the Ni(111) substrate which results in a compressed Au layer. The important Au-graphene distance has been chosen in Figure 5.12(a) based on the Fermi-level position from the experiment and in agreement with Ref. [109] as $d = 3.3$ Å.

The distance between graphene and the Au monolayer is a parameter of an enormous influence on the spin-orbit splitting in graphene as is shown in Figure 5.13. This finding is in line with calculations for pure metal surfaces Au(111) and Ag(111) where the surface and nuclear potentials were found to contribute multiplicatively to the Rashba splitting of the surface state [22, 110, 111]. In Fig. 5.13 the Fermi energy varies with the graphene-Au distance which allows us to make connection to the experiment. The sign change from *n*- to *p*-doping between d = 3.34 and 3.41 Å is in agreement with calculations for R-($\sqrt{3}\times\sqrt{3}$) graphene/Au(111) which give an equilibrium graphene-Au distance of 3.31 Å [109]. In addition, the behavior of the staggered potential (Δ_{st}) is shown. The staggered potential is induced by the Au lattice which breaks the equivalence of A and B sublattices

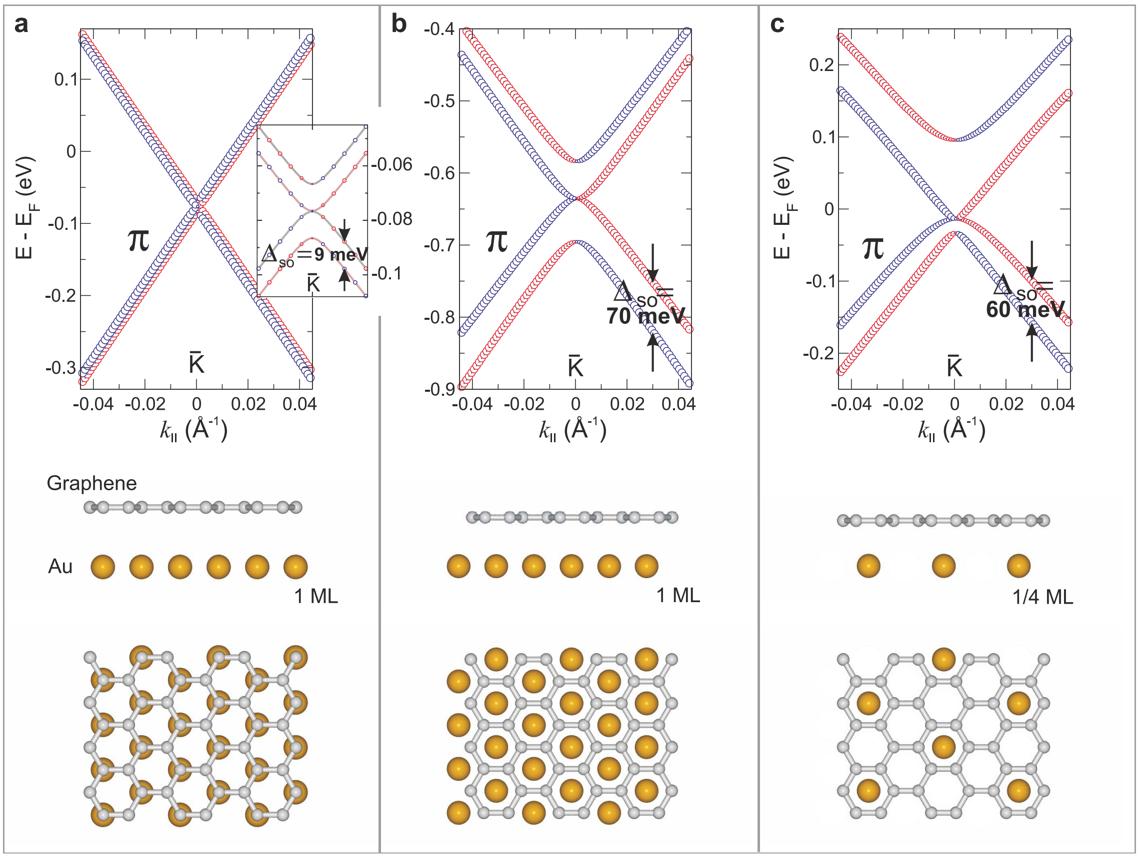

Figure 5.12: *(a) Results of ab initio calculations (open circles) showing the 9 meV Rashba-split Dirac cone for graphene on a gold monolayer in the on-top position at the equilibrium distance of 3.3 Å. In the inset a magnified view near the Dirac point is shown; Lines depict the dispersion as predicted from the analytical model by Rashba [70]. (b) The Au monolayer is laterally moved to the graphene hollow sites and can now be pressed into the graphene to the non-equilibrium distance of 2.5 Å without breaking the Dirac cone but enhancing the spin-orbit splitting to 70 meV. (c) Improved model with the Au atoms still sitting in the graphene hollow sites but diluted to 0.25 ML Au in a* $p(2\times 2)$ *geometry and at the equilibrium distance of 2.3 Å. Here, a spin-orbit splitting of* $\sim 50-100$ *meV and intact Dirac cone are achieved in equilibrium. Blue and red lines in panels (a-c) denote spin up and spin down bands. Atomic structures are schematically shown at the bottom of each panel. Calculation courtesy of G. Bihlmayer.*

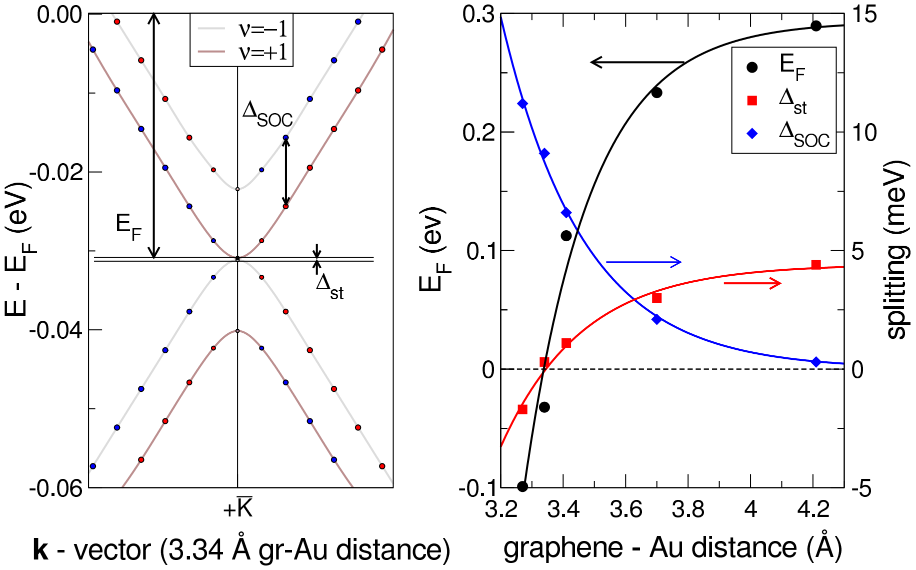

Figure 5.13: *Band topology and distance dependence of doping and spin-orbit splitting. Left: comparison of the analytically calculated Rashba-type band topology (solid lines) calculated by Rashba [70] to the calculation of Figure 5.12(a) (symbols) [$p(1 \times 1)$ on-top geometry] in the vicinity of the Dirac point finding full agreement. The line color gives the chirality (ν) and the symbol color (red and blue) the spin polarization. The spin-orbit splitting Δ_{SOC} amounts to 9 meV. For this structure the graphene-Au distance is varied as shown on the right side: graphene-Au distance dependence the Fermi energy, staggered potential and spin-orbit splitting. Calculation courtesy of G. Bihlmayer.*

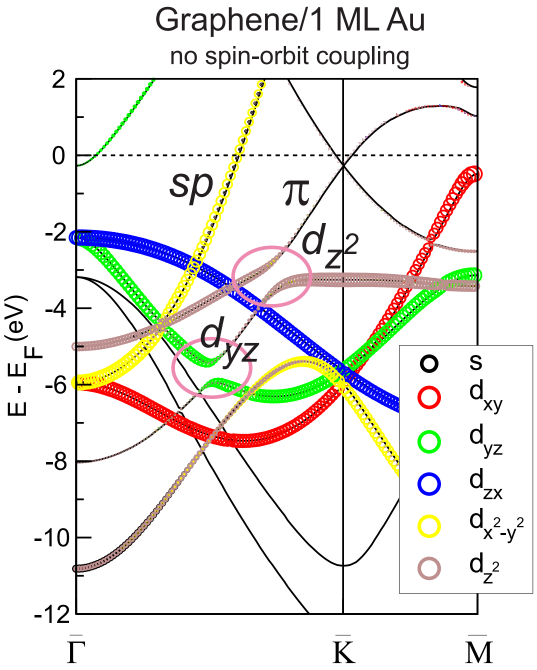

Figure 5.14: *Hybridization as the origin of the spin-orbit splitting in the graphene. Calculations without spin-orbit interaction reveal anticrossings and hybridization gaps which are due to orbital symmetries (see pink circles). (The spin-orbit splitting lowers the symmetry further and introduces additional anticrossings.) The model is* $p(1 \times 1)$ *graphene on a Au monolayer in the on top geometry as in panel (a) of Fig. 5.12. Since the π-band is made of* p_z *orbitals, the observed hybridization with* d_z^2 *and* d_{yz} *orbitals is determined by symmetry. Calculation courtesy of G. Bihlmayer.*

of the graphene if one sublattice is in the on-top position relative to the Au as shown in the geometry sketch of Figure 5.12(a). This effect from the staggered potential causes a splitting of the Dirac cone of a few meV for large graphene-Au distances but it increases strongly for short distances breaking the Dirac cone.

The experimental Fermi level corresponds with its slight *p*-doping to the distance 3.3–3.4 Å in the theoretical model, and data for the distance of 3.3 Å is shown in Figure 5.12(a). This is also the equilibrium distance calculated before for graphene/Au(111) [109]. According to analytical prediction, the band topology is peculiar around the $\overline{\mathrm{K}}$ point with two pairs of bands as was seen in Figure 2.5. This analytical model [70, 71] does not assume any specific surface configuration. The bands have so far been confirmed for freestanding graphene in a supercell geometry by density functional theory calculations for an applied field $E = 4.0$ V/nm [66]. In the *ab initio* calculations this field E is realistically created by the interface to Au. This was done in Figure 5.12(a) which shows the spin-orbit split bands at the Dirac point at $\overline{\mathrm{K}}$ for the on-top geometry. In the inset, these *ab initio* results (symbols) are magnified near the Dirac point and compared to the dispersion of the analytical model (solid line), which is fully confirmed. The spin-orbit splitting is 9 meV in Fig. 5.13 for $d = 3.3$ Å. A similar value of 8 meV was calculated recently [99].

In agreement with the experiment, our *ab initio* calculation reveals C π-Au d hybridization as the source of the spin-orbit splitting in the graphene. The graphene π-band (p_z orbitals) hybridizes indeed with the deeper Au 5d bands of d_{z^2} and d_{yz} type because of their matching symmetry. Despite the large distance of 3.3 Å the hybridization is strong which has not been considered in the literature in connection with graphene-noble-metal interfaces. This is best seen on Figure 5.14 after the spin-orbit coupling is turned off. This leaves only gaps caused by hybridization. We determine hybridization gaps of widths $E_{g,z^2} \approx 0.8$ eV and $E_{g,yz} \approx 0.5$ eV. Their absolute binding energies do not compare well to the experiment revealing the limitations of the Au monolayer as model substrate. This situation improves largely and the main C π-Au d hybridization moves from ~ 3 eV to ~ 4 eV below E_F when the Ni substrate is included in the calculation as is shown in Figure 5.15. The distance $d = 3.3$ Å nicely reproduces the position of the graphene states from the experiment, the same distance was used in the graphene-Au bilayer model of Figure 5.13. But we observe that between these two models the binding energies of the Au 5d bands suffer considerable changes due to the Ni substrate, mainly Au-Ni hybridizations which make the Au 5d bands difficult to distinguish. The d_{yz} band from Figure 5.14 originating at -2 eV at $\overline{\Gamma}$ and arriving at -6 eV at $\overline{\mathrm{K}}$ can be distinguished also in Fig. 5.15. A new Au 5d state appears at -1.5 eV at $\overline{\mathrm{K}}$. The Au sp band of Figure 5.14 is not observed in the experiment, and Figure 5.15 shows that the reason is that this band is very strongly hybridized with the Ni and disappears as a well-defined band.

The spin-orbit splitting in Figure 5.12(a) is 9 meV near E_F but increases strongly when the distance between graphene and Au is reduced (see Figure 5.13 for the detailed dependence on the distance). On the other hand, the Dirac cone is destroyed at closer graphene-Au distance, giving, e. g., for 2.5 Å a band gap of 40 meV at $\overline{\mathrm{K}}$. The reason for this is the broken A-B symmetry of carbon atoms in the on-top geometry which decreases for larger distances. In contrast, a hollow-site geometry preserves the A-B symmetry in the graphene. The geometry for this case is shown in Figure 5.12(b). Consequently, an intact Dirac cone is obtained in the hollow-site geometry also for smaller graphene-Au distances such as 2.3 Å which is shown in Figure 5.12(b). At this arbitrarily chosen interlayer distance of 2.3 Å a giant spin-orbit splitting of ~ 70 meV is created. However, at such a close distance repulsive interactions cost as much as 1 eV relative to the equilibrium separation and this geometry is thus considered unrealistic.

While the giant spin-orbit splitting apparently is difficult to reproduce by density functional theory in equilibrium, the intact Dirac cone is not. The intact Dirac cone is presently obtained with $p(1\times1)$ on-top graphene/Au and has also been found for $p(1\times1)$ graphene/Cu(111) where the on-top position is determined to be energetically favourable [109]. Relative to this $p(1\times1)$ on-top geometry which implies maximum A-B symmetry breaking, a moiré

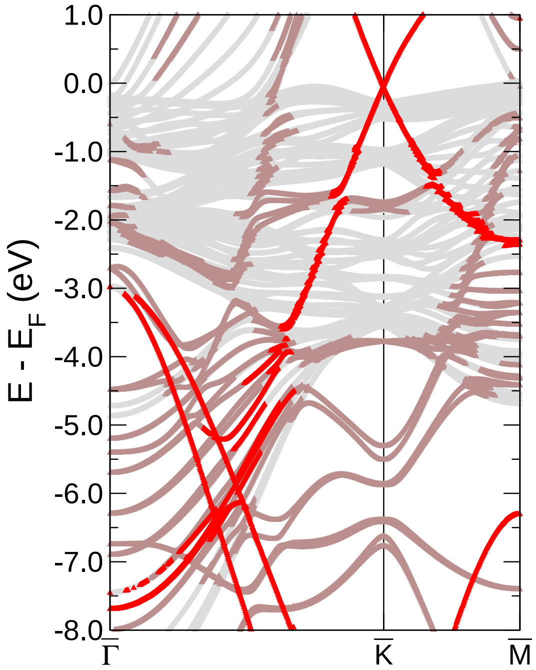

Figure 5.15: *Effect of the Ni substrate on the electronic structure at the graphene/Au interface. Colors mark states with a high probability density at the graphene (red), Au monolayer (violet), and Ni substrate (grey). Calculation courtesy of G. Bihlmayer.*

superstructure such as the 9×9 one necessarily breaks the A-B symmetry to a lesser or vanishing degree which is favourable for obtaining an intact Dirac cone. After having investigated other laterally shifted positions of the $p(1 \times 1)$ overlayer and a 4×3 moiré superstructure as well as corrugation in the graphene all yielding spin-orbit splittings of the order of 10 meV at equilibrium graphene-Au distances, the conclusion is that the giant spin-orbit splitting will not be accounted for by the sharp graphene-Au interface alone that the structural characterization by LEED and STM suggests as simplest case. This means that a model for a realistic splitting will have to include individual Au atoms which then can obtain a higher coordination to the carbon. Due to the resulting attraction and shorter distance this allows for a stronger spin-orbit splitting of the graphene π states. As seen above, at small graphene-Au separations the preservation of A-B symmetry becomes critical and leads us once again to the hollow site geometry. Figure 5.12(c) shows this situation for graphene/0.25 ML Au in a $p(2 \times 2)$ structure with the Au in the hollow site relative to the graphene. The distance between Au atoms and graphene layer is 2.3 Å (as for the nonequilibrium Au monolayer of Figure 5.12(b)) which is the equilibrium distance determined by our structural optimization. Figure 5.12(c) shows that this structure enhances the spin-orbit splitting to values between 50 and 100 meV while keeping the characteristic band topology and the Dirac point. This demonstrates that the measured giant Rashba splittings are quite reasonable from the *ab initio* point of view.

The 9×9 and 8×8 structures will include in the simplest case a substantial amount of Au atoms arranged in the hollow sites of graphene [112] but this does not imply a reduced distance, especially if one considers that 9×9 is also the structure which a Au monolayer alone forms on Ni(111) [106]. Therefore, the 9×9 and 8×8 superstructures are probably not relevant for the giant splitting and both give rise to only ~ 10 meV splitting in agreement with our observation shown in Figure 5.11.

The previously measured data [7] were characterized by a smaller ~ 13 meV spin-orbit splitting, and this low-splitting phase is in principle in agreement with our present calculations for the full Au monolayer. The published [7] band dispersion measured along $\overline{\Gamma \mathrm{K}}$ reflects the presence of a sample with structural defects. It contained substantial contributions of rotated domains visible as characteristic $\overline{\Gamma \mathrm{M}}$ dispersions appearing along $\overline{\Gamma \mathrm{K}}$ which is not the case in the present data even when the amount of intercalated Au is varied systematically from zero to more than 1 ML as was shown in Figures 5.9 and 5.10. The intercalation process under the graphene, including that of Au, is at present far from understood. The accepted main route is via defects in the graphene [113], and for large molecules this can be confirmed by STM directly [114]. The presence of many domain boundaries facilitates the intercalation and apparently results in the low-splitting phase. Intercalation of Au works, however, also in samples which are free of defects over large distances. The temperatures required for intercalation and for the initial graphene formation are very similar in the graphene/Au/Ni(111) system so that an opening and closing of the graphene bonds appears possible during intercalation. This would more likely happen for a perfect graphene layer and could lead to more Au atoms that are locally closer to the graphene, either as subsurface Au or as adatoms.

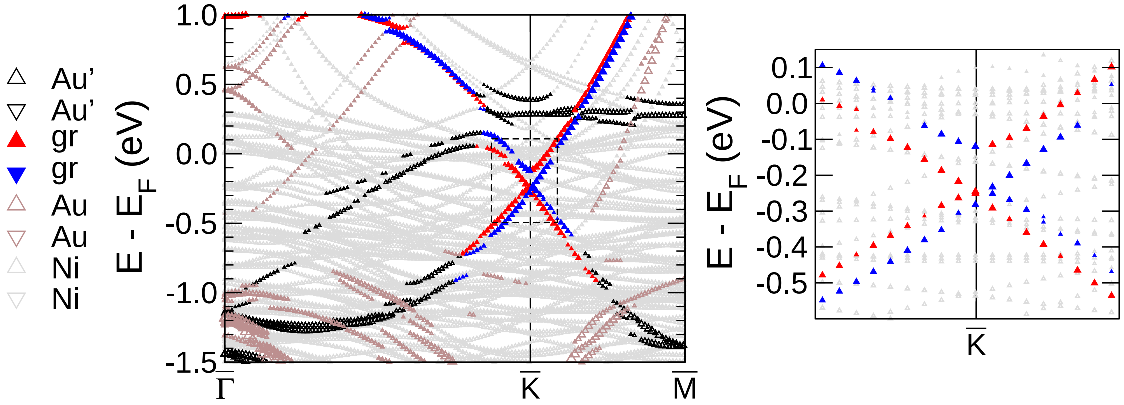

Figure 5.16: *Same model as in Figure 5.15 but with additional Au adatoms, i.e. graphene is sandwiched between 0.25 ML Au and 1 ML Au on top of a 3 ML thick Ni substrate. This calculation explores again the influence of the Ni substrate (grey symbols) under the Au monolayer (violet symbols) on the graphene π-states (red and blue symbols). The upward and downward direction of the triangles marks the spin, in particular the upward red and downward blue triangles for graphene states. Left: The states due to the additional Au adatoms (black triangles, Au') can be seen to interact with the graphene states through different hybridizations than the Au monolayer. Right: Zoom near the Dirac point. The spin-orbit split Dirac cone from the graphene-Au bilayer model of Fig. 5.12(c) is thus confirmed in the present, more realistic, configuration. The fact that higher and lower energies are not symmetric about the Dirac point is not due to the Ni substrate but to the $p(2 \times 2)$ 0.25 ML Au adatoms, like in Figure 5.12(c). Calculation courtesy of G. Bihlmayer.*

The $p(2 \times 2)$ plot of Figure 5.12(c) is useful for demonstrating that an enhancement of the spin-orbit coupling in graphene by sparsely distributed Au atoms is possible in an equilibrium structure but it does not imply that the Au arrangement possesses such an ordered structure. We can certainly exclude that carbon atoms in graphene are substited by Au atoms. Their size would correspond to two carbon atoms and the resulting distortion would manifest itself in STM. Another possibility are non-intercalated residual atoms above the graphene for which we have no direct experimental evidence because of room temperature measurements. They have a high mobility on the surface and should be shifted along by the STM tip. In order to explore a realistic model which includes the Ni substrate, the band dispersion for a structure of graphene sandwiched between 0.25 ML Au and 1 ML Au on top of 3 ML Ni has been calculated as well. The result is presented in Figure 5.16 and gives practically the same Dirac cone with giant spin splitting as in Figure 5.12(c).

To summarize the results of the present section, we report a giant Rashba splitting in graphene in contact with Au reaching up to 100 meV. This splitting is caused by the graphene-Au hybridization. While a flat Au monolayer can account for only ~ 10 meV spin-orbit splitting as has been reported in Ref. [7], a structure of laterally more separated Au atoms residing in hollow-site positions closer to graphene provides at the equilibrium graphene-Au distance an enhanced spin splitting of $\Delta_{SO} \sim 50$–100 meV, a realistic Fermi level position, and an intact Dirac cone. We attribute the simultaneous presence of both 100 meV and 10 meV splittings to the coexistence of areas with and without extra Au either as adatoms or immersed under the graphene.

5.1.4 Atmospheric stability

For use in real devices, the peculiar electronic and spin structure of the graphene/Au/Ni(111) system must be stable when the system is exposed to atmosphere, otherwise a way to protect it has to be found. Exfoliated graphene is known to be stable in air [115] and in acid solution [116], but it has been assumed that exposure to air is a major source of doping [11]. In fact, charge inhomogeneities due to doping have been found to affect the minimum conductivity [117] of graphene through regions in which the Fermi energy shifts randomly [118]. In this situation, pentacene was recently suggested as protection layer for graphene [119]. A 15 nm thick pentacene layer deposited on graphene/SiC(0001) was shown to lead to the same n-type doped graphene dispersion after deposition and removal by annealing. Graphene in spintronics [32] is particularly vulnerable due to the interfaces with magnetic transition metals and their high reactivity with air. In the present case, it can be expected that the reaction of oxygen with the Ni surface either dopes the graphene or disrupts it. The former would be seen as a pronounced shift in the Dirac point relative to the Fermi energy and the latter would replace the itinerant π states by nondispersive carbide states. On the other hand, certain selfprotection of graphene/Ni(111) has already been seen by electron spectroscopy: Auger electron spectroscopy indicates a protective character of graphene toward exposure to air [120]. Moreover, the spin polarization of

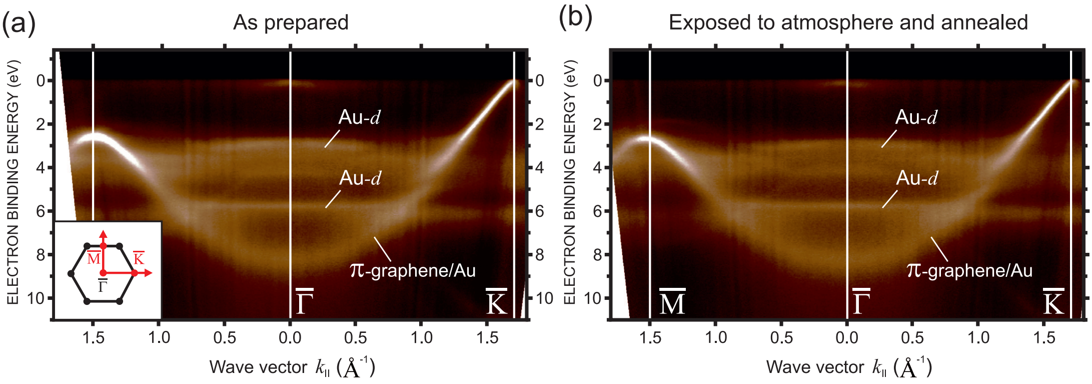

Figure 5.17: *Angle-resolved photoemission intensity measured at 62 eV photon energy (a) before and (b) after exposure to air for 10 min and short annealing at 800 K. The inset in panel (a) shows the directions in the Brillouin zone.*

secondary electrons from graphene/Ni(111) was recently found to remain constant after exposure to 5×10^{-6} mbar oxygen for 30 min [37].

To study the influence of the atmosphere on the graphene/Au/Ni(111) system, samples were exposed to air between 10 min and 5 hours at room temperature in a relative humidity between 45% and 55% and, subsequently, reintroduced through a load lock into the ultrahigh vacuum chamber. Figure 5.17 shows angle-resolved photoelectron intensity measured at 62 eV photon energy (a) before and (b) after exposure to air for 10 min and short annealing at 800 K. We see at this stage no difference in the electronic structure caused by the exposure. In particular:

1. No carbon of the graphene has become carbidized which would lead to extra nondispersive states.
2. No immediate graphene/Ni(111) interface is created which would shift the $E(k)$ dispersion by 2 eV to higher binding energy [6, 7, 104].
3. No apparent band gap opens at E_F.
4. No apparent doping occurs.

In order to investigate the doping state of the graphene π band in greater detail, Figure 5.18 displays measurements in the direction perpendicular to $\overline{\Gamma\mathrm{K}}$ (a) near the $\overline{\mathrm{K}}$ point (b) as prepared, (c) after exposure to air for 1 hour, and (d) after subsequent annealing. The cut through the Dirac cone shows the Dirac point in Figure 5.18(b) located at ≈ 80 meV above the Fermi level, according to our fit. The fit results give the same values within 20 meV after exposure and after annealing. No detectable energy shift means that the doping state of graphene is not affected by the exposure to air. When the sample is measured after exposure to air and without subsequent annealing (Fig. 5.18(c)), the photoemission

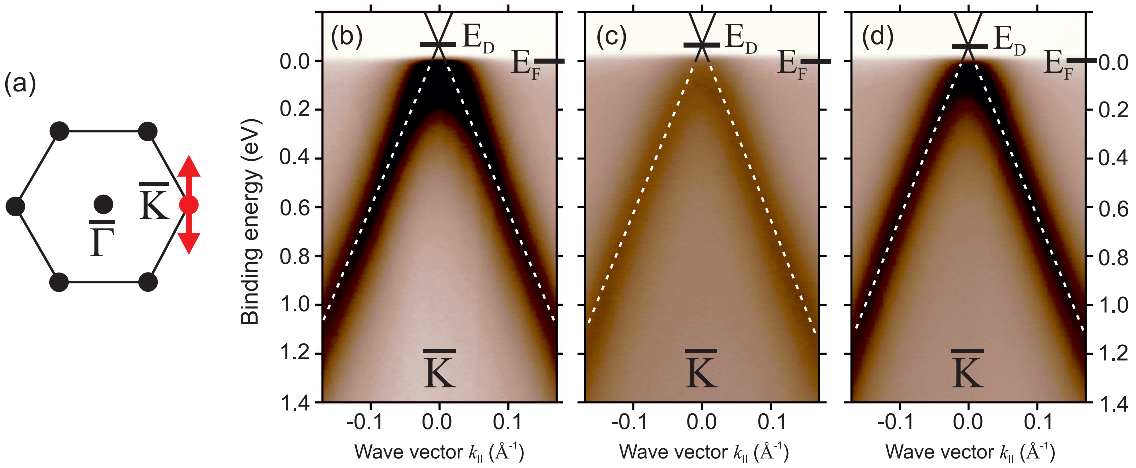

Figure 5.18: *(a) Direction in the graphene Brillouin zone of the angle-resolved photoemission measurements presented in panels (b-d), i.e., normal to* $\overline{\Gamma \mathrm{K}}$ *through the* $\overline{\mathrm{K}}$ *point. (b) as prepared graphene/Au/Ni(111), (c) after exposure to air for 1 hour, (d) after subsequent annealing.*

intensity is suppressed but the Dirac cone position and shape are preserved, thus, the peculiar graphene electronic properties are also preserved.

Figure 5.19 shows a typical lineshape of the graphene π band. It is seen that the photoemission intensity is at first reduced but after annealing is regained and that the broadening has almost not increased. The reduction in intensity for the graphene as exposed is most likely due to adsorbed water from the atmosphere, which does not react with graphene but as overlayer reduces the photoemission intensity from the graphene bands. The broadening has increased only very little from 0.48 eV to 0.54 eV after exposure to atmosphere and practically recovers by the annealing. The small broadening means that not only no doping occurs in average across the probed sample area of ~ 0.01 mm^2 but also that the inhomogeneity of the doping stays very small. A possible reason has been pointed out recently. While an icelike H_2O layer has a strong influence on the electronic properties of graphene [121], in a H_2O cluster the dipole moments tend to cancel on average leaving almost no effect on the graphene [122].

No changes were detected also with LEED and XPS (except that the peaks-to-background intensity ratio changes) even after direct transfer of the sample from air to measurements without additional heating.

We have tested the Rashba spin-orbit splitting in graphene/Au/Ni(111) by spin- and angle-resolved photoemission on a sample exposed to air for 5 hours. Figure 5.20 shows the spin-integrated photoemission spectrum $(I^{\uparrow}+I^{\downarrow})$ for $k_{\|}=0.16\text{Å}^{-1}$ (measured from the $\overline{\mathrm{K}}$ point) along with the spin polarization $[p=(I^{\uparrow}-I^{\downarrow})/(I^{\uparrow}+I^{\downarrow})]$. The change of sign of p at 1 eV binding energy shows the lasting Rashba splitting. The splitting is about 50 meV in this case.

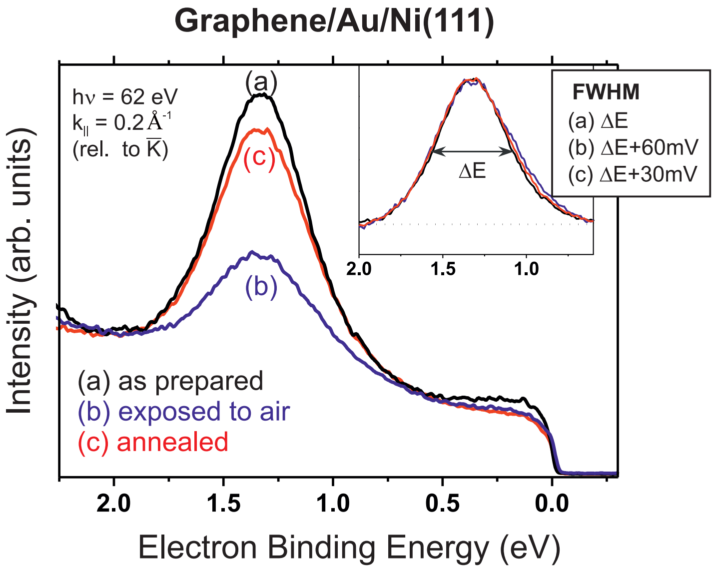

Figure 5.19: *Behavior of the linewidth for the example of* $k_{\|} = 0.2\ \text{Å}^{-1}$ *measured from the* $\overline{\mathrm{K}}$ *point: (a) as prepared, (b) after exposure to atmosphere (increase in linewidth by 10% with large suppression of intensity), and (c) after annealing (almost full restoration of original intensity and linewidth). This means that not only no doping occurs in average but also no variation in the doping.*

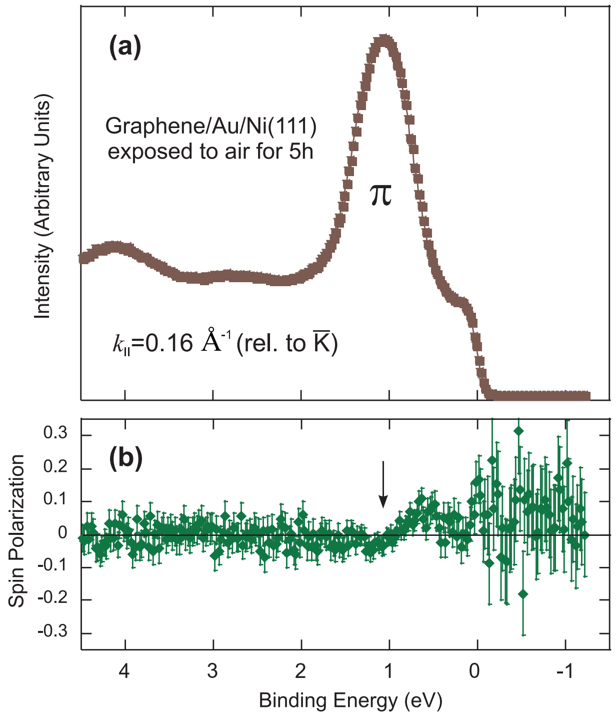

Figure 5.20: *(a) Spin-integrated photoemission spectrum of the graphene/Au/Ni(111) after exposure to air for 5 hours and (b) its spin polarization revealing a substantial Rashba-type spin-orbit interaction.*

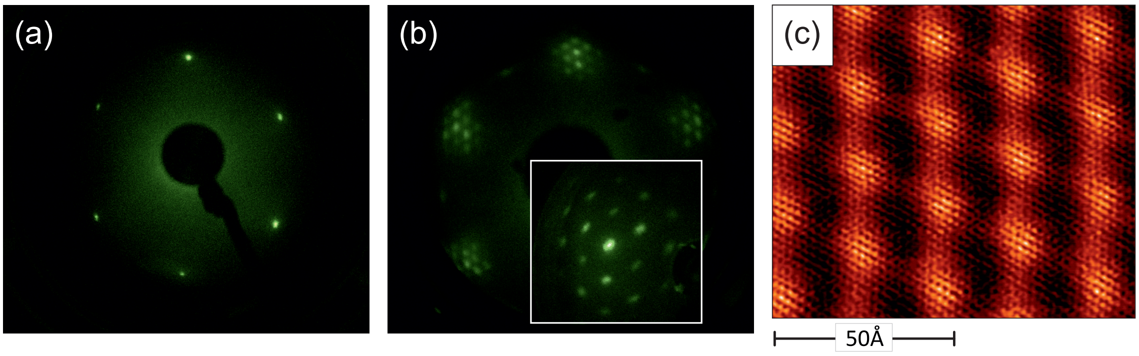

Figure 5.21: *LEED of (a) clean Ir(111) surface and (b) graphene on Ir(111) with moiré superstructure. (c) STM of graphene/Ir(111) with the same moiré superstructure.*

In conclusion, we have shown that Au-intercalated graphene/Ni(111) is self-protective against carbidization and oxidation of the Ni and against disruption of the spin-dependent electronic structure of graphene. The protection of ferromagnets could be interesting for nanostructures as well. Co forms islands on W(110) when heated and these can be graphene-covered while maintaining their topology [123]. It would be interesting to check their stability in air. Moreover, the observation that graphene is self-protective against doping could mean that doping of graphene by nonmetals requires open edges which are rare on graphene/Au/Ni(111).

5.2 Graphene on Iridium

Graphene on iridium is an intensively studied system [113,124–127] containing the graphene monolayer. The graphene is known as weakly interacting with Ir(111) with a linear π band dispersion forming the peculiar Dirac cone in angle-resolved photoemission with a slight p-doping [124, 128]. The clean Ir(111) surface was prepared by cycles of Ar^+ sputtering followed by annealing at 1600 K. There exist several phases of graphene on Ir(111). The moiré-type graphene layer (R0 phase) was grown epitaxially by chemical vapor deposition of propylene (C_3H_6) at $\sim$ 1500 K and a partial pressure of 3×10^{-8} mbar. Like for Ni the self-limitation of this growth method results in a single graphene layer. A mismatch of $\sim$ 10 % of the graphene and iridium lattices leads to a corrugation [125] and a moiré superstructure observed in LEED (Figure 5.21(b)) and STM (Figure 5.21(c)). In angle-resolved photoelectron spectroscopy, this moiré superstructure is also visible as ’reflections’ or ’replicas’ of the graphene π bands and *minigaps* at the intersection between such ’reflections’ and the main π bands [124, 128]. Both effects correspond to the expectations for a band structure in the repeated zone scheme of the superlattice.

The band structure of graphene on Ir(111) measured by angle-resolved photoelectron

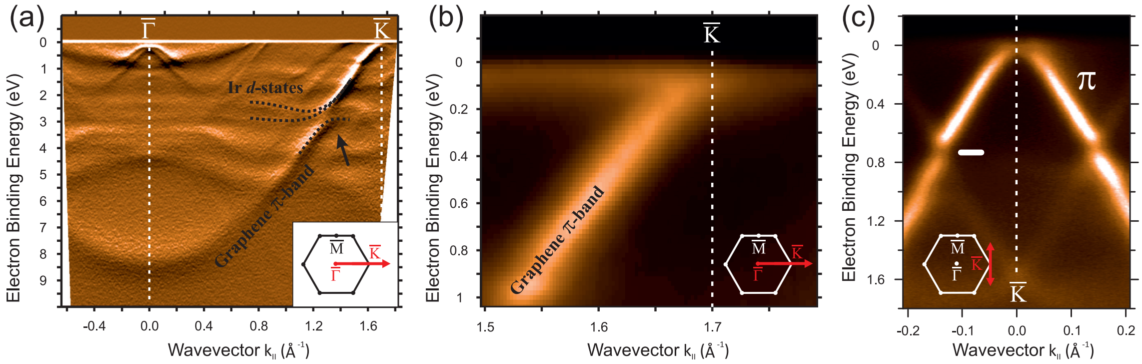

Figure 5.22: *Angle-resolved photoemission from graphene on Ir(111). (a) First derivative of intensity over energy of the* $\overline{\Gamma \mathrm{K}}$ *dispersion. Hybridization between the graphene* π *band and Ir d states is shown by a black arrow and dashed black lines. (b) Magnified view of the region near the* $\overline{\mathrm{K}}$ *point. (c) Dirac cone measured in the direction normal to* $\overline{\Gamma \mathrm{K}}$ *. Insets in (a-c) show directions of measurements in the graphene Brillouin zone.*

spectroscopy is shown in Figure 5.22. In panel (a) an overview dispersion is shown in the $\overline{\Gamma \mathrm{K}}$ direction of the graphene Brillouin zone. The graphene π band starts from ~ 8.3 eV binding energy at the $\overline{\Gamma}$ point and reaches the Fermi level near the $\overline{\mathrm{K}}$ point. In panel (b) a magnified view of the region near the $\overline{\mathrm{K}}$ point and the Fermi level is shown. Again, only part of the total picture is visible due to the destructive interference [84]. To see the full picture a measurement normal to the $\overline{\Gamma \mathrm{K}}$ direction was done and the result is shown in panel (c). An intact linear Dirac cone is clearly visible with minigaps at the crossing points with π band 'reflections' [124]. The Dirac point is located almost at the Fermi level with a small *p* doping. The presence of the intact Dirac cone similar to the case of free graphene layer was observed previously for this system [124] and means a quasifree nature of graphene on iridium with a small graphene-iridium interaction strength.

The giant Rashba effect in graphene on gold which we discussed in section 5.1 is related to the high atomic number of gold ($Z = 79$) and hybridization of the graphene π band with gold *d* states. We showed that at other, low-Z, systems like graphene/Ni, graphene/Co, graphene/Ag/Ni and graphene/SiC there no Rashba effect could be detected. To verify that high-Z materials can generally induce a spin-orbit coupling in graphene, we decided to study additionally the graphene/Ir(111) system. Iridium was selected due to several reasons:

1. Iridium is also a high-Z material with $Z = 77$.
2. Iridium features also *d* bands, comparable with gold.
3. We observed a spin-orbit split surface state of iridium.

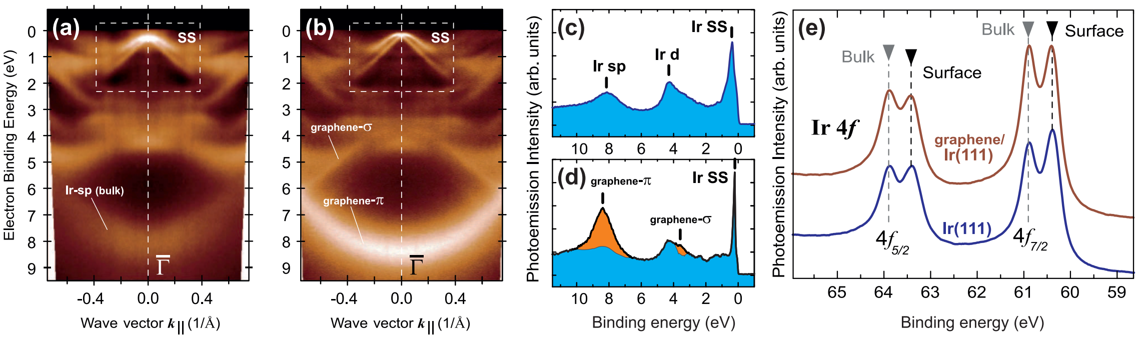

Figure 5.23: *(a,b) Angle-resolved photoemission overview measured at $h\nu = 62$ eV for (a) Ir(111) and (b) graphene/Ir(111). The white frame marks a spin-orbit split iridium surface state. (c,d) Normal emission spectra from panels (a) and (b), respectively. Orange colored parts of panel (d) denote difference between Ir(111) and graphene/Ir(111) spectra. (e) Ir 4f core level spectra measured at $h\nu = 110$ eV photon energy for Ir(111) (blue) and graphene/Ir(111) (orange).*

4. Graphene on Ir(111) can be grown of high quality.

5. Graphene on Ir(111) is quasifreestanding similarly to graphene on gold.

In the following sections we will discuss a Rashba-split iridium surface state and its incredible stability upon graphene formation on top of Ir(111), a giant Rashba effect in the R0 phase of graphene/Ir(111) with splitting of ~ 50 meV. Finally, a structural study of rotationally displaced graphene phase with a spin splitting of ~ 25 meV is presented with the conclusion that the size of the Rashba splitting can be controlled by the graphene growth parameters.

5.2.1 Iridium Surface State

We will start with description of the spin-orbit split surface state of Ir(111) which is an important manifestation of the Rashba effect at the Ir surface. In Figure 5.23(a) an overview band structure s shown. There is an iridium *sp* band with minimum around 8 eV binding energy at the $\bar{\Gamma}$ point as well as split states around the Fermi level. These split states are known to be an iridium surface state [129] related to the L-gap surface state of Au(111) but upside down (negative effective mass) due to a different order of bulk bands. A magnified view of these surface states is presented in Figure 5.24(a). Their splitting looks like a classical Rashba effect and they resemble a pair of spin-orbit split bands shifted in $k_{\|}$ by ~ 0.075 Å^{-1} relative to each other. The Rashba parameter is $\alpha_R = 1.3 \times 10^{-10}$ eV m. This is the largest Rashba effect reported so far for an elemental metal.

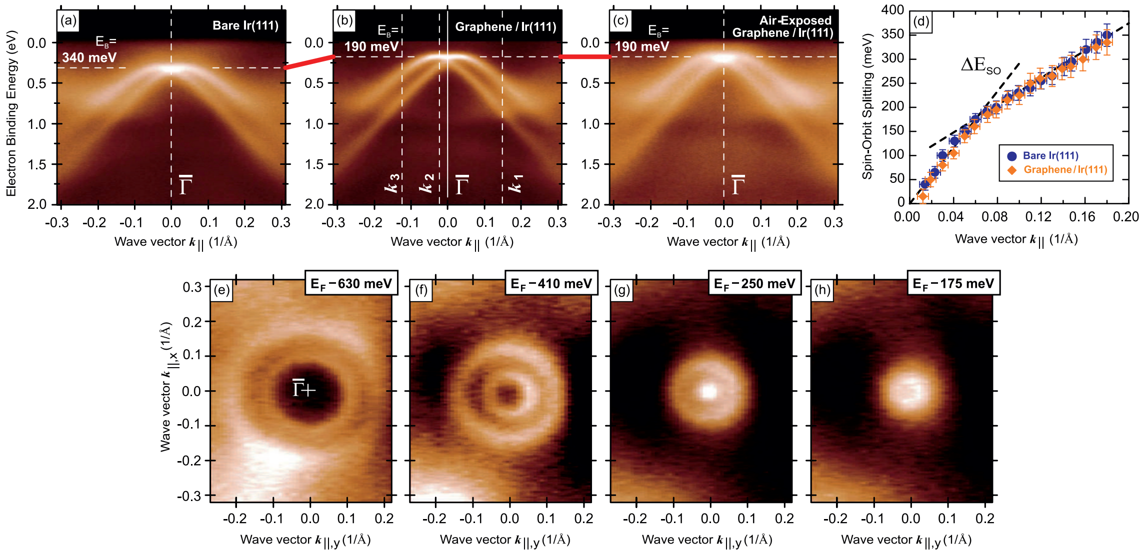

Figure 5.24: *(a-c) Magnified view of the iridium surface state region for (a) clean Ir(111), (b) graphene/Ir(111) and (c) graphene/Ir(111) exposed to air. In panel (b) locations of spin-resolved measurements are marked by k_1, k_2 and k_3. (d) Comparison of surface state splitting for Ir(111) and graphene/Ir(111). (e-h) Constant energy cuts of full photoemission mapping of the surface state region.*

Figure 5.23(b) shows an overview band structure of the graphene/Ir(111) system on the same scale as Fig. 5.23(a). Band structures with and without graphene are very similar with the main difference being the intensity of the band around 8 eV binding energy at the $\bar{\Gamma}$ point. In pure Ir(111) this is the iridium *sp* band but in graphene/Ir(111) it is the graphene π band which by chance disperses very similarly to the Ir *sp* band but has significantly larger intensity. In the band structure of graphene/Ir(111) also the graphene σ states are visible proving additionally the formation of the graphene layer. Surface states are by their nature very sensitive to the influence of adsorbates. Remarkably, the iridium surface states are still present after the graphene layer is formed on top of Ir(111). This observation is the main point of the current section and will be discussed below in detail.

Figures 5.23(c) and (d) show spectra taken from panels (a) and (b), respectively, in normal emission ($\bar{\Gamma}$ point). To compare the two systems in question, in panel (d) the difference between the spectra is marked in orange. The graphene σ states have a rather low intensity but the graphene π band is visible as an intense peak on top of the Ir *sp* peak. Iridium $4f$ core levels with and without the graphene layer are shown in Figure 5.23(e). Measurements were done with $h\nu = 110$ eV photon energy. There is no apparent difference between the two cases even for the surface components of the core levels. Such behaviour shows very weak graphene-iridium interaction strength which is in line with the previously discussed quasifreestanding band dispersion.

To study the iridium surface state modification upon graphene layer formation in detail,

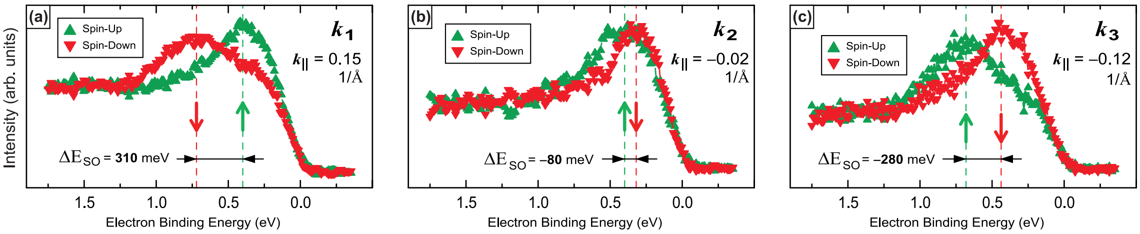

Figure 5.25: *Spin-resolved measurements of the iridium surface state under the graphene layer at points shown by dashed vertical lines in Figure 5.24(b).*

we measured that region with high-resolution angle-resolved photoemission. The result is presented in Figures 5.24(a) and (b). After the graphene layer is formed on top of Ir(111) there is only a slight change of these surface states. Te band maximum is shifted by 150 meV to lower binding energy, from $\sim$ 340 meV to $\sim$ 190 meV. In panel (d) the spiltting of the surface state for Ir(111) and graphene/Ir(111) is compared. The splitting is equal and linear with $k_{||}$ in agreement with the Rashba model. A kink at $k_{||} = 0.06$ Å^{-1} is due to interaction of the surface state with iridium bulk *d* bands [129]. We conducted a full photoemission mapping of the region near the $\overline{\Gamma}$ point of this surface state when it is located under the graphene layer. The results are presented in Figure 5.24(e-h) as constant energy cuts at binding energies 630, 410, 250 and 175 meV. The circular structure agrees well with the theory of the Rashba effect. At 630 and 410 meV two circles corresponding to two opposite spin direction rotations in the Rashba model are observed and at $\sim$ 250 meV the inner circle has shrinked to a point.

Direct spin-resolved measurements of the iridium surface state under the graphene layer shown in Figure 5.25 show that the splittings are due to the spin and reverse with the sighn of $k_{||}$. This spin polarization is apparently fully preserved after formation of the graphene layer. As we discussed before, to the Rashba effect could lead a surface potential gradient and also the substrate effect when the surface state wavefunction penetrates into the substrate core region. Figure 5.24(d) gives us an additional information in this context, i.e., the absence of a change in the spin-orbit splitting when graphene is formed on top of the iridium surface proves that the observed splitting size is due to the large atomic number of the iridium substrate atoms and not due to the surface potential. It is in line with results of previous observation of a substrate induced splittings in Au/W, Ag/W, Au/Mo and Ag/Mo systems [26] and additionally proves necessity of the high-*Z* materials when we want to effectively produce the spin-orbit splitting in graphene by the substrate effect.

Surface states are generally very sensitive to the environment and due to this are usually not suitable for use in devices. In section 5.1.4 we have observed the atmospheric stability of the graphene/Au/Ni system. The Dirac cone, doping level and spin splitting were preserved after exposure of the system to atmosphere. In the case of graphene/Ir(111) we have an intact spin-orbit split surface state which is covered by a graphene layer. Such coverage could serve as a protection layer similar to the graphene/Au/Ni case and this is

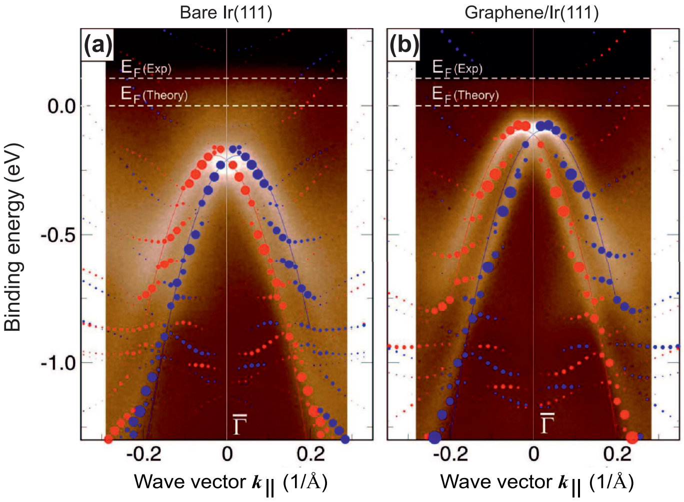

Figure 5.26: *Superimposed experimental and theoretical data of the iridium surface state at the $\overline{\Gamma}$ point for the case of (a) bare Ir(111) surface and (b) graphene/Ir(111) system. Large red and blue dots denote contributions of surface localized bands of p_z character with opposide directions of spin circulation. Calculations by G. Bihlmayer.*

indeed shown in Figure 5.24(c). There the graphene/Ir(111) system is shown after exposure to ambient atmosphere for 15 min. This venting does not change the size of the splitting and energy position of the surface state. The presence of a higher background relative to the pure graphene/Ir(111) system in panel (b) is due to some remaining adsorbates. The results of graphene/Au/Ni and graphene/Ir taken together lead us to the conclusion that the graphene layer, weakly interacting with the substrate, can be considered as an ideal protection layer.

To clarify the existence and stability of the iridium surface state *ab initio* calculations were performed for us. To simulate the bare and graphene covered surfaces, a 15 layer film of iridium was used and covered by graphene expanded to the Ir(111) in-plane lattice constant. The graphene sheet was placed at a distance of 0.35 nm from the surface. The surface state can be identified by the spin-polarization due to the Rashba effect in the uppermost two Ir(111) layers. The Rashba parameter was obtained from a fit in the $\overline{\Gamma K}$ direction and amounts to 1.3×10^{-10} eV m with and without graphene. Figures 5.26(a,b) present the calculated band structure of the iridium surface state superimposed with the experimental photoemission data. With the exception of a rather small difference of 0.1 eV in Fermi energies, experimental and theoretical results are in very good agreement. In particular, the relative energy shift of the Ir surface state upon adsorption of graphene as well as spin-orbit splittings are reproduced by the calculations.

To summarize the present section we mention the observation and study of the Rashba split surface state of Ir(111), its presence and stability against the environment when the

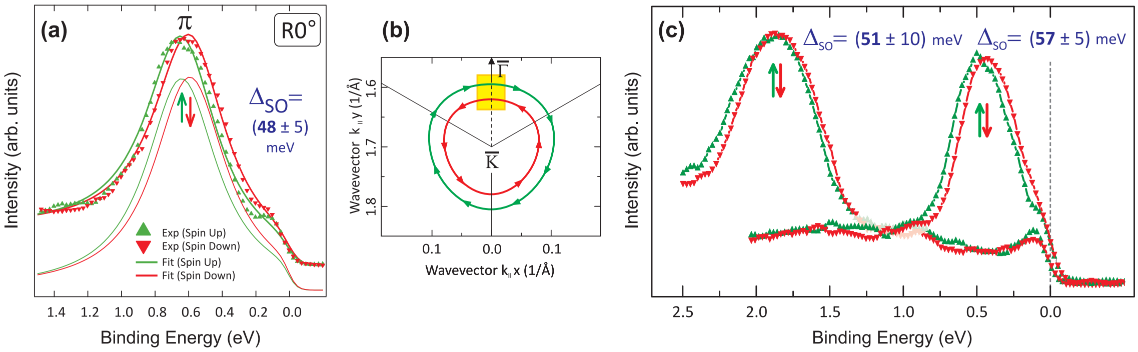

Figure 5.27: *(a) Spin-resolved photoemission of the graphene π band of graphene/Ir(111) showing the giant Rashba spin-orbit splitting of* $\sim$ 48 *meV. The measurement was done at* $h\nu = 62$ *eV in the* $\overline{\Gamma \mathrm{K}}$ *direction at* $k_{\|} \sim 1.57$ Å^{-1}. *(b) Schematic view of the measurement position in the graphene Brillouin zone with a constant energy cut of the Dirac cone. (c) Two more points measured in the same* $\overline{\Gamma \mathrm{K}}$ *direction show an approximately constant splitting.*

iridium is covered by a graphene layer. This behaviour and the very large size of the Rashba effect are confirmed by density functional calculations.

5.2.2 Giant Rashba effect in graphene

The presence of the Rashba-split surface state on Ir(111) and graphene/Ir(111) is very promising for inducing a giant Rashba spin-orbit splitting in the graphene. In Figure 5.27(a) a spin-resolved measurement of the graphene π band of the graphene/Ir(111) system is shown. There a splitting of $\sim$ 50 meV is observed which is a giant if one compares to the intrinsic spin-orbit coupling of a free graphene layer. In panel (b) the measurement position is schematically shown using a constant energy cut of a spin split model Dirac cone. By arrows the spin rotation directions are marked corresponding to the Rashba model. In panel (c) two additional spectra are presented showing the nearly constant splitting value for different wave vectors and binding energies. The measurements of Figure 5.27 were done in the $\overline{\Gamma \mathrm{K}}$ direction of the graphene Brillouin zone. With varying $k_{\|}$ the spin polarization 'moves together' with the graphene π band. This means that the graphene π band is spin split and the effect is not an accidental overlap of the π band with a spin polarized background of iridium states. This is important since the background is high due to Ir *d* states as compared to graphene on Au. Additionally, there is a surface projected band gap of Ir(111) close to the $\overline{\mathrm{K}}$ point as is shown in Figure 5.28(b) and several spin-resolved measurements were done on the π band inside the gap. This further reduces the possible influence from photoemission from iridium bands close to the $\overline{\mathrm{K}}$ point on the spin polarization of the graphene π band. The origin of the observed spin-orbit splitting becomes more clear when one looks at Figure 5.28(a) where the graphene

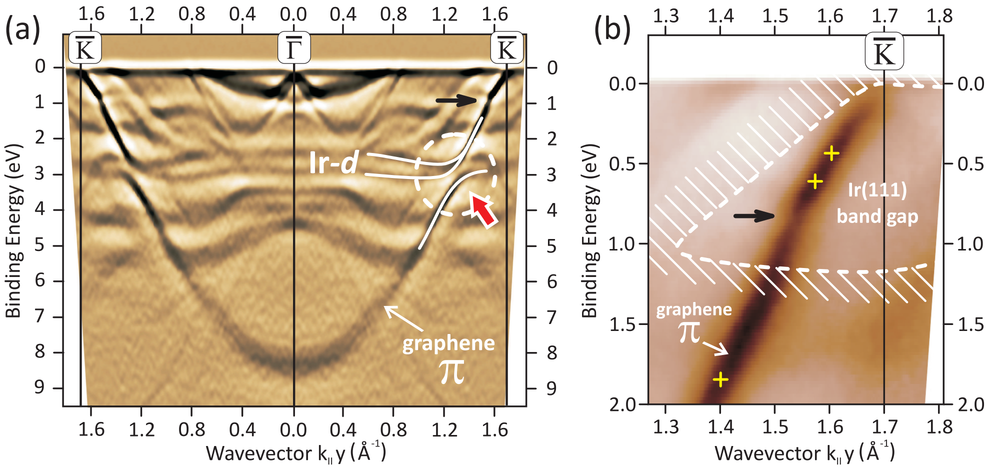

Figure 5.28: *(a) Graphene/Ir(111) band structure in the* $\overline{\Gamma \mathrm{K}}$ *direction (second derivative of intensity over energy). The hybridization region of the graphene* π *band with Ir d bands is marked by a dashed circle and a red arrow. (b) Magnified region near the* $\overline{\mathrm{K}}$ *point. Only one half of the graphene Dirac cone is visible here. Crosses show where the spectra from Figure 5.27 were measured. A white dashed line shows the surface projected band gap of Ir(111). Black arrow marks the mini-gap.*

π band and iridium *d* states are marked. Despite the quasifree nature of graphene on iridium a hybridization between the graphene and iridium bands is observed with ~ 0.5 eV hybridization gap. This hybridization together with the large atomic number of iridium is the origin of the giant spin-orbit splitting of the graphene Dirac cone, i.e., electrons from the graphene p_z orbitals approach the high potential gradient around the Ir nuclei and this enhances the spin-orbit interaction. The situation is similar to the case of graphene on gold which we already discussed in detaile.

5.2.3 Control of Rashba effect by rotational displacement

In the previous Section we discussed the so-called R0 phase graphene on Ir(111) which is grown at a rather high temperature around 1500 K. The R0 phase is very uniform at a large scale with a characteristic and sharp moiré pattern observed in LEED and STM as shown in Figures 5.21(b,c). From the literature it is known that at lower temperatures graphene can grow on Ir(111) in many different rotation variants like 14°, 30° etc. [126, 127]. In a very recent publication [127] the growth temperature dependence of the graphene alignment was studied and a smooth transition of LEED images from the standard R0 phase moiré into a bar-like superstructure was observed when lowering the growth temperature. There was no clear explanation of the observed superstructures. In Figure 5.29 our characterization by LEED and STM of the low-temperature phase is presented. Both LEED and

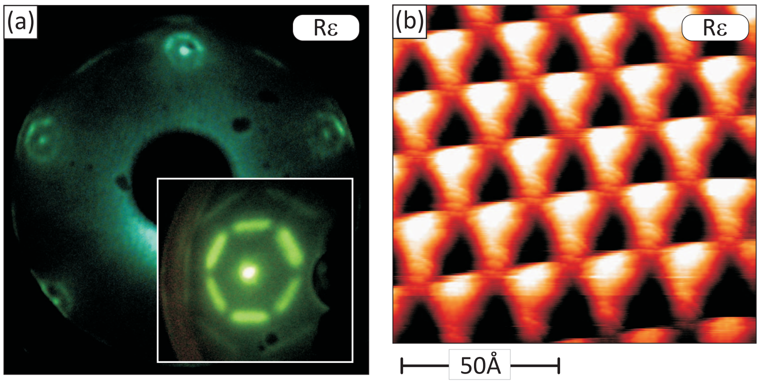

Figure 5.29: *(a) LEED and (b) STM images of the low-temperature phase graphene on Ir(111). They differ drastically from the R0 phase presented in Figure 5.21.*

STM pictures are drastically different from the R0 phase presented in Figure 5.21(b,c): in the LEED image there is a characteristic bar-like superstructure and in the STM image there is a triangular structure with an anomalously large *z*-corrugation of electronic origin. The STM images were obtained at tunneling voltage $+2$ mV and current 25 nA.

The Rashba effect depends strongly on the strength of the interaction with the substrate and, therefore, the dramatic change observed in LEED and STM could indicate that also the induced spin-orbit splitting of the graphene π band may change. We did a full photoemission mapping around the $\overline{\mathrm{K}}$ point to see the Dirac cone in detail and the results are presented in Figure 5.30. Panels (a) and (b) compare the R0 phase of graphene on Ir(111) and the low-temperature phase. A giant splitting of the Dirac cone of ~ 400 meV is observed with some differences but rather similar to what could be expected in the case of a giant Rashba splitting. In panel (c) the second derivative of intensity over energy of the same data as in panel (b) is presented revealing more details. In panels (a-c) black arrows mark umklapp-induced minigaps. In panels (d) and (e) a constant energy cut at 600 meV below the Fermi level is shown. As we discussed in section 2.2.2 the Rashba effect on the graphene Dirac cone gives rise to two concentric circles. Here we see two intersecting circles. Further analysis of the data in panels (b-e) results in the consistent interpretation of the observed structure as overlapping photoemission signal from several graphene domains rotated by a small angle $2\varepsilon = 2.8^\circ$ relative to each other. This is presented schematically in panel (f). This small rotation angle ε could vary depending on the growth temperature, therefore, we suggest to call this graphene phase generally 'Rε *phase*'. In view of the small angles involved, angle-resolved photoemission proves in this case a very precise tool for structural characterization, quite differently from its original objective.

To directly check that the two observed bands split by 400 meV are not spin polarized branches of the same spin-split graphene π band we conducted spin-resolved measurements presented it Figures 5.31(a,b). In this geometry (normal to $\overline{\Gamma\mathrm{K}}$ at points shown

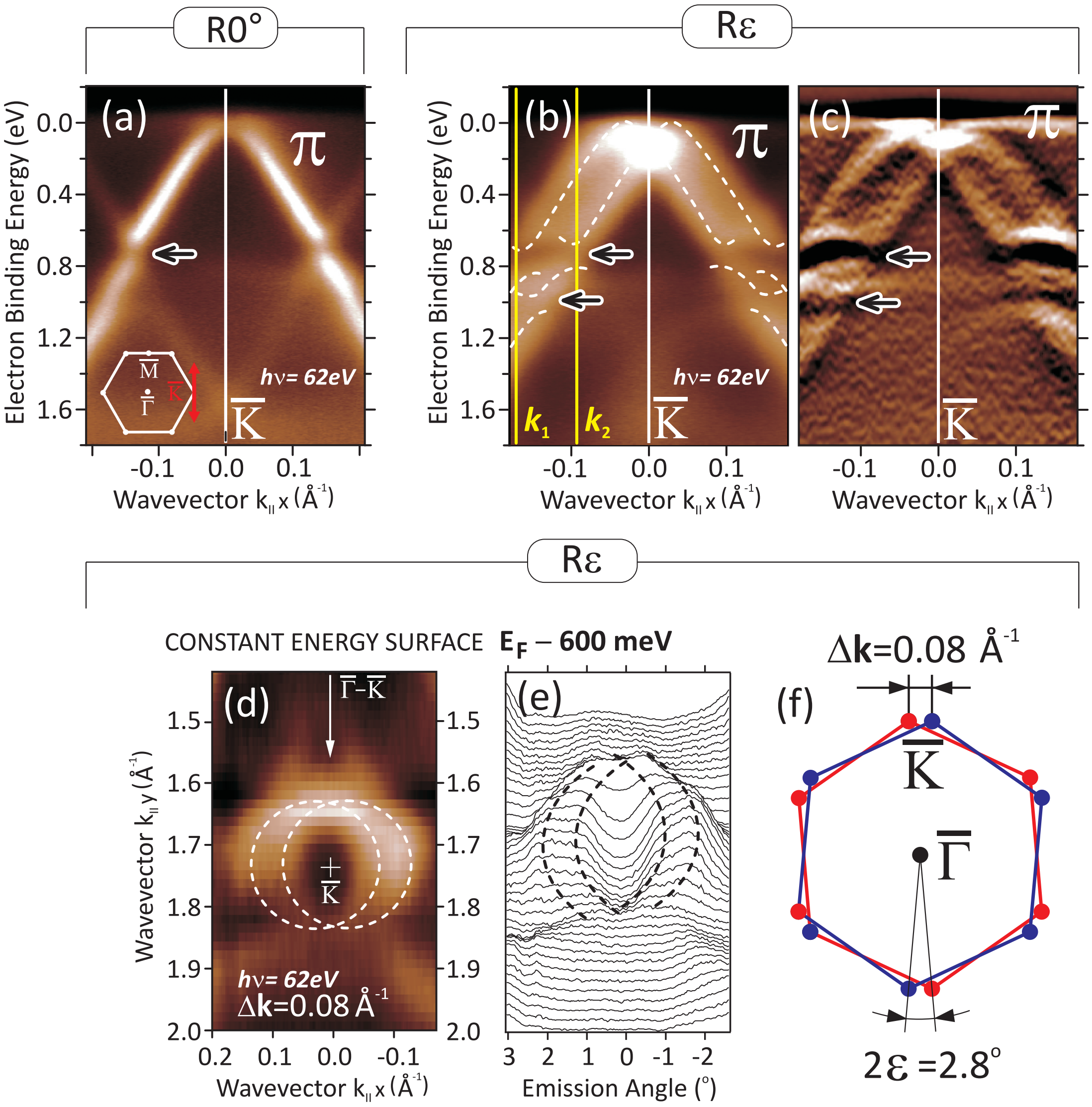

Figure 5.30: *(a) Dirac cone of the R0 phase graphene on Ir(111) measured by angle-resolved photoemission. (b) Dirac cone of the Rε phase. (c) Second derivative of intensity over energy of data from panel (b). (d,e) Constant energy cut from full photoemission mapping around the* $\overline{\mathrm{K}}$ *point of the Rε phase reveals two shifted circles. (f) Model explaining the observed structure as two Dirac cones due to overlap from rotated Brillouin zones.*

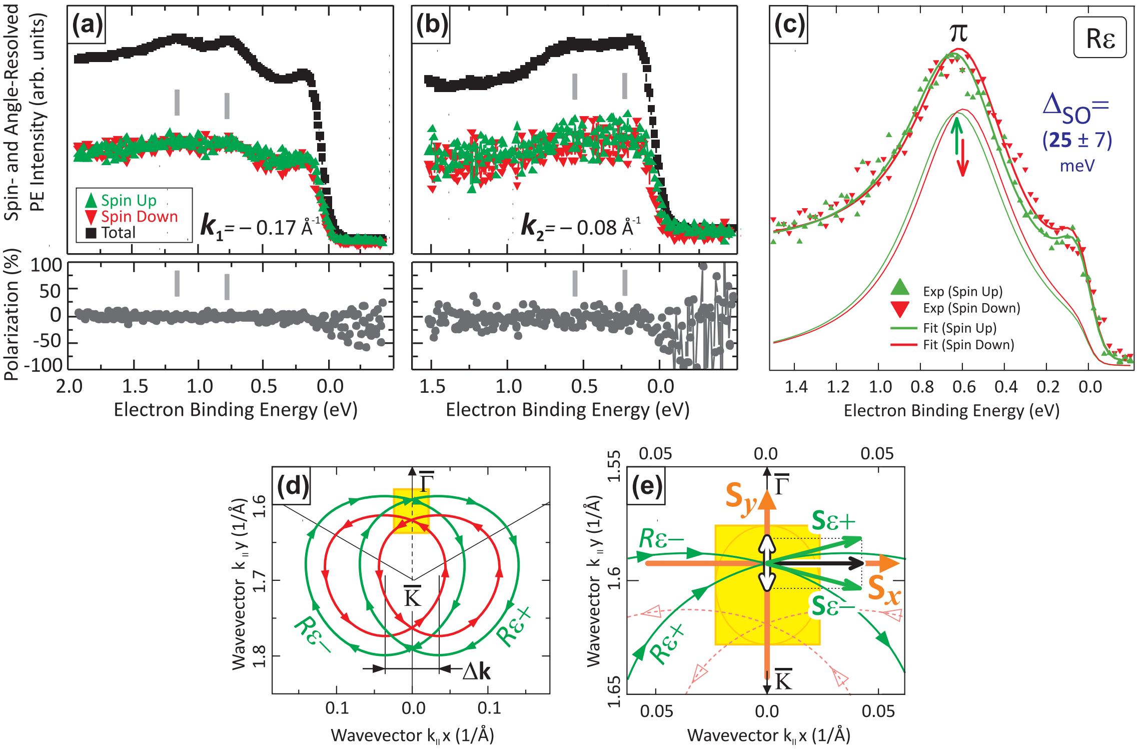

Figure 5.31: *(a,b) A draft spin-resolved measurement of the strongly split Dirac cone in the Rε graphene phase. Measured at k_1 and k_2 points shown by yellow vertical lines in Figure 5.30(b). In this direction the intensity of peaks is very small, but enough to conclude that the two observed bands are not a spin-split band. (c) Spin-resolved spectra of the Rε phase in the same geometry as for the R0 phase to make a direct comparison of the spin splitting size. The geometry is shown in panel (d). (e) Drawing explaining that the measured magnitude of spin splitting is very little affected by the rotation of the graphene domains.*

in Figure 5.30(b)) the photoemission intensity is very small for spin-resolved measurements and the statistics is not good. However, it is enough to conclude that there is no large spin polarization which is expected for the Rashba effect. This is in line with the angle-resolved photoemission mapping result that these bands are due to a geometrical effect and are just a superposition of photoemission signals from rotated graphene domains. Each of these two bands could still be spin-split due to a smaller Rashba effect, but in the discussed geometry the intensity is not enough to resolve it. In another geometry as shown at Figure 5.31(d) (similar to the R0 case in Figure 5.27(b)) the intensities of two bands add and in this geometry the photoemission interference effect is smaller, which leads to a rather high intensity in Figure 5.31(c). This spin-resolved measurement resolves $\sim$ 25 meV splitting of the π band in the Rε phase. Compared to the intrinsic spin-orbit splitting in free graphene, 25 meV is still a giant effect, only two times smaller than in the R0 phase and 4 times smaller than in graphene/Au.

In Figure 5.31(d) the energy-momentum region where the photoelectrons are collected by the spectrometer is marked by a yellow frame. According to the Rashba effect in graphene at any given energy the spins are tangential to the constant energy contours of the π-band and follow them. Taking into account our experimental geometry this does not change in the photoemission transition [71]. Due to the **k**-offset of the acquisition region from the $\overline{\Gamma}\,\overline{\mathrm{K}}$ lines of the Brillouin zones of rotated domains Rε- and Rε+, the spins of photoelectrons will have slightly different orientation at every **k**-point of the isoenergetic contours inside of the acquisition frame. The situation is zoomed in Figure 5.31(e) (for the sake of simplicity the yellow frame depicts the experimental **k**-resolution while the real region of acquisition is not rectangular but elliptical due to circular shape of the spectrometer aperture).

Now one has to understand to which extent the rotation of spins within the spectrometer frame can affect the measured spin polarization. Our spin-detector acquires two projections of Mott-scattered electron spins which are in the plane of the sample surface. One projection falls on the axis S_y which is collinear to the $\overline{\Gamma}$-$\overline{\mathrm{K}}$ direction of the Brillouin zone of *non-rotated* graphene. Another projection goes to the axis S_x which is orthogonal to S_y. These axes are shown in Figure 5.31(e) in orange and bold. Indeed, projections of spin on S_y [white arrows in panel (e)] can be effectively compensated in the photoemission signal because of superposition of spins **S**ε- and **S**ε+ coming from the domains Rε- and Rε+, respectively. In contrast, the projections of **S**ε- and **S**ε+ on the axis S_x [black arrow in panel (e)] are added and will be acquired by the spin detector. The average angular deviation of spins from the axis S_x within the determined width of the spectrometer frame ($\sim$0.06Å^{-1}) is estimated as 15°. Instead of a precise treatment of the azimuthal dependence of the Mott scattering, we obtain for such a small angle the projection onto S_x in simple trigonometric terms as cos(15°) which corresponds to 97% of real spin polarization. This shows that the measurement of the Rashba splitting of the Rε phase of graphene is negligibly affected by the rotational displacement of Dirac cones and correct spin-resolved measurements from this graphene phase are feasible.

The present structural model of the Rε phase as distribution of rotated graphene do-

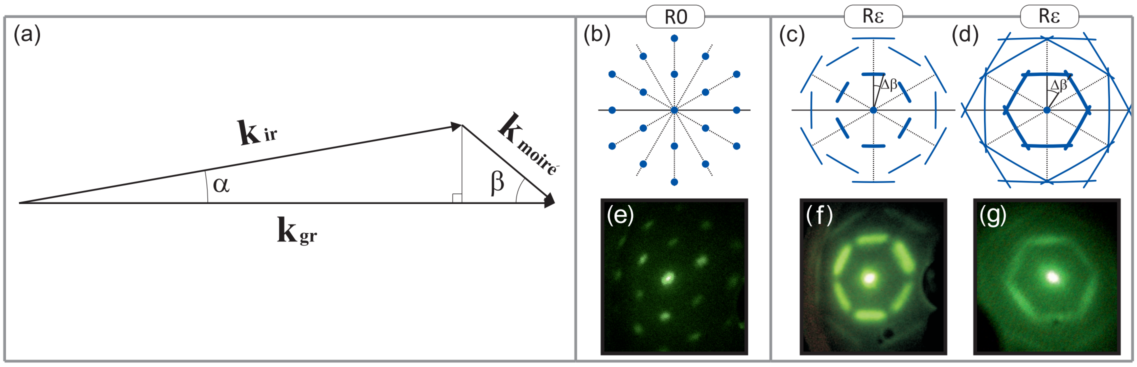

Figure 5.32: *(a) Determination of the moiré vector and simulation of LEED for (b) the R0 phase, (c) the Rε phase with randomly distributed rotation angles* $-1.5^\circ < \varepsilon < 1.5^\circ$, *(d) the Rε phase with* $-3.5^\circ < \varepsilon < 3.5^\circ$. *(e-g) Experimental observation of corresponding LEED superstructures.*

mains has to be checked for its consistency with the peculiar LEED and STM pictures of Figure 5.29. Concerning the LEED, a principal question is why a superstructure of nearly straight dashes appears. It is possible to answer on this question with the help of the vector construction shown in Figure 5.32(a). The moiré reciprocal lattice vector is defined by

$$\mathbf{k}_{\text{moiré}} = \mathbf{k}_{\text{Gr}} - \mathbf{k}_{\text{Ir}} \tag{5.1}$$

with reciprocal lattice vectors $\mathbf{k}_{\text{Gr}}$ of graphene and $\mathbf{k}_{\text{Ir}}$ of Ir. In the R0 phase, $\mathbf{k}_{\text{Gr}}$ and $\mathbf{k}_{\text{Ir}}$ directions coincide, and we can determine the moiré lattice constant $a_{\text{moiré}}$ from:

$$a_{\text{moiré}} = (1/a_{\text{Gr}} - 1/a_{\text{Ir}})^{-1} \tag{5.2}$$

It is ≈ 27 Å, i. e., 10 Ir unit cells correspond to 11 graphene unit cells.

In the case of a rotated graphene monolayer on Ir(111) the vector equation 5.1 leads to a less obvious result compared to the R0 case. Let graphene be rotated by an angle α relative to the Ir, then moiré pattern rotates by an angle β [see Figure 5.32(a)]:

$$\tan\beta = \frac{\sin\alpha}{\frac{k_{\text{Gr}}}{k_{\text{Ir}}} - \cos\alpha} \tag{5.3}$$

and the length of the moiré reciprocal lattice vector becomes:

$$k_{\text{moiré}} = \frac{k_{\text{Ir}}\sin\alpha}{\sin\beta} \tag{5.4}$$

From equations (5.3) and (5.4) one finds that with rotation of the graphene layer on top of Ir(111) the moiré pattern rotates about 10 times faster and the moiré lattice con-

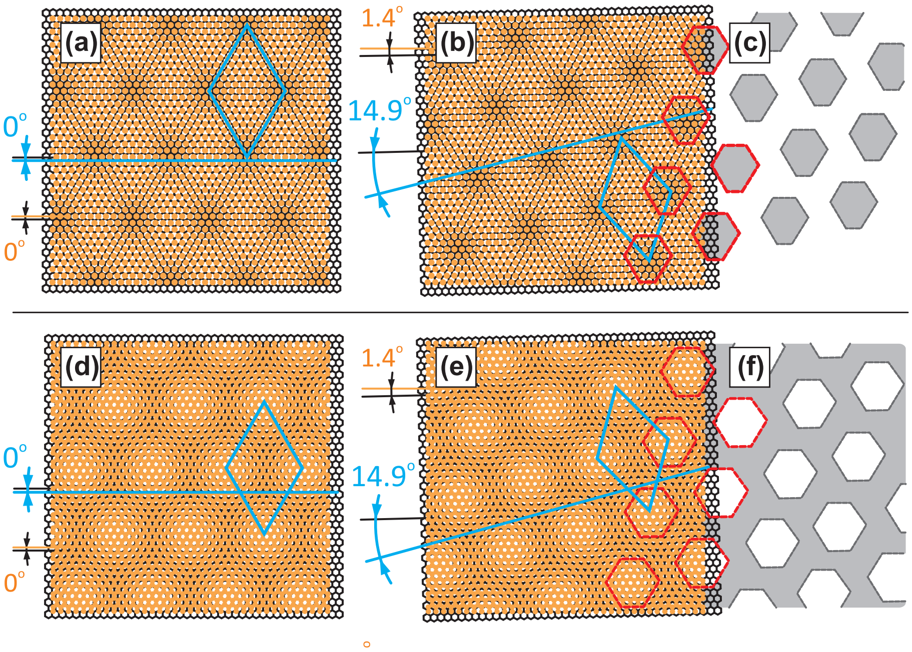

Figure 5.33: *Real-space simulation of the moiré structures. Ir atoms (orange) are superimposed on graphene (black); (a) and (b) demonstrate why a large rotation of the moiré pattern is observed. A large rotation of the moiré pattern [*14.9°*in (b)] happens due to a small rotation of the graphene domain [*1.4°*in (b)]. Simulations in (a) and (b) treat the Ir(111) substrate as a single atomic layer and generate a moiré pattern which resembles a superstructure of bubbles (or triangles) (c) characteristic of Rε graphene; (d) and (e) additionally take into account a second (subsurface) Ir layer and produce a nanomesh-like moiré pattern with inversed topographic contrast (f) which is typical for the non-rotated R0 phase of graphene. Gray color in (c) and (f) denotes higher topographic corrugation.*

stant decreases. Consequently, the moiré superstructure pattern in the LEED rotates and *increases* in size. This rotation together with the increase in size produces the dashes if one presumes that there are many graphene domains with rotational displacement angles densely distributed in a certain angular range.

Figure 5.32(b) shows a simulation for the R0 phase graphene and Figure 5.32(c) shows a simulation according to equations (5.3) and (5.4) for the Rε phase where graphene domains are randomly rotated in a range $-\alpha \leq \varepsilon \leq \alpha$, where $\alpha \approx 1.5°$. Figure 5.32(d) displays results of the simulation for graphene domains rotated even stronger ($\alpha \approx 3.5°$). In a recent paper [127] the same dash-like structures appeared in the LEED but remained unexplained. In panels (e-g) our experimental observation of corresponding superstructures is shown measured from the graphene/Ir(111) system formed at different temperatures.

The particular triangle structure seen by the STM in Figure 5.29(b) for the Rε graphene

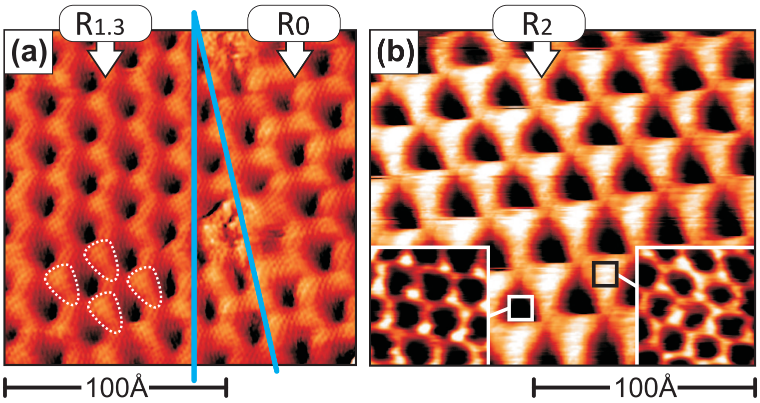

Figure 5.34: *STM images showing several local rotated domains which can be identified by their boundaries to other domains. The dash-like LEED patterns are then created by the contributions from a multitude of such domains with a distribution of rotation angles. Insets to (b) display atomically resolved measurements of dark and bright triangles of the moiré pattern.*

phase can also be explained based on the moiré pattern of rotated graphene domains. We have performed a simulation of the moiré patterns emerging in graphene domains rotated relative to the Ir(111) substrate by various angles. For the beginning we have treated the Ir substrate as a single (topmost) atomic layer of Ir(111). The top half of Figure 5.33 presents results for this case. Moiré patterns obtained for R0 graphene and for graphene rotated by 1.4° relative to the Ir substrate are shown in Figures 5.33(a) and 5.33(b), respectively. One can see that the moiré structure rotates by a ten times larger angle (14.9°), fully in agreement with equation (5.3).

Interestingly, the periodicity of the moiré pattern obtained for R0 graphene in Figure 5.33(a) correlates with experiments, but the type of its topographic corrugation does not. Indeed, darker areas in Figure 5.33(a) [and in 5.33(b) for the rotated domain] correspond to the sites where graphene is not in registry to the Ir layer and where it has higher z-corrugation. Such correspondence was established by atomically resolved STM measurements which are shown in Figure 5.34. Moiré sites with low z-corrugation display one graphene sublattice enhanced due to the local breaking of $A-B$ symmetry caused by the in-registry (i.e., on top) placement of the graphene lattice above Ir atoms. On contrast, areas with higher z-corrugation exhibit a typical honeycomb graphene structure, which means out of registry (hollow site) configuration without symmetry breaking.

As a result, the moiré structures from Figures 5.33(a) and 5.33(b) show up in STM images as a superstructures of 'bubbles', schematically depicted in panel (c) [gray color in Figures 5.33(c) and 5.33(f) corresponds to higher topographic corrugation]. This is in a remarkable contradiction to most of our STM data which show that aligned R0 graphene looks the other way around - like a nanomesh with holes [see Figures 5.21(c) and 5.33(a)]. Searching for the reason of such discrepancy, we could qualitatively adjust the occurrence of the moiré pattern in our simulations by taking into account the *second* (subsurface) atomic layer of the Ir(111). Simulations performed for R0 and 1.4°-displaced graphene with subsurface Ir atoms included are reported in Figures 5.33(d) and 5.33(e), respectively. One sees that the contrast of the moiré pattern is now fully inverted and the topographic pattern changes to nanomesh-like [Fig. 5.33(f)].

We see that for the correct interpretation of the nanomesh-like moiré pattern of the R0 graphene phase one has to account for both surface and subsurface Ir layers [Figure 5.33(d)]. In contrast, the rotated graphene domains in the Rε phase tend to show a pattern of bubbles (or triangles), a proper understanding of which requires to exclude the influence of the subsurface Ir layer [Figure 5.33(b)]. This is clearly seen in Figure 5.34 which report STM images acquired from rotated graphene domains and their neighbouring areas. One sees that the moiré of R0 graphene forms a perfect nanomesh, the moiré of 1.4°-rotated domain shows a certain tendency toward triangles and the moiré of 2°-rotated graphene reveals a purely triangular pattern. The finding that the subsurface atomic layer of Ir is not involved in the formation of moiré patterns in the rotational graphene phases is an indication of a *weaker* (as compared to R0) chemical coupling between rotated graphene and Ir(111). This is in line with the aforementioned anomalously large z-corrugations acquired for Rε graphene domains by STM and, last but not least, the reduced substrate induced spin-orbit splitting compared to the R0 phase.

In summary, we have observed a giant Rashba-type spin-orbit splitting of graphene on Ir(111). The splitting ($\sim$ 50 meV) occurs near the Fermi level and is twice larger than $k_\mathrm{B}T$ allowing for room-temperature applications in spintronics. Hybridization with Ir 5d states together with a strong Rashba effect at the Ir(111) surface is identified as reason. The strong splitting of the Dirac cone seen in the Rε phase is not due to spin but reflects the geometry of rotated graphene domains which are in this way structurally characterized by the photoemission data. At the same time the real spin splitting characteristic of graphene bands in the Rε phase is reduced as compared to the R0 phase. Weakening of a chemical interaction between graphene and Ir(111) caused by rotational displacement is suggested as a reason for that. Our findings show that generally a rotational dislocations may be a tool to control the strength of the extrinsic Rashba effect in supported graphene.

SUMMARY AND CONCLUSIONS

The thesis is focused on substrate induced spin polarization effects in the electronic structure of graphene in contact with different substrates. The crystallographic structure and quality of graphene were studied mostly by scanning tunneling microscopy (STM) and low-energy electron diffraction (LEED). The overall electronic structure of graphene on different substrates is studied by means of angle-resolved photoemission (spin-integrated) and the spin structure was investigated by means of spin- and angle-resolved photoelectron spectroscopy. The first part of this thesis contains an overview of the employed methods: XPS, ARPES, spin-resolved ARPES, LEED, overview of experimental stations. Then an introduction to the main topics follows: graphene and its electronic structure, the Rashba effect in a two-dimensional electron gas and at metal surfaces like Au(111) or Ir(111), and the Rashba effect in graphene. Possible sources for the Rashba effect on surface states and the graphene π band are discussed.

The first scientific part of the thesis is devoted to graphene on ferromagnets. Preparation procedure and electronic structure of graphene/Ni(111) and graphene/Co(0001) are discussed. Angle-resolved photoelectron spectroscopy measurements of the graphene electronic structure in the $\overline{\Gamma K}$ direction of the graphene Brillouin zone are in agreement with previously published results and show a strongly *n*-doped graphene π band dispersion without the peculiar relativistic Dirac fermion dispersion near the Fermi level. Measurements in the direction normal to $\overline{\Gamma K}$ allowed us to make the discovery of intact Dirac cones in both graphene/Ni and graphene/Co. By measurements in the $\overline{\Gamma K}$ direction the Dirac cone was not observed before due to a strong interference from two graphene sublattices in the photoelectron emission process. Thus, it has for a long time been believed that the peculiar Dirac cone-like dispersion in graphene is destroyed on ferromagnets by the strong graphene-substrate interaction. The discovery of intact Dirac cones forces us to change significantly our view and understanding of the graphene-ferromagnet systems.

Graphene monolayers on nickel and cobalt were then studied by spin- and angle-resolved photoelectron spectroscopy with the aim to determine the influence of these substrates on spin-orbit coupling and ferromagnetic spin polarization in graphene. There is no detectable Rashba effect, but a spin polarization of the graphene Dirac cone is discovered and studied in very detail. The spin polarization is attributed to the hybridization of the graphene π band with spin-polarized $3d$ states of substrate which occurs away from the Dirac point.

In the second part of this thesis the discussion related to graphene on low-Z substrates is continued for the examples graphene/SiC and graphene/Ag. The graphene on silicon carbide system is introduced in detail and the graphene π band is carefully measured by spin-resolved photoemission. As the result, no detectable spin polarization or Rashba effect were observed in agreement with our expectation that the low-Z materials are insufficient to induce a Rashba effect in graphene. This is confirmed by comparison to *ab initio* calculations predicting a low spin-orbit splitting of 0.05 meV. The graphene on silver system is discussed very briefly with the same result.

Then the thesis treats graphene on high-Z materials, namely gold and iridium. The main result is that a giant Rashba effect is discovered with spin-orbit splittings of $\sim$ 100 meV for graphene/Au and $\sim$ 50 meV for graphene/Ir. Such values are four orders of magnitude larger than the intrinsic spin-orbit splitting in a free graphene layer. Graphene on gold and on iridium manifests itself as quasifreestanding with linear Dirac cone and the Dirac point near the Fermi level. As was measured for graphene/Au, the spin-orbit splitting of the Dirac cone extends to the Fermi level and, therefore, the Fermi surface is spin split. The source of the giant Rashba effect is attributed to hybridization of the graphene π band with spin-polarized gold (iridium) 5d states and, as a consequence, influence of the large gold (iridium) intraatomic potential gradient on the graphene p_z orbitals. *Ab initio* calculations show that a flat Au monolayer can account for only $\sim$ 10 meV spin-orbit splitting and only a structure of laterally more separated gold adatoms could significantly enhance it. The atmospheric stability of the graphene/Au/Ni(111) system was studied by exposure of the samples to atmosphere. It is shown that exposure to air does not carbidize or oxidize the Ni substrate or open an apparent gap in the graphene. Its doping state is not affected and the Rashba-type spin-orbit effect on the graphene π states is preserved. These results show that it is possible to use the peculiar electronic and spin properties of the graphene/Au/Ni system in ambient environment and not only under ultra-high vacuum conditions.

In the thesis also a Rashba split iridium surface state is studied in detail and its unexpected behaviour upon graphene formation on top of the iridium surface is shown. It is demonstrated that the existence of the surface state, its spin polarization, and the size of its Rashba-type spin-orbit splitting remain unaffected when iridium is covered with graphene. The protection by the graphene allows the spin-split surface state to survive in ambient atmosphere. Reducing the growth temperature of graphene on iridium results in a very large splitting of the graphene Dirac cone. Data analysis shows that this splitting does not relate to spin but is due to overlap of photoemission intensities from a distribution of rotated graphene domains. This model successfully explains unusual structures observed in ARPES, LEED and STM. The Rashba effect on this phase is considerably smaller compared to the usual graphene/Ir phase which implies that the magnitude of the extrinsic spin-orbit splitting in supported graphene can be controlled by its rotational displacement relative to the substrate.

BIBLIOGRAPHY

[1] P. R. Wallace, *Phys. Rev.* **71**, 622 (1947)

[2] J. Shelton, H. Patil, and J. Blakely, *Surf. Sci.* **43**, 493 (1974)

[3] T. Aizawa, R. Souda, Y. Ishizawa, H. Hirano, T. Yamada, and K. Tanaka, *Surf. Sci.* **237**, 194 (1990)

[4] A. Nagashima, N. Tejima, and C. Oshima, *Phys. Rev. B* **50**, 17487 (1994)

[5] A. M. Shikin, D. Farías, V. K. Adamchuk, and K.-H. Rieder, *Surface Science* **424**, 155 (1999)

[6] A. M. Shikin, G. V. Prudnikova, V. K. Adamchuk, F. Moresco, and K.-H. Rieder, *Phys. Rev. B* **62**, 13202 (2000)

[7] A. Varykhalov, J. Sánchez-Barriga, A. M. Shikin, C. Biswas, E. Vescovo, A. Rybkin, D. Marchenko, and O. Rader, *Phys. Rev. Lett.* **101**, 157601 (2008)

[8] A. Bostwick, J. McChesney, T. Ohta, E. Rotenberg, T. Seyller, and K. Horn, *Progress in Surface Science* **84**, 380 (2009)

[9] K. V. Emtsev, A. Bostwick, K. Horn, J. Jobst, G. L. Kellogg, L. Ley, J. L. McChesney, T. Ohta, S. A. Reshanov, J. Röhrl, E. Rotenberg, A. K. Schmid, D. Waldmann, H. B. Weber, and T. Seyller, *Nature Mater.* **8**, 203 (2009)

[10] A. M. Shikin, A. G. Rybkin, D. E. Marchenko, A. A. Popova, A. Varykhalov, and O. Rader, *Nanotechnologies in Russia* **6**, 625 (2011)

[11] K. S. Novoselov, A. K. Geim, S. V. Morozov, D. Jiang, Y. Zhang, S. V. Dubonos, I. V. Grigorieva, and A. A. Firsov, *Science* **306**, 666 (2004)

[12] Nobel Foundation announcement

[13] A. K. Geim and K. S. Novoselov, *Nature Materials* **6**, 183 (2007)

[14] F. Miao, S. Wijeratne, Y. Zhang, U. C. Coskun, W. Bao, and C. N. Lau, *Science* **317**, 1530 (2007)

[15] M. C. Lemme, T. J. Echtermeyer, M. Baus, and H. Kurz, *IEEE Electron Device Letters* **28**, 282 (2007)

[16] Y. Wang, X. Chen, Y. Zhong, F. Zhu, and K. P. Loh, *Appl. Phys. Lett.* **95**, 063302 (2009)

[17] P. Matyba, H. Yamaguchi, G. Eda, M. Chhowalla, L. Edman, and N. D. Robinson, *ACS Nano* **4**, 637 (2010)

[18] M. D. Stoller, S. Park, Y. Zhu, J. An, and R. S. Ruoff, *Nano Lett.* **8**, 3498 (2008)

[19] E. I. Rashba, *Sov. Phys. Solid State* **2**, 1109 (1960)

[20] M. W. Wu, J. H. Jiang, and M. Q. Weng, *Phys. Rep.* **493**, 61 (2010)

[21] S. LaShell, B. A. McDougall, and E. Jensen, *Phys. Rev. Lett.* **77**, 3419 (1996)

[22] L. Petersen and P. Hedegård, *Surface Science* **459**, 49 (2000)

[23] T. Hirahara, K. Miyamoto, I. Matsuda, T. Kadono, A. Kimura, T. Nagao, G. Bihlmayer, E. V. Chulkov, S. Qiao, K. Shimada, H. Namatame, M. Taniguchi, and S. Hasegawa, *Phys. Rev. B* **76**, 153305 (2007)

[24] M. Hochstrasser, J. G. Tobin, E. Rotenberg, and S. D. Kevan, *Phys. Rev. Lett.* **89**, 216802 (2002)

[25] E. Rotenberg, J. W. Chung, and S. D. Kevan, *Phys. Rev. Lett.* **82**, 4066 (1999)

[26] A. M. Shikin, A. Varykhalov, G. V. Prudnikova, D. Usachev, V. K. Adamchuk, Y. Yamada, J. Riley, and O. Rader, *Phys. Rev. Lett.* **100**, 057601 (2008)

[27] R. Winkler, *Spin-Orbit Coupling Effects in Two-Dimensional Electron and Hole Systems (Springer, Berlin)* (2003)

[28] T. Fujita, M. B. A. Jalil, and S. G. Tan, *J. Phys. Cond. Mat.* **20**, 115206 (2008)

[29] J. Nitta and T. Koga, *Journal of Superconductivity* **16**, 689 (2003)

[30] S. Datta and B. Das, *Appl. Phys. Lett.* **56**, 665 (1990)

[31] J. Nitta and T. Bergsten, *IEEE Transactions on Electron Devices* **54**, 955 (2007)

[32] N. Tombros, C. Jozsa, M. Popinciuc, H. T. Jonkman, and B. van Wees, *Nature (London)* **448**, 571 (2007)

[33] M. Shiraishi, M. Ohishi, R. Nouchi, N. Mitoma, T. Nozaki, T. Shinjo, and Y. Suzuki, *Adv. Funct. Mater.* **19**, 3711 (2009)

[34] W. Han, K. Pi, W. Bao, K. M. McCreary, Y. Li, W. H. Wang, C. N. Lau, and R. K. Kawakami, *Appl. Phys. Lett.* **94**, 222109 (2009)

[35] D. Huertas-Hernando, F. Guinea, and A. Brataas, *Phys. Rev. Lett.* **103**, 146801 (2009)

[36] S. Cho, Y.-F. Chen, and M. S. Fuhrer, *Appl. Phys. Lett.* **91**, 123105 (2007)

[37] Y. S. Dedkov, M. Fonin, and C. Laubschat, *Appl. Phys. Lett.* **92**, 052506 (2008)

[38] V. M. Karpan, P. A. Khomyakov, A. A. Starikov, G. Giovannetti, M. Zwierzycki, M. Talanana, G. Brocks, J. van den Brink, and P. J. Kelly, *Phys. Rev. B* **78**, 195419 (2008)

[39] A. Dyrdal, V. K. Dugaev, and J. Barnaś, *Phys. Rev. B* **80**, 155444 (2009)

[40] C. L. Kane and E. J. Mele, *Phys. Rev. Lett.* **95**, 226801 (2005)

[41] C. Weeks, J. Hu, J. Alicea, M. Franz, and R. Wu, *Phys. Rev. X* **1**, 021001 (2011)

[42] Z. Qiao, S. A. Yang, W. Feng, W. Tse, J. Ding, Y. Yao, J. Wang, and Q. Niu, *Phys. Rev. B* **82**, 161414 (2010)

[43] M. Zarea, S. E. Ulloa, and N. Sandler, *Phys. Rev. Lett.* **108**, 046601 (2012)

[44] G. Weisz, *Phys. Rev.* **149**, 504 (1966)

[45] A. M. Shikin, A. G. Rybkin, D. E. Marchenko, D. Y. Usachov, A. Y. Varykhalov, and O. Rader, *Physics of the Solid State* **52**, 1515 (2010)

[46] A. Varykhalov, J. Sánchez-Barriga, A. M. Shikin, W. Gudat, W. Eberhardt, and O. Rader, *Phys. Rev. Lett.* **101**, 256601 (2008)

[47] A. G. Rybkin, A. M. Shikin, V. K. Adamchuk, D. Marchenko, C. Biswas, A. Varykhalov, and O. Rader, *Phys. Rev. B* **82**, 233403 (2010)

[48] S. Hüfner, *Photoelectron Spectroscopy: Principles and Applications, Springer* (1995)

[49] H. Hertz, *Ann. Phys.* **17**, 983 (1887)

[50] A. Einstein, *Ann. Phys.* **31**, 132 (1905)

[51] P. J. Feibelman and D. E. Eastman, *Phys. Rev. B* **10**, 4932 (1974)

[52] A. Damascelli, *Physica Scripta* **T109**, 61 (2004)

[53] M. P. Seah and W. A. Dench, *Surf. Interface. Anal.* **1**, 2 (1979)

[54] Saiht, http://commons.wikimedia.org/wiki/File:PES3.jpg

[55] SPECS GmbH, http://www.specs.com

[56] G. C. Burnett, T. J. Monroe, and F. B. Dunning, *Review of Scientific Instruments* **65**, 1893 (1994)

[57] M. A. Van Hove, W. H. Weinberg, and C. M. Chan, *Springer-Verlag, Berlin Heidelberg New York.* (1986)

[58] P. P. Ewald, *Acta Crystallographica Section A* **25**, 103 (1969)

[59] VG Scienta, http://www.vgscienta.com

[60] Omicron, http://www.omicron.de

[61] B. Partoens and F. M. Peeters, *Phys. Rev. B* **74**, 075404 (2006)

[62] M. Hoesch, M. Muntwiler, V. N. Petrov, M. Hengsberger, L. Patthey, M. Shi, M. Falub, T. Greber, and J. Osterwalder, *Phys. Rev. B* **69**, 241401(R) (2004)

[63] C. E. Moore, *National Bureau of Standards, Washington, DC* (1970)

[64] A. O. E. Animalu, *Philos. Mag.* **13** (1966)

[65] J. C. Boettger and S. B. Trickey, *Phys. Rev. B* **75**, 121402 (2007)

[66] M. Gmitra, S. Konschuh, C. Ertler, C. Ambrosch-Draxl, and J. Fabian, *Phys. Rev. B* **80**, 235431 (2009)

[67] A. H. Castro Neto and F. Guinea, *Phys. Rev. Lett.* **103**, 026804 (2009)

[68] D. Marchenko, A. Varykhalov, M. R. Scholz, G. Bihlmayer, E. I. Rashba, A. Rybkin, A. M. Shikin, and O. Rader, *Nature Communications* **3**, 1232 (2012)

[69] J. Nilsson, A. H. Castro Neto, F. Guinea, and N. M. R. Peres, *Phys. Rev. Lett.* **97**, 266801 (2006)

[70] E. I. Rashba, *Phys. Rev. B* **79**, 161409(R) (2009)

[71] F. Kuemmeth and E. I. Rashba, *Phys. Rev. B* **80**, 241409 (2009)

[72] Y. S. Dedkov, M. Fonin, U. Rüdiger, and C. Laubschat, *Phys. Rev. Lett.* **100**, 107602 (2008)

[73] I. Gierz, J. H. Dil, F. Meier, B. Slomski, J. Osterwalder, J. Henk, R. Winkler, C. R. Ast, and K. Kern, *arXiv:1004.1573v1* (2010)

[74] O. Rader, A. Varykhalov, J. Sánchez-Barriga, D. Marchenko, A. Rybkin, and A. M. Shikin, *Phys. Rev. Lett.* **102**, 057602 (2009)

[75] J. Sánchez-Barriga, *"A photoemission study of quasiparticle excitations, electron-correlation effects and magnetization dynamics in thin magnetic systems", PhD Thesis, Potsdam University* (2010)

[76] J. Sánchez-Barriga, A. Varykhalov, M. R. Scholz, O. Rader, D. Marchenko, A. Rybkin, A. M. Shikin, and E. Vescovo, *Diamond and Related Materials* **19**, 734 (2010)

[77] I. Forbeaux, J. M. Themlin, and J. M. Debever, *Phys. Rev. B* **58**, 16396 (1998)

[78] Y. Gamo, A. Nagashima, M. Wakabayashi, M. Terai, and C. Oshima, *Surface Science* **374**, 61 (1997)

[79] D. Eom, D. Prezzi, K. T. Rim, H. Zhou, M. Lefenfeld, S. Xiao, C. Nuckolls, M. S. Hybertsen, T. F. Heinz, and G. W. Flynn, *Nano Lett.* **9**, 2844 (2009)

[80] Y. S. Dedkov, A. M. Shikin, V. K. Adamchuk, S. L. Molodtsov, C. Laubschat, A. Bauer, and G. Kaindl, *Phys. Rev. B* **64**, 035405 (2001)

[81] Y. S. Dedkov and M. Fonin, *New J. Phys.* **12**, 125004 (2010)

[82] A. A. Grüneis and D. V. Vyalikh, *Phys. Rev. B* **77**, 193401 (2008)

[83] A. Varykhalov, D. Marchenko, J. Sánchez-Barriga, M. R. Scholz, B. Verberck, B. Trauzettel, T. O. Wehling, C. Carbone, and O. Rader, *"Intact Dirac cones at broken sublattice symmetry: photoemission study of graphene on Ni and Co", in press, Phys. Rev. X* (2012)

[84] E. L. Shirley, L. J. Terminello, A. Santoni, and F. J. Himpsel, *Phys. Rev. B* **51**, 13614 (1995)

[85] F. J. Himpsel, J. A. Knapp, and D. E. Eastman, *Phys. Rev. B* **19**, 2919 (1979)

[86] F. J. Himpsel and D. E. Eastman, *Phys. Rev. B* **21**, 3207 (1980)

[87] Y. S. Dedkov, M. Fonin, U. Rüdiger, and C. Laubschat, *Appl. Phys. Lett.* **93**, 022509 (2008)

[88] V. M. Karpan, G. Giovannetti, P. A. Khomyakov, M. Talanana, A. A. Starikov, M. Zwierzycki, J. van den Brink, G. Brocks, and P. J. Kelly, *Phys. Rev. Lett.* **99**, 176602 (2007)

[89] I. D. Marco, *"Correlation Effects in the Electronic Structure of Transition Metals and Their Compounds", PhD Thesis, University of Nijmegen* (2009)

[90] I. Gierz, J. H. Dil, F. Meier, B. Slomski, J. Osterwalder, J. Henk, R. Winkler, C. R. Ast, and K. Kern, *arXiv:1004.1573v2* (2011)

[91] T. Seyller, A. Bostwick, K. V. Emtsev, K. Horn, L. Ley, J. L. McChesney, T. Ohta, J. D. Riley, E. Rotenberg, and F. Speck, *Phys. Stat. Sol. B* **245**, 1436 (2008)

[92] J. Bernhardt, J. Schardt, U. Starke, and K. Heinz, *Appl. Phys. Lett.* **74**, 1084 (1999)

[93] I. Gierz, T. Suzuki, R. T. Weitz, D. S. Lee, B. Krauss, C. Riedl, U. Starke, H. Höchst, J. H. Smet, C. R. Ast, and K. Kern, *Phys. Rev. B* **81**, 235408 (2010)

[94] K. V. Emtsev, F. Speck, T. Seyller, L. Ley, and J. D. Riley, *Phys. Rev. B* **77**, 155303 (2008)

[95] T. Bostwick, A. anc Ohta, T. Seyller, K. Horn, and E. Rotenberg, *Nature Phys.* **3**, 36 (2007)

[96] S. Y. Zhou, G.-H. Gweon, A. V. Fedorov, P. N. First, W. A. de Heer, D.-H. Lee, F. Guinea, A. H. Castro Neto, and A. Lanzara, *Nature Mater.* **6**, 770 (2007)

[97] F. Varchon, R. Feng, J. Hass, X. Li, B. Ngoc Nguyen, C. Naud, P. Mallet, J.-Y. Veuillen, C. Berger, E. H. Conrad, and L. Magaud, *Phys. Rev. Lett.* **99**, 126805 (2007)

[98] S. Kim, J. Ihm, H. J. Choi, and Y.-W. Son, *Phys. Rev. Lett.* **100**, 176802 (2008)

[99] S. Abdelouahed, A. Ernst, J. Henk, I. V. Maznichenko, and I. Mertig, *Phys. Rev. B* **82**, 125424 (2010)

[100] B. Premlal, M. Cranney, F. Vonau, D. Aubel, D. Casterman, M. M. De Souza, and L. Simon, *Appl. Phys. Lett.* **94**, 263115 (2009)

[101] I. Barke, F. Zheng, T. K. Rugheimer, and F. J. Himpsel, *Phys. Rev. Lett.* **97**, 226405 (2006)

[102] F. Reinert, G. Nicolay, S. Schmidt, D. Ehm, and S. Hüfner, *Phys. Rev. B* **63**, 115415 (2001)

[103] J. Henk, M. Hoesch, J. Osterwalder, A. Ernst, and P. Bruno, *J. Phys.: Condens. Matter* **16**, 7581 (2004)

[104] K. Yamamoto, M. Fukushima, T. Osaka, and C. Oshima, *Phys. Rev. B* **45**, 11358 (1992)

[105] P. Stoppmanns, B. Heidemann, N. Irmer, N. Müller, B. Vogt, B. Schmiedeskamp, U. Heinzmann, E. Tamura, and R. Feder, *Phys. Rev. Lett.* **66**, 2645 (1991)

[106] J. Jacobsen, L. P. Nielsen, F. Besenbacher, I. Stensgaard, E. Lægsgaard, T. Rasmussen, K. W. Jacobsen, and J. K. Norskov, *Phys. Rev. Lett.* **75**, 489 (1995)

[107] K. Umezawa, S. Nakanishi, and W. M. Gibson, *Phys. Rev. B* **57**, 8842 (1998)

[108] E. K. Vestergaard, R. T. Vang, J. Knudsen, T. M. Pedersen, T. An, E. Lægsgaard, I. Stensgaard, B. Hammer, and F. Besenbacher, *Phys. Rev. Lett.* **95**, 126101 (2005)

[109] G. Giovannetti, P. A. Khomyakov, G. Brocks, V. M. Karpan, J. van den Brink, and P. J. Kelly, *Phys. Rev. Lett.* **101**, 026803 (2008)

[110] G. Bihlmayer, Y. M. Koroteev, P. M. Echenique, E. V. Chulkov, and S. Blügel, *Surf. Sci.* **600**, 3888 (2006)

[111] M. Nagano, A. Kodama, T. Shishidou, and T. Oguchi, *J. Phys.: Condens. Matter* **21**, 064239 (2009)

[112] A. Varykhalov, M. R. Scholz, T. K. Kim, and O. Rader, *Phys. Rev. B* **82**, 121101(R) (2010)

[113] A. Y. Tontegode, *Prog. Surf. Sci.* **38**, 201 (1991)

[114] A. Varykhalov, W. Gudat, and O. Rader, *Adv. Mater.* **22**, 3307 (2010)

[115] K. S. Novoselov, A. K. Geim, S. V. Morozov, D. Jiang, M. I. Katsnelson, I. V. Grigorieva, S. V. Dubonos, and A. A. Firsov, *Nature (London)* **438**, 197 (2005)

[116] Q. K. Yu, J. Lian, B. Siriponglert, H. Li, Y. P. Chen, and S. S. Pei, *Appl. Phys. Lett.* **93**, 113103 (2008)

[117] P. Blake, R. Yang, S. V. Morozov, F. Schedin, L. A. Ponomarenko, and A. A. Uhukov, *Solid State Commun.* **149**, 1068 (2009)

[118] E. Rossi and S. D. Sarma, *Phys. Rev. Lett.* **101**, 166803 (2008)

[119] H.-G. Jee, J.-H. Han, H.-N. Hwang, B. Kim, H.-S. Kim, Y. D. Kim, and C.-C. Hwang, *Appl. Phys. Lett.* **95**, 093107 (2009)

[120] V. A. Mozhayskiy, A. Y. Varykhalov, A. G. Starodubov, A. M. Shikin, S. I. Fedoseenko, and V. K. Adamchuk, *Fullerenes, Nanotubes, Carbon Nanostruct.* **12**, 385 (2004)

[121] T. O. Wehling, A. I. Lichtenstein, and M. I. Katsnelson, *Appl. Phys. Lett.* **93**, 202110 (2008)

[122] O. Leenaerts, B. Partoens, and F. M. Peeters, *Phys. Rev. B* **79**, 235440 (2009)

[123] A. Varykhalov and O. Rader, *Phys. Rev. B* **80**, 035437 (2009)

[124] I. Pletikosić, M. Kralj, P. Pervan, R. Brako, J. Coraux, A. T. N'Diaye, C. Busse, and T. Michely, *Phys. Rev. Lett.* **102**, 056808 (2009)

[125] C. Busse, P. Lazic, R. Djemour, J. Coraux, T. Gerber, N. Atodiresei, V. Caciuc, R. Brako, A. T. N'Diaye, S. Bluegel, J. Zegenhagen, and T. Michely, *Phys. Rev. Lett.* **107**, 036101 (2011)

[126] E. Loginova, S. Nie, K. Thuermer, N. C. Bartelt, and K. F. McCarty, *Phys. Rev. B* **80**, 085430 (2009)

[127] H. Hattab, A. T. N'Diaye, D. Wall, G. Jnawali, J. Coraux, C. Busse, R. van Gastel, B. Poelsema, T. Michely, F.-J. Meyer zu Heringdorf, and M. Horn-von Hoegen, *Appl. Phys. Lett.* **98**, 141903 (2011)

[128] J. Sánchez-Barriga, A. Varykhalov, D. Marchenko, M. R. Scholz, and O. Rader, *Phys. Rev. B* **85**, 201413(R) (2012)

[129] J. F. van der Veen, F. J. Himpsel, and D. E. Eastman, *Phys. Rev. B* **22**, 4226 (1980)

ABBREVIATIONS

2DEG - Two-dimentional electron gas

ARPES - Sngle-resolved photoelectron spectroscopy

BE - Binding energy

DFT - Density functional theory

E_F - Fermi level

eV - Electronvolt

LEED - Low-energy electron diffraction

ML - Monolayer

PES - Photoelectron spectroscopy

QWS - Quantum-well state

SARPES - Spin- and angle-resolved photoelectron spectroscopy

STM - Scanning tunneling microscopy

UHV - Ultra-high vacuum

UPS - Ultraviolet photoelectron spectroscopy

XPS - X-ray photoelectron spectroscopy

CURRICULUM VITAE

Personal information:

Name: Dmitry Marchenko
Date of birth: 15 January 1984
Nationality: Russian
Tel.: +49-176-77320817
E-mail: marchenko.dmitry@gmail.com

Educational Background:

2009 - Present: Ph.D. Student,
Helmholtz-Zentrum Berlin für Materialien und Energie
and Potsdam University, Germany.
Supervisor: apl. Prof. Dr. O. Rader.

Jan - Dec 2009: Beamline manager at the Russian-German beamline,
Synchrotron BESSY-II, Berlin.

2006 - 2009: Master degree in physics, Saint-Petersburg State University, Russia.
"Electronic structure of graphene on Co/W(110) and its modification
by intercalation of Al, Cu, Au atoms".
Supervisors: Prof. V. K. Adamchuk and Prof. A. M. Shikin.

2002 - 2006: Bachelor degree in physics, Saint-Petersburg State University, Russia.
"Application of Angle-Resolved Photoelectron Spectroscopy technique to analysis
of surface states modification in thin Mg films on W(110)".
Supervisor: Prof. A. M. Shikin.

1998 - 2002: Academic Gymnasium of Saint-Petersburg State University,
Saint-Petersburg, Russia. Mathematics and Physics specialization.

1994 - 1998: School No. 12, Yevpatoria, Crimea, Ukraine.
Mathematics specialization.

1991 - 1994: School No. 47, Irkutsk, Russia.

LIST OF PUBLICATIONS

Submitted:

30* *"Absence of giant Rashba splitting in graphene/SiC"*,
D. Marchenko, A. Varykhalov, M. R. Scholz, O. Rader, A. Popova and A. M. Shikin, Th. Seyller,
Phys. Rev. B, code BXR1141.

29* *"Giant Rashba splittings of Dirac fermions in aligned and rotated graphene on Ir(111)"*,
D. Marchenko, J. Sánchez-Barriga, M. R. Scholz, O. Rader and A. Varykhalov,
Phys. Rev. B, code LV13450B.

28 *"Reversal of the circular dichroism in the angle-resolved photoemission from Bi2Te3"*,
M. R. Scholz, J. Sánchez-Barriga, J. Braun, D. Marchenko, A. Varykhalov, M. Lindroos, Yung Jui Wang, Hsin Lin, A. Bansil, J. Minár, H. Ebert, A. Volykhov, L. V. Yashina, and O. Rader,
Phys. Rev. Lett., code LU13301.

Accepted for publication, in press:

27 *"Interaction of graphene with intercalated Al: The process of intercalation and specific features of the electronic structure of the system"*,
A. A. Popova, A. G. Rybkin, A. V. Fedorov, D. Yu. Usachev, M. E. Yachmenev, D. E. Marchenko, O. Yu. Vilkov, A. V. Nelyubov, V. K. Adamchuk, A. M. Shikin,
Surface Science.

Published:

26* *"Induced spin-orbit splitting in graphene: role of atomic number of intercalated metal and π-d hybridization"*,
A. Shikin, A. Rybkin, D. Marchenko, A. Popova, M. Scholz, O. Rader, A. Varykhalov,
New. J. Phys **15** 013016 (2013).

25* *"Intact Dirac cones at broken sublattice symmetry: photoemission study of graphene on Ni and Co"*,
A. Varykhalov, D. Marchenko, J. Sánchez-Barriga, M. R. Scholz, B. Verberck, B. Trauzettel, T. O. Wehling, C. Carbone, O. Rader, Phys. Rev. X **2**, 041017 (2012).

24* *"Giant Rashba splitting in graphene due to hybridization with gold"*, D. Marchenko, A. Varykhalov, M. R. Scholz, G. Bihlmayer, E. I. Rashba, A. Rybkin, A. M. Shikin, O. Rader, Nature Communications **3**, 1232 (2012).

23 *"Topology of spin polarization of the 5d states on W(110) and Al/W(110) surfaces"*, A. G. Rybkin, E. E. Krasovskii, D. Marchenko, E. V. Chulkov, A. Varykhalov, O. Rader, and A. M. Shikin, Phys. Rev. B **86**, 035117 (2012).

22 *"Tolerance of Topological Surface States towards Magnetic Moments: Fe on Bi2Se3"*, M. R. Scholz, J. Sánchez-Barriga, D. Marchenko, A. Varykhalov, A. Volykhov, L.V. Yashina, and O. Rader, Phys. Rev. Lett. **108**, 256810 (2012).

21* *"Minigap isotropy and broken chirality in graphene with periodic corrugation enhanced by cluster superlattices"*, J. Sánchez-Barriga, A. Varykhalov, D. Marchenko, M. R. Scholz, O. Rader, Phys. Rev. B **85**, 201413 (2012).

20* *"Ir(111) Surface State with Giant Rashba Splitting Persists under Graphene in Air"*, A. Varykhalov, D. Marchenko, M. R. Scholz, E. D. L. Rienks, T. K. Kim, G. Bihlmayer, J. Sánchez-Barriga, and O. Rader, Phys. Rev. Lett **108**, 066804 (2012).

19* *"Spin-dependent avoided-crossing effect on quantum-well states in Al/W(110)"*, A. G. Rybkin, A. M. Shikin, D. Marchenko, A. Varykhalov, and O. Rader, Phys. Rev. B **85**, 045425 (2012).

18* *"Graphene: Synthesis and features of electronic structure"*, A. M. Shikin, A. G. Rybkin, D. E. Marchenko, A. A. Popova, A. Varykhalov und O. Rader, Nanotechnologies in Russia **6**, 625-632 (2011).

17* *"The Role of the Covalent Interaction in the Formation of the Electronic Structure of Au- and Cu-Intercalated Graphene on Ni(111)"*, A. A. Popova, A. M. Shikin, A. G. Rybkin, D. E. Marchenko, O. Yu. Vilkov, A. A. Makarova, A. Yu. Varykhalov, and O. Rader, Physics of the Solid State **53**, 2539-2544 (2011).

16 *"Hydrogenation, Purification and Unzipping of Carbon Nanotubes by Reaction with Molecular Hydrogen: Road to Graphane Nanoribbons"*, A. Talyzin, S. Luzan, I. Anoshkin, A. Nasibulin, J. Hua, E. Kauppinen, V. Mikoushkin, V. Shnitov, D. Marchenko, D. Noreus, ACS Nano **5**, 5132-5140 (2011).

15* *"Atmospheric stability and doping protection of noble-metal intercalated graphene on Ni(111)"*, D. Marchenko, A. Varykhalov, A. Rybkin, A.M. Shikin, and O. Rader, Appl. Phys. Lett. **98**, 122111 (2011).

14 *"Formation of ultrathin iron magnetic films on the silicon vicinal surface"*, M. V. Gomoyunova, G. S. Grebenyuk, I. I. Pronin, S. M. Solov'ev, D. E. Marchenko and D. V. Vyalikh, Physics of the Solid State **53**, 606-611 (2011).

13 *"Studying the electronic structure of Cr(x)Ti(1-x)Se(2) by X-ray resonance and absorption spectroscopy"*, A. S. Shkvarin, Yu. M. Yarmoshenko, N. A. Skorikov, A. I. Merentsov, A. N. Titov, P. A. Slepuhin, D. E. Marchenko, M. Sperling, Journal of Experimental and Theoretical Physics **112**, 87-93 (2011).

12* *"Large spin-orbit splitting in light quantum films: Al/W(110)"*, A. G. Rybkin, A. M. Shikin, V. K. Adamchuk, D. Marchenko, C. Biswas, A. Varykhalov and O. Rader, Phys. Rev. B **82**, 233403 (2010).

11 *"Tunable Band Gap in Hydrogenated Quasi-Free-standing Graphene"*, D. Haberer, D. V. Vyalikh, S. Taioli, B. Dora, M. Farjam, J. Fink, D. Marchenko, T. Pichler, K. Ziegler, S. Simonucci, M. S. Dresselhaus, M. Knupfer, B. Büchner, and A. Grüneis, Nano Letters **10**, 3360-3366 (2010).

10 *"XPS and depth resolved SXES study of HfO(2)/Si interlayers"*, E. O. Filatova, A. A. Sokolov, A. A. Ovchinnikov, S. Yu. Tveryanovich, E. P. Savinov, D. E. Marchenko, V. V. Afanas'ev, A. S. Shulakov, Journal of Electron Spectroscopy and Related Phenomena **181**, 206-210 (2010).

9 *"X-ray spectroscopic examination of thin HfO(2) films ALD- and MOCVD-grown on the Si(100) surface"*, A. A. Sokolov, A. A. Ovchinnikov, K. M. Lysenkov, D. E. Marchenko and E. O. Filatova, Technical Physics **55**, 1045-1050 (2010).

8* *"Substrate-induced spin-orbit splitting of quantum-well and interface states in Au, Ag, and Cu layers of different thicknesses on W(110) and Mo(110) surfaces"*, A. M. Shikin, A. G. Rybkin, D. E. Marchenko, D. Yu. Usachov, V. K. Adamchuk, A. Yu. Varykhalov, O. Rader, Physics of the Solid State **52**, 1515-1525 (2010).

7* *"Chemical vapour deposition of graphene on Ni(111) and Co(0001) and intercalation with Au to study Dirac-cone formation and Rashba splitting"*, J. Sánchez-Barriga, A. Varykhalov, M.R. Scholz, O. Rader, D. Marchenko, A. Rybkin, A.M. Shikin, E. Vescovo, Diamond and Related Materials **19**, 734-741 (2010).

6 *"Formation of spectra of quantum well states in thin Al layers on W(110)"*, A. G. Rybkin, D. Yu. Usachov, D. E. Marchenko, A. M. Shikin, V. K. Adamchuk, A. Yu.Varykhalov, O. Rader, Journal of Surface Investigation-X-Ray Synchrotron and Neutron Techniques **4**, 401-404 (2010).

5 *"Spectroscopic investigations of the stability of porous silicon structure obtained by etching Si(100) in aqueous ammonium fluoride solution"*, E. O. Filatova, K. M. Lysenkov, A. A. Sokolov, A. A. Ovchinnikov, D. E. Marchenko, V. M. Kashkarov und I. V. Nazarikov, Technical Physics Letters **36**, 119-121 (2010).

4 *"Analysis of the possibility of the spin-orbit origin of surface state splitting in thin Mg(0001) layers on W(110) and Mo(110)"*, A. M. Shikin, D. E. Marchenko, N.

A. Vinogradov, G. V. Prudnikova, A. G. Rybkin, V. K. Adamchuk and O. Rader, Physics of the Solid State **51**, 608-619 (2009).

3* *"Is There a Rashba Effect in Graphene on 3d Ferromagnets?"*, O. Rader, A. Varykhalov, J. Sánchez-Barriga, D. Marchenko, A. Rybkin, and A.M. Shikin, Phys. Rev. Lett. **102**, 057602 (2009).

2 *"Size Effects in Ultrathin Mg/W(110) Films: Quantum Electronic States"*, N. A. Vinogradov, D. E. Marchenko, A. M. Shikin, V. K. Adamchuk and O. Rader, Physics of the Solid State **51**, 179-188 (2009).

1* *"Electronic and Magnetic Properties of Quasifreestanding Graphene on Ni"*, A. Varykhalov, J. Sánchez-Barriga, A.M. Shikin, C. Biswas, E. Vescovo, A. Rybkin, D. Marchenko, and O. Rader, Phys. Rev. Lett. **101**, 157601 (2008).

Asterisks (*) denote publications directly related to the presented thesis.

ZUSAMMENFASSUNG

Graphen ist eigentlich eine lange bekannte Form des Kohlenstoffs, deren elektronische Struktur bereits 1947 berechnet wurde und die auf Nickel-Einkristallen schon in den Siebzigerjahren hergestellt wurde. Ber?hmt wurde Graphen, nachdem Andrei Geim und Konstantin Novoselov 2004 eine mikromechanische Spaltmethode zur Herstellung von frei tragendem Graphen vorgeschlagen haben. Sie konnten zeigen, dass die Elektronen im Graphen sich eher wie Licht verhalten als wie massive Teilchen, und erhielten 2010 den Physik-Nobelpreis "für grundlegende Experimente am zweidimensionalen Material Graphen".

Beim Rashba-Effekt handelt es sich um eine Ausprägung der Spin-Bahn-Wechselwirkung. Beide beschreiben die Energieunterschiede, die ein Elektron zwischen zwei verschiedenen Orientierungen von Drehimpulsen erfährt. Dreht sich das Elektron im selben Sinne um sich selbst wie um den Kern des Atoms, in diesem Fall des Kohlenstoffs, nimmt es eine andere Energie an als in dem Falle, dass diese beiden Drehungen einander entgegen gerichtet sind. Dieser für die Atomphysik wesentliche Effekt wurde von Rashba für zweidimensionale Elektronensysteme, wie Graphen eines ist, beschrieben.

Spin-Bahn-Wechselwirkung und Rashba-Effekt spielen eine wichtige Rolle bei der Überführung der gegenwärtigen Elektronik, die die Ladung der Elektronen nutzt, in eine Spintronik, die auf dem Spin der Elektronen basiert. Bisher wird Graphen vor allem im Hinblick auf den Transport von Ladung untersucht, denn in der Spintronik wäre es zwar in der Lage, einen Spinstrom verlustarm zu transportieren, könnte aber diesen Spinstrom kaum beeinflussen, da es eine äußerst geringe Spin-Bahn-Wechselwirkung besitzt.

Das Wesen des Rashba-Effekts ist die Kontrolle der Spin-Bahn-Wechselwirkung durch äußeren Einfluss. Auf dieser Grundlage wird in der gegenwärtigen Arbeit für verschiedene Systeme die Spin-Bahn-Aufspaltung mit der Methode der spin- und winkelaufgelösten Photoelektronenspektroskopie gemessen. Hierzu wird das Graphen auf verschiedene Arten kristallin auf Einkristalle aufgebracht und mit Beugungsmethoden und mikroskopischen Methoden strukturell untersucht. Zunächst wird gezeigt, dass Graphen in Kontakt mit leichteren Elementen auf Siliziumkarbid und auf Silber keine hohe Spin-Bahn-Wechselwirkung zeigt. Dieser Befund bleibt auch auf Nickel und Kobalt derselbe. Allerdings gelingen zwei überraschende Entdeckungen. Zum einen wird Nickel in der Literatur als Prototyp eines Substrats angesehen, auf dem die Elektronen des Graphen ihr lichtartiges Verhalten verlieren und massiv werden. Es wird gezeigt, dass das nicht der Fall ist und sich ein perfekter sogenannter Dirac-Kegel in der Photoelektronenspektroskopie zeigt. Da Nickel und Kobalt ferromagnetisch sind, ergibt sich nun die Möglichkeit, die Spins im Graphen auf ferromagnetische Weise, die grundsätzlich verschieden von der Spin-Bahn-Wechselwirkung ist, auszurichten. Das wird auf Kobaltsubstrat nachgewiesen.

Das Hauptergebnis der Arbeit ist die Entdeckung einer um vier Größenordnungen erhöhten Spin-Bahn-Aufspaltung von Graphen, wenn es in Kontakt mit Gold tritt. Um diesen experimentellen Befund zu erklären, schließen sich aufwendige elektronische und strukturelle Untersuchungen an. Dass ein solcher riesiger Rashba-Effekt in Graphen auch von anderen Elementen, die ähnlich schwer wie Gold sind, erzeugt werden kann und auf Hybridisierung beruht, wird schließlich in einer abschließenden Untersuchung von Graphen auf Iridium gezeigt. Dieses System unterscheidet sich in struktureller Hinsicht von Graphen auf Au, und neue Strukturen werden im Rahmen dieser Arbeit erstmals erklärt. Hier wird das das Zusammenspiel von Struktur, elektronischer Wechselwirkung mit dem Substrat und induzierter Rashba-artiger Spin-Bahn-Wechselwirkung besonders deutlich.

ACKNOWLEDGEMENTS

I want to thank deeply my supervisor Prof. Oliver Rader for his continuous support and organization of efficient work, encouragement and help in all stages of the thesis preparation. Thanks to Dr. Andrei Varykhalov for excellent experimental stations and great technical and scientific support. Due to his presence work at BESSY became easier and more effective.

I would like to express my deepest acknowledgments to my former supervisors Prof. Alexander Shikin and Prof. Vera Adamchuk. With them I started to work with low-dimensional systems and photoemission techniques, I got very good experimental experience and very interesting research topics. Thanks to them I was able to start working at BESSY in such interesting and successful Russian-German collaboration with plenty of people, experiments, knowledge. For substantial and helpful discussions and ideas.

I am grateful to Dr. Jaime Sánchez-Barriga, Markus Scholz, Dr. Artem Rybkin and Anna Rybkina for the long but effective time together at experiments and discussions.

Thanks to my mother and grandmother for support and the possibility to study in good schools with profound specialization in physics and mathematics. Mathematics and physics have been very exciting for me from the very childhood on and every year of my study in schools and university were very interesting and fascinating. I also appreciate greatly and sincerely Tania, my wife, who has fully supported me in all aspects of my life during my work on the thesis.